SPACE RADIATION DOSIMETRY: AN OPTICALLY STIMULATED LUMINESCENCE RADIATION DETECTOR FOR LOW-EARTH ORBIT

By

RAMONA GAZA

Bachelor of Science

Western University of Timisoara

Timisoara, Timis, Romania

1997

Submitted to the faculty of the
Graduate College of the
Oklahoma State University
in partial fulfillment of
the requirements for
the Degree of
DOCTOR OF PHILOSOPHY
December, 2004

SPACE RADIATION DOSIMETRY: AN OPTICALLY STIMULATED LUMINESCENCE RADIATION DETECTOR FOR LOW-EARTH ORBIT

Dissertation Approved:

Stephen W. S. McKeever
Thesis Adviser

Bruce J. Ackerson

Andrew S. Arena

Albert T. Rosenberger

Paul A. Westhaus

A. Gordon Emslie
Dean of the Graduate College

"This is the goal: To make available for life every place

where life is possible. To make inhabitable all worlds as yet

uninhabitable, and all life purposeful."

(HERMANN OBERTH, Man Into Space, 1957)

ACKNOWLEDGEMENTS

First, I would like to thank my parents Ioana and Mircea Carabas for encouraging me since I was as a little girl to pursue a career in science, and for teaching me the importance of a college education. Thank you for your unconditional love and restless support, and thank you for making me to become whom I am today. I would also like to thank my Grandmother (Mama Mare) who understood from the very beginning my husband and I desire to come to United States. I really appreciate all of your help and understanding over the years.

My love and gratitude go to Paul Gaza, thank you for your continuous interest in our new life here in USA as well as our professional life, your experience and advice helped us many times.

I am thankful for our Romanian friends Doina and Ludovic Kovalik whom showed their continuous friendship and support during my Ph.D. years in Stillwater. Even though our lives took different paths, and we now live more than 1000 miles away, I hope we can keep our precious friendships always.

I am grateful to Ginni Kalchgruber for being my friend over the last two years. Thanks for being always there, optimistic, funny, and patient. I hope that our friendship brought you the same joy and fulfillment that it brought me and that it will continue for the years to come.

My deepest love and gratitude go to Sharon and Lindsay Jones. Thank you for offering us to be part of your family and for the kindness that you have showed us over

the years. Thanks for being our family here in Oklahoma.

To all of my teachers that inspired over the years, especially to my elementary school teacher, Ms. Maria Radu who taught me that I have to improve myself every day. I hope to have a chance one day to share with you all of the wonderful experiences that I had during the last five years.

I would like to thank the faculty of the Physics Department here at OSU. It was a wonderful experience for me to be part of the Physics Department and I am privileged to have been thought by the best. Especially, to Dr. Paul A. Westahus who showed to all of us how a teaching career can be brought to perfection.

My deepest thanks go to Dr. Stephen W.S. McKeever, thank you for helping me follow my dreams. Thank you for saying yes five years ago, when I asked if I could work on the 'astronaut project'. Thank you for your guidance and support, for giving me the chance to see the world and for showing me the wonderful flavor of success. Thank you for the fulfilling experience to study and learn under your guidance.

I am grateful to Dr. Bruce J. Ackerson, to Dr. Albert T. Rosenberger, to Dr. Paul A. Westhaus, and to Dr. A. S. Arena for their guidance as members of my Ph.D. committee.

I would like to thank the staff of the Department of Physics: to Mrs. Susan Cantrell and to Mrs. Cindi Raymond, for their great assistance. Thank you for cooking the 'student day' lunch for us. I would like to thank to Mrs. Glynna Worley from the Vice-President for Research Office (VPRTT) for her tremendous help during this past five years and for helping me so may times with the long process of thesis submission.

My gratitude goes to Dr. Eric Benton and to Dr. Yukio Uchihori for giving me the opportunity to participate in so many interesting projects (ICCHIBAN, BRADOS and

TRACER). Also, my gratitude goes to all of my Japanese friends (Kaori, Kayoko and Hisashi) for their help during the ICCHIBAN projects and also for showing me the flavor of living in Japan. Thank you for your taking the time to show me around and for the wonderful okonomiyaki recipe.

I am thankful to Dr. Maria E. Brandan for offering me the opportunity to collaborate on several research projects at UNAM, Mexico City. Thank you for your professional and personal support. Also, my thanks go to the wonderful research group at UNAM. To Ana-Elena Buenfil, Isabel Gamboa-deBuen, Mercedes Rodríguez-Villafuerte, and Olga Avilla for helping with my research and for being so kind to me always. To Cesar and Karim for their help and patience regarding the 'no-light' conditions needed for my experiments and for extending their help as far as climbing the roof of a rather high building, thank you very much, I really appreciate it.

I would like to thank to Eddie Semones and Mike Golightly for giving me the opportunity to spend one month working with the Space Radiation Analysis Group at Johnson Space Center.

My deepest thanks go to Zonta International Foundation for awarding me the Amelia-Earhart Fellowships. Thank you very much for this opportunity.

Last, and most important, I would like to thank my husband, Razvan, for his love and support, for the wonderful contradictory physics discussions that we had over the years, for trying to keep me focused when life took unexpected turns, and for being there for me at the best and the worst moments of my life.

TABLE OF CONTENTS

LIST OF TABLES

LIST OF FIGURES

CHAPTER 1

INTRODUCTION

1.1. Brief space flight history

On October 4, 1957 world's first artificial satellite of Earth, Sputnik I was successfully launched in the former Soviet Union. Sputnik I orbited the Earth in 96 minutes, weighted 83.6 kg and spent three months in orbit. Only one month later, on November 3, the second former Soviet Union's satellite was launched. Sputnik II weighted more than six times the weight of Sputnik I and had on board the first ever passenger to fly in space, the famous dog Laika.

The first United States (US) Earth satellite, Explorer I was designed and built by the Jet Propulsion Laboratory and it was launched from Cape Canaveral on January 31, 1958. Explorer I is responsible for one of the first important discoveries by satellites, the existence of the Van Allen Belts (charged particles trapped in space by the Earth's magnetic field). During only a four months period the whole history of human exploration changed, marking the beginning of the space exploration era and the first steps in conquering outer space.

The next task for the space exploration was to fly humans onboard spacecrafts. In 1923, Hermann Oberth was the first to mathematically predict that rockets could fly a human into space. Born in Transylvania in 1894, Hermann Oberth, the founding father of rocketry and space travel, wrote in his first book '*By Rocket to Interplanetary Space*' published in 1923 that:

"These I wish to prove in this book:

1. At the present level of science and technology it is possible to build machines which can climb higher than the Earth's atmosphere.
2. With further improvements these machines can reach such speed that if left in space they will not fall back to Earth but will be able to resist the pull of gravity.
3. These machines can be built so that men can go up in them (probably without danger to their bodies)" (Walters, 1962).

The first manned space flight took place almost forty years after Hermann Oberth's predictions. The first man to orbit the Earth was the cosmonaut Yuri Gagarin, on April 12, 1961. He flew aboard the Russian spacecraft Vostok – I during a flight trip of almost two hours. Since then, manned flights have been performed on a regular basis during several US and Russian programs such as Mercury, Gemini, Soyuz, Apollo and the Space Shuttle Program. As a great accomplishment of the US Apollo program, on July 16, 1969 the astronauts Neil A. Armstrong and Edwin E. Aldrin were the first men to walk on the Moon. Between 1961 and 1995, one hundred manned flights took place, with over four hundred astronauts and cosmonauts spending a total of almost one thousand days in space[i].

Another important task for space exploration was to focus on long duration missions. The former Soviet Union launched in 1971 the world's first manned space station, Salyut I. This was followed by the launch of the US Skylab in 1973 and the Soviet Union MIR space station in 1986.

Today, the International Space Station (ISS) built by the collaboration of 16 nations, represents a state of the art orbital construction project that is continuously developed and

[i] Document found on the NASA webpage (February 2004) http://www-pao.ksc.nasa.gov/kscpao/factoids/hundtoc.htm

improved in order to simulate a natural habitat for up to seven astronauts and cosmonauts and to accommodate research facilities to help us understand better the space environment. The construction, development and maintenance of the International Space Station required almost 40 space flights to Low–Earth Orbit (LEO) over the last five years and more than 50 spacewalks.

While aboard ISS or during possible interplanetary flights (trips to the Moon or Mars) the space crew has to overcome a series of engineering and life support challenges. Besides the engineering challenges that would make possible interplanetary flights (i.e. developing advanced propulsion systems, telecommunication systems and software data acquisition programs), there is a variety of human adaptation issues to such long space flights. Along with the human behavior and performance, food and nutrition, bone loss and psychological factors, one of the great difficulties that need to be overcome is the biological effect of space radiation on humans.

1.2. Space radiation fields and their influence on the human body

The radiation levels in LEO are much higher that those encountered on Earth, which is protected by its atmosphere and magnetic field. The radiation exposure in LEO depends on a series of factors such as shielding, inclination of the orbit, altitude, mission duration and the time when the mission occurs during the solar cycle. The radiation environment in space is a complex variety of charged particles: galactic cosmic radiation consisting of high-energy protons, alpha particles and heavy ions that originate outside our solar system with an energy spectrum peaking at 1GeV; medium energy protons (< 250 MeV) and electrons (< 6 MeV) trapped in the Earth's magnetic field, and solar

particle radiation consisting of medium energy protons with a small alpha particle and heavy ion component (Benton and Benton, 2001). The charged particles can interact with the spacecraft walls and the space crew suits, creating secondary particles that will contribute to the total radiation exposure of the astronauts.

Particles such as γ-rays, X-rays and charged particles that are capable of ionizing the matter through which they pass have the generic name of *ionizing radiation*. A measure of the interaction of ionizing radiation with matter is the *absorbed dose*, defined as the energy imparted to matter per unit mass at a point (Attix, 1986). The SI unit for the absorbed dose is the *Gray* (*Gy*).

$$D = \frac{dE}{dm} \qquad [D]_{SI} = \frac{1\,J}{1\,kg} = 1\,Gy \tag{1.1}$$

In equation (1.1), D is the absorbed in a specific medium, dE represents the mean energy deposited per unit mass in a volume dV and dm represents the mass of the medium in the volume dV. The time derivative of the absorbed dose is called *absorbed dose rate* and represents the change in the absorbed dose in the time interval dt. The SI unit for the dose rate is expressed in Gy/s.

$$D_r = \frac{dD}{dt} \qquad [D_r]_{SI} = \frac{1\,Gy}{1\,s} \tag{1.2}$$

In equation (1.2), D_r is the dose rate, dD represents the change in the absorbed dose during the time interval dt.

The interaction of the charged particles with biological systems can result in damage to the biological cells due to the high local concentration of the absorbed energy. A charged particle passing through tissue can produce a high ionization density region along its track damaging the DNA structure near the particle path. The damage in the

DNA may interfere with the reproduction and the survival of the cell. Therefore, there are several possible biological effects of the ionizing radiation on the human cells. In some cases, the cells are damaged by radiation, but they are fixed by the repair mechanisms of the human body and still function properly. If the repair is not perfect, the result is an altered cell that can influence other cells by increasing the probability of cancer. For large radiation exposures, the cell may be prevented from reproduction or even killed. If an organ or tissue loses its function as a consequence of the radiation-induced cell killing, the effect is called deterministic. Deterministic effects occur above a threshold dose, increase in severity and occurrence with increasing dose, and may appear early or late after irradiation. Disregarding large solar particle events, the probability that the radiation in LEO can induce early deterministic effects (i.e., acute effects) is small. Late deterministic effects, such as damage to the skin and different organs (i.e., cataracts, damage to the bone marrow, malfunctions of lungs and kidneys) may appear above a threshold dose (NCRP, 1989 and NCRP, 2000).

The major risk concerning the radiation exposure in LEO comes from late cancer and hereditary effects. A radiation-altered cell may reproduce itself and result in a series of modified cells, a multiplication process that may lead to cancer. In addition, the altered cell may incorrectly transmit genetic information to the descendents of an exposed individual, giving rise to hereditary effects. These late effects are called stochastic effects. Stochastic effects are random effects and their probability of occurrence in an exposed population is proportional to the absorbed dose.

As already mentioned, the radiation field in LEO is a mix of charged particles. The quality of the radiation is characterized by the *linear energy transfer (LET)* defined as the

mean energy lost per unit particle track length in a material. The linear energy transfer has units of keV/μm. Different types of radiation have different biological effects on the human body. This is taken into consideration by weighting the absorbed dose by a factor, called the *quality factor*, related to the quality of the radiation. The corrected absorbed dose is called the *dose equivalent* and is defined as:

$$H = \int Q(L)\, D(L)\, dL \qquad [H]_{SI} = \frac{1\ J}{1\ kg} = 1\ Sv \tag{1.3}$$

In equation (1.3), H is the dose equivalent, $Q(L)$ is the quality factor for a specific LET and $D(L)$ is the absorbed dose (defined at a specific point in tissue) from a radiation with linear energy transfer between L and $L + dL$. The SI unit for the dose equivalent is the *Sievert* (*Sv*).

The International Commission on Radiological Protection (ICRP 60, 1991) recommended the following LET dependence of the quality factor. It can be noticed in Figure 1.1 that Q has a constant value of one for $LET < 10\ keV/\mu m$ and a strong dependence for $LET > 10\ keV/\mu m$.

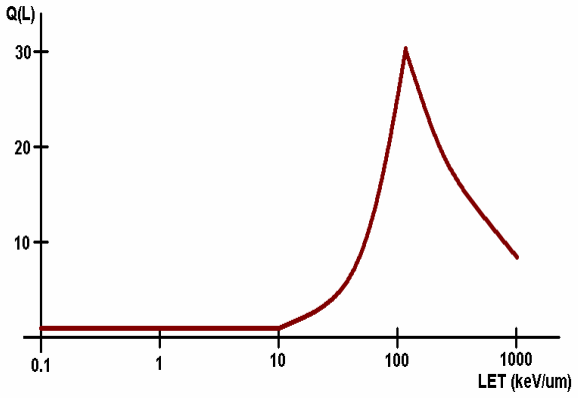

Figure 1.1. The quality factor dependence on the LET in keV/μm based on the ICRP (1991) recommendation

The ionizing radiation and can be categorized in low-LET radiation for LET < 10 keV/μm (i.e., gamma rays, X-rays and electrons) and high-LET radiation with LET > 10 keV/μm. (i.e., alpha particles, heavy ions and neutrons). The biological effects of the low-LET radiation are different from those of the high-LET radiation. Low-LET radiation exposure can cause single and double strand breaks in the DNA, with the ratio between the single strand and the double strand being higher than after a high-LET radiation exposure (NCRP, 1989). Also, the cell probability to auto repair is higher following a low-LET radiation compared with a high-LET radiation.

Considering the complexity of the space radiation and its biological effects, detailed studies are needed in order to create a valid radiation protection program for astronauts in Low-Earth Orbit.

1.3. Radiation protection measures for astronauts in LEO

Extended studies have been made to investigate and monitor the biological effects induced by space radiation in order to design an appropriate radiation safety program for astronauts and cosmonauts (Badwar, 1997; NCRP, 2000 and NCRP, 2002). The management of the radiation program in LEO involves the "As Low As Reasonably Achievable (ALARA)" principle. For space radiation protection, ALARA has the purpose of "balancing the mission objectives with practical dose reduction steps" as defined by the National Council on Radiation Protection and Measurements (NCRP) (NCRP, 2002). The NCRP also recommended that the dose limits for astronauts should include the cumulative dose from space flights during the astronauts' career, the dose received from astronauts' mission duties (i.e., extravehicular activity – EVA) and any

other occupational doses received prior to their astronaut career, disregarding the dose received during medical treatment and from the background radiation on Earth. The recommended career dose limits for males and females of different ages are given in Table 1.1 (NCRP, 2000). The total detriment is obtained by adding to the 3 % lifetime risk of cancer mortality (Table 1.1) an additional 0.6 % of nominal detriment for both heritable and nonfatal effects, with a total detriment of 4.2 %.

Table 1.1. Ten-year career limits based on 3% lifetime risk of fatal cancer

AGE AT EXPOSURE (y)	FEMALE DOSE (Sv)	MALE DOSE (Sv)
25	0.4	0.7
35	0.6	1.0
45	0.9	1.5
55	1.7	3.0

In July 2003, the Bioastronautics Office of the NASA Johnson Space Center combined their efforts with the National Space Biomedical Research Institute to develop a baseline document called “Bioastronautics Critical Path Roadmap” (BCPR). One of the main tasks of BCPR is to ensure human survival in space (i.e., the ability to stay healthy and safe) during and after long-term missions to Low-Earth Orbit and beyond (BCPR, 2003). When assessing risk, the BCPR considers not only the health, safety and performance of the crewmembers during flight and immediately following the flight, but also the possible late health effects that may occur during the crewmembers’ retirement. The BCPR prioritized the risks of adverse effects from exposure to the space

environment considering three main parameters: the likelihood of the risk occurrence, the consequences of the risk and the overall mitigation status of the risk. The prioritized space radiation risks for a balanced program are presented in Table 1.2 (BCRP, 2003). The dose assumptions made in compiling Table 1.2 are the ten-year career limit dose values based on the 3% lifetime risk of fatal cancer presented in Table 1.1.

Table 1.2. The BCPR prioritized space radiation risks for a balanced program

RISK CATEGORY	RISK TITLE	RISK AREA
Red 1	Carcinogenesis caused by radiation	Radiation effects
	Late degenerative tissue effects (i.e., non-cancer mortality, cataracts and central nervous system effects)	Radiation effects
	Synergistic effects from exposure to radiation	Radiation effects
Yellow 2	Early or acute effects from exposure to radiation	Radiation effects
	Radiation effects on fertility, sterility and heredity	Radiation effects

In Table 1.2*, Red 1* is defined as "high likelihood, high consequence risks with low risk mitigation and *Yellow 2* is defined as "high likelihood/moderate consequence or moderate likelihood/high consequence risks with higher risk mitigation status". As presented above (Table 1.2), several radiation effects (i.e., carcinogenesis, cataracts and central nervous system effects) are categorized as "*Red 1* – High Likelihood, High Consequence Risks with Low Risk Mitigation Status" (BCRP, 2003).

According to BCRM, the low risk mitigation status parameter indicates that

substantial research is needed to lower the risk, emphasizing once more the importance of investigating the space radiation and its biological effects on the human body.

1.4. Space radiation detectors

The relative biological effects of the different space radiation components depend on a series of factors such as the duration of the mission, the flight altitude and the shielding provided by the spacecraft. Due to the variety of space crew routine activities inside and outside the ISS and Space Shuttle (i.e. spacewalks), there is a need to monitor the individual radiation exposure of the crewmembers, besides recording the radiation at a specific location inside the spacecraft.

There are several types of radiation detection devices currently used to measure the radiation exposure in LEO. Portable or fixed area monitor devices are used to measure the radiation at a specific location inside or outside the station, while personal dosimeters are carried by each crewmember to monitor their individual radiation exposure. From the operational point of view, the radiation detectors can be categorized as active detectors and passive detectors. The active detectors are used to measure the dose in real or near-real time and the currently used active detectors on ISS include tissue equivalent proportional counters (TEPCs), solid-state detectors (SSDs) and ionization chambers. A TEPC is a gas chamber detector that measures the energy deposition by charged particles (i.e., electrons, protons and heavy ions), photons and neutrons in a volume of tissue comparable to the dimension of a nucleus of mammalian cells. TEPCs can provide information about the absorbed dose (D) and the absorbed dose rate (D_r) and use the so called *lineal energy* to give information about the radiation quality as a substitute for

LET. The lineal energy was defined as the ratio between the energy deposition in a given volume by a single event and the mean chord length of that volume. The value of the mean lineal energy is often considered to be numerically equal to LET (NCRP, 2002). Solid-state detectors are sensitive only to charged particles and they measure the energy deposition by a charged particle in a medium. They can provide real-time information about LET, absorbed dose and absorbed dose rate. The NCRP recommends that SSDs should be used to measure the LET spectra inside and outside ISS. During solar particle events it is important that an electron sensitive active device, such an ionization chamber, should also be used outside the station to monitor the change in the electron flux. Considering their relatively complex electronic nature, all active detectors can be used only as area monitor detectors.

Passive detectors can be used as personal dosimeters or area monitoring dosimeters and include thermoluminescent detectors (TLDs) and plastic nuclear track detectors (PNTDs). By interaction with a PNTD such as PADC/CR-39® (i.e. polyallyl diglycol carbonate), a charged particle deposits energy in the material along the particle track. This damage trail in the PNTD can be investigated by chemical etching procedures and can give information about the linear energy transfer and the dose. The plastic nuclear track detectors are sensitive to the high-LET radiation (i.e., $LET \geq 5\ keV/\mu m$) and have a reduced sensitivity to the low-LET radiation (Benton and Benton, 2001).

Thermoluminescence detectors are detectors that emit light while heated, if previously exposed to ionizing radiation. The luminescence output is proportional to the dose deposited in the detector. Thermoluminescence detectors are mostly sensitive to the low-LET radiation for $LET \leq 10\ keV/\mu m$ and $Q = 1$, and exhibit a strongly decreasing

luminescence response with increasing LET for $LET > 10\ keV/\mu m$ for which $Q = Q(L)$. Currently used TLDs on the Shuttle and ISS are LiF:Mg,Ti and CaF_2:Tm. One disadvantage of using TLDs is the complexity of analysis due to the specific heating requirements. The possibility of using an optically stimulated luminescence dosimeter (OSLD) in LEO was advanced by the NCRP (NCRP, 2002). The optically stimulated luminescence (OSL) signal is obtained from an irradiated OSL material during its stimulation with light. One of the advantages of using OSLDs (instead of TLDs) would be the possibility of providing all optical, small, and lightweight, low-power OSL readers to be used on the Shuttle or ISS so that the astronauts could read their own dosimeters during long duration flights. An example of OSL dosimeter is Al_2O_3:C that gained recognition in 1999 when Landauer Inc. developed the Luxel personal dosimeters (i.e., Al_2O_3:C used in OSL mode). This device currently represents 25% of the approximately five million personal dosimeters being used in radiation working environments throughout the world (Bøtter-Jensen et al., 2003).

The complexity of the space radiation environment requires several types of passive dosimeters to be used simultaneously in order to measure the absorbed dose as accurately as possible and over as wide a range of LET as possible. The National Council on Radiation Protection and Measurements (NCRP) recommended in 2002 that:

"A measurement package consisting of a thermoluminescent dosimeter (TLD) or optically stimulated luminescence dosimeter (OSLD) for measurement of the low-LET component, and a stack of plastic nuclear track detectors (PNTD) to determine the high-LET component should be used for passive personal dosimetry in the complex radiation field experienced in space" (NCRP, 2002).

The objective of this work is to investigate the feasibility of using Al_2O_3:C, in optically stimulated luminescence mode, as a personal dosimeter for astronauts. The space radiation environment is a complex variety of charged particles, making it imperative to study the luminescence response of the proposed OSL material (Al_2O_3:C) to several charged particle fields.

During the last four years, the optically stimulated luminescence response of Al_2O_3:C dosimeters was investigated using several exposures to both low and high-energy heavy charged particles at the Pelletron facility at the Universidad Nacional Autónoma de México (UNAM), Mexico City, and the HIMAC facility at the National Institute for Radiological Sciences in Chiba, Japan. The investigated materials were also exposed to space radiation fields as part of the STS-105 Space Shuttle mission project. The results of these exposures will be presented and discussed in detail, together with the necessary theoretical background.

CHAPTER 2

THE SPACE RADIATION ENVIRONMENT IN LOW-EARTH ORBIT

2.1. Space radiation fields

The radiation spectrum in Low-Earth Orbit consists of several types of charged particles: protons, electrons, alpha particles and heavy ions (up to uranium $Z = 92$). The main sources of radiation in LEO are:

1. Galactic cosmic rays (GCR) that contain mainly protons with small helium, heavy ions and electron components. The GCR energy spectrum peaks around 1 GeV.
2. Van Allen Belts (i.e., trapped protons and electrons in Earth's magnetic field) that contain medium energy protons (up to 250 MeV) and electrons with energies up to 6 MeV (Benton & Benton, 2001).
3. Solar particle radiation has a significant contribution to the radiation environment in LEO when very large solar particle events occur and consists mostly of low energy protons and electrons.
4. Due to the interaction of the cosmic rays with the spacecraft walls, secondary charged particles (i.e., both electrically charged and neutrally charged – neutrons) are created and they are contributing to the overall crew radiation exposure.

In order to maintain an operational radiation safety program for astronauts in LEO (i.e., ALARA – as low as reasonably achievable), a series of decisive parameters need to be considered. Thus, a good study of the space radiation environment together with the biological impact of its different components is needed. The provided shielding inside and outside the space station (i.e., spacecraft walls, space suit) also plays an important

role. Also, the prediction, duration and severity of solar particle events (SPE) are important. All of these factors are considered when assessing radiation risk limits for astronauts in LEO.

2.1.1. Galactic cosmic rays

Galactic cosmic rays (GCR) are charged particles that originate outside our solar system. Victor Hess discovered the GCR in 1912 during a high-altitude balloon experiment and he was awarded the Nobel Prize (1936) for his discovery. He noticed that an electroscope discharged faster with increasing altitude and he attributed this observation to a radiation source entering the Earth's atmosphere "from above" (Mewald, 1996). Galactic cosmic rays consist of 98 % nuclei (i.e., protons and heavy ions) and 2 % electrons and positrons. The nuclear component contains about 87 % protons, 12 % helium ions and 1 % heavy ions (Simpson, 1983). The GCR spectrum contains particles with energy values between 1 MeV/n up to 10^{14} MeV/n.

Galactic cosmic rays are one of the most important radiation sources outside our solar system. The distribution of GCR throughout the interplanetary space is isotropic in nature and therefore it is hard to predict their origin. One of the first hypotheses related to the origin of the GCR was that the particles already present in the interplanetary medium interacted with the wave shocks from a supernova producing cosmic rays. New theories suggest that the cosmic rays are produced and accelerated through the interstellar space by supernova remnants (SPN), such as the Crab Nebula. This theory is based on the observation of the synchrotron radiation emitted by cosmic ray electrons spiraling around the magnetic field lines of the SPN (Simpson, 1983). Nevertheless, the question still

remains whether the source of GCR lies either inside or outside our solar system, or maybe a mixture of both.

The measured relative abundance of elements from hydrogen to nickel in galactic cosmic rays (relative to silicon) was measured and compared with the solar system abundances for the same nuclei. This comparison is represented in Figure 2.1 (Simpson, 1983). It can be noticed that there are important differences in the elemental abundance between the solar system matter and the source matter of GCR, indicating that one of the probable sources responsible for the GCR production lies outside our solar system.

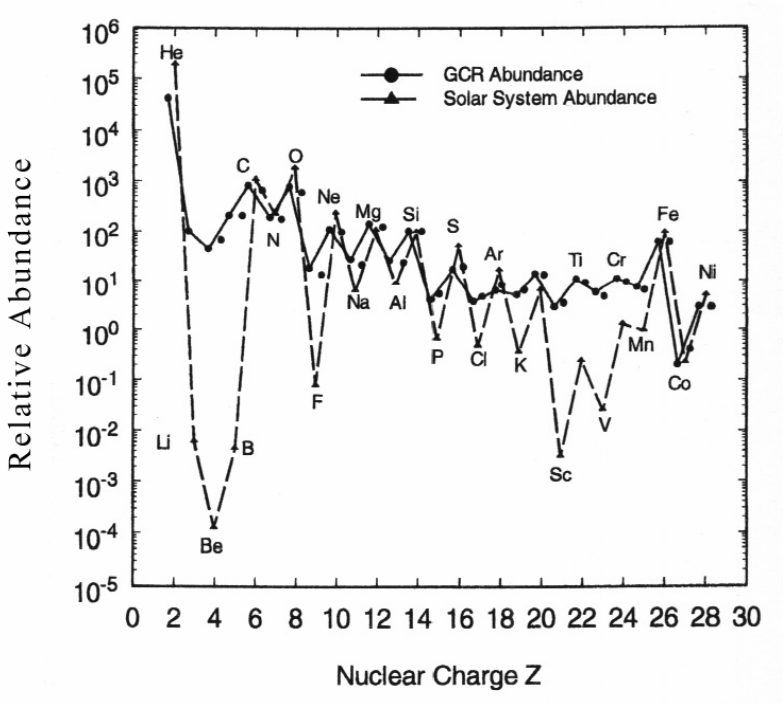

Fig. 2.1. The GCR abundances from H to Ni (black circles) compared to the solar system abundances (black crosses) (Simpson, 1983)

Galactic cosmic rays are also affected by Earth's magnetic field that provides a significant shielding for the spacecraft while in Low-Earth Orbit. The Earth's magnetic field lines are parallel to the Earth surface at the Equator and point toward the Earth

surface at the poles. Therefore, a space vehicle in LEO passing near the South and North Pole would receive a large amount of GCR, while passing near the Equator region the GCR would decrease. When high-energy GCR interact with the Earth atmosphere secondary particles (i.e., pions, muons, neutrinos and gamma rays) are produced that contribute to the total background radiation on Earth. Nevertheless, the incidence of these high-energy GCR is pretty small, thus their overall contribution is insignificant.

The GCR flux in Low-Earth Orbit is modulated by the solar activity. GCR with energies smaller then 1GeV/n exhibit a decrease in their flux due to interactions with the solar wind. When the solar activity is low the solar wind decreases. The GCR flux reaches its maximum value for solar minimum, whereas in the case of the solar maximum the flux is at its lowest value. The flux of the elements that contribute the most to the GCR (i.e., protons, helium, oxygen, and iron), for both solar minimum and solar maximum, is shown in Figure 2.2 (Benton & Benton, 2001).

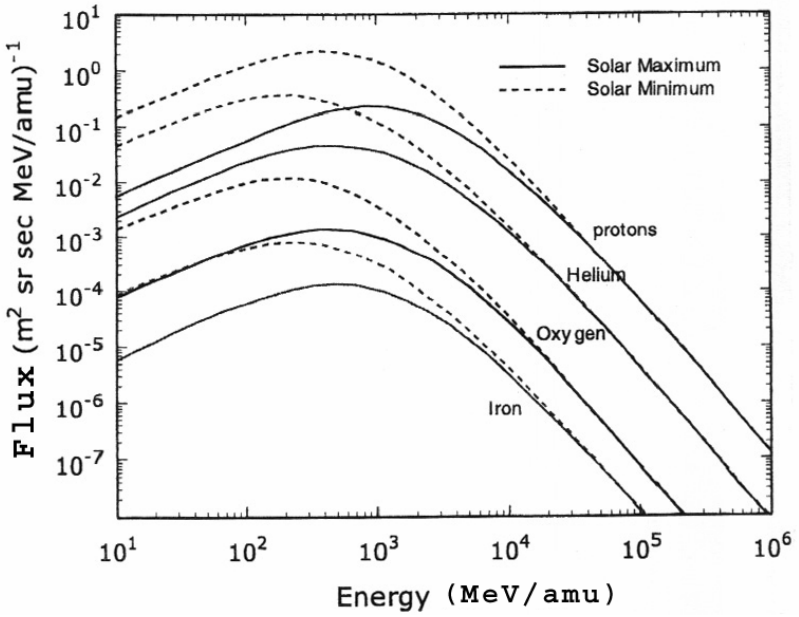

Figure 2.2. The flux dependence of some of the main GCR elements (H, He, O and Fe) on solar activity (Benton & Benton, 2001)

The GCR spectrum has also an "anomalous" component that causes an increase in intensity with decreasing energy. Anomalous cosmic rays are electrically neutral particles from outside our solar system and consist mainly of He, N, O Ne and Ar. Their intensity is influenced by the solar modulation, varying two orders of magnitude over the solar cycle. Due to their low energies (energies too small to penetrate the spacecraft's shielding), the anomalous cosmic rays are not expected to contribute to the overall astronaut radiation exposure.

2.1.2. Trapped particles in the Earth's magnetic field

As already mentioned in Chapter 1, the Explorer I mission in 1958 brought its contribution to space radiation science by the discovery of the trapped radiation belts. Van Allen discovered the Earth's trapped radiation belts, using a Geiger counter that detected unexpected anomalies in the fluence of energetic charged particles. At about 500 km altitude the counter's rate was thirty counts per second (the usual count expected from the cosmic rays), but at about 2000 km altitude the detector indicated zero counts per second. The experiment was repeated during the Explorer III mission, when an increase of the count rate to the maximum, followed by a zero counts per second reading was observed repeatedly. Van Allen suggested that the detector was actually saturated by the large number of detected particles, indicating zero counts per second as a result of this saturation. Also, he suggested that the large flux of particles was trapped by the Earth's magnetic field forming the so-called Earth's trapped radiation belts.

Radiation belts are mainly composed of protons and electrons, but they also contain

some energetic ions such as helium, carbon and oxygen. The trapped electrons have an insignificant contribution at low altitudes (i.e., smaller than 700 km) and do not pose a threat for astronauts. Thus, for a spacecraft in LEO, the main contribution to dose rate comes from the trapped protons. The trapped protons flux is influenced by both the solar activity and by altitude. At a fixed altitude the proton fluxes (i.e., measured in terms of dose rate) decrease as the solar activity increases, whereas at constant solar activity the trapped protons dose rate increases almost exponentially with altitude (Badhwar, 1997).

Charged particles trapped in the Earth's magnetic field have a helical motion around the geomagnetic field lines that consists of a sliding motion along the field lines and a bouncing motion along a line between the trapped particle's mirror points (Hess, 1968). In addition to the helical motion, there is also a longitudinal drift around the Earth, with electrons drifting East and protons West. The South Atlantic Anomaly (SAA) region (i.e., South Pacific region where the spiraling protons get closer to Earth than usual) is an important source of radiation exposure for crewmembers whose spacecrafts are traveling at low orbit inclination and low altitude (NCRP, 1998). Such spacecraft (i.e., the Shuttle and ISS) can pass through the SAA region and receive their maximum exposure to trapped protons. At solar minimum, for ISS and MIR usual orbital inclination of 51.6° and altitude of approximately 400 km, almost half of the ionizing radiation comes from SAA trapped protons, while the other half comes from GCR (Badhwar, 1997).

2.1.3. Solar particles radiation

Solar particles consist of protons, electrons and a small component of heavy charged particles up to iron. Due to the high relative abundance and their high energies, solar

protons are the most relevant to the crew's health. Large solar particle events (i.e., energies larger than 10 MeV and fluences greater than 10^7 part/cm^2) are considered to be the most dangerous for astronauts in LEO. Such large SPEs are rare and only a few can be expected per solar cycle (Badhwar, 1997). Currently, there are no available methods to predict the magnitude and the occurrence of these large events. Nevertheless, their frequency can be related to the solar activity, thus improving the chances of forecasting SPE. One of the orbital satellites used to try to predict solar particle events is the Geosynchronous Orbit Earth Satellite (GOES) that provides a continuous monitoring of the proton flux. Once a solar flare occurred, is much easier to predict the following flare. Thus, one approach in predicting a SPE is to look at the characteristics (i.e., amount and types of radio emissions) of recent solar flares in order to determine the occurrence and the maximum fluence rate of the next SPE. A schematic SPE time-intensity profile at 1 AU (i.e., astronomical unit) is shown in Figure 2.3 (Shea & Smart, 1990).

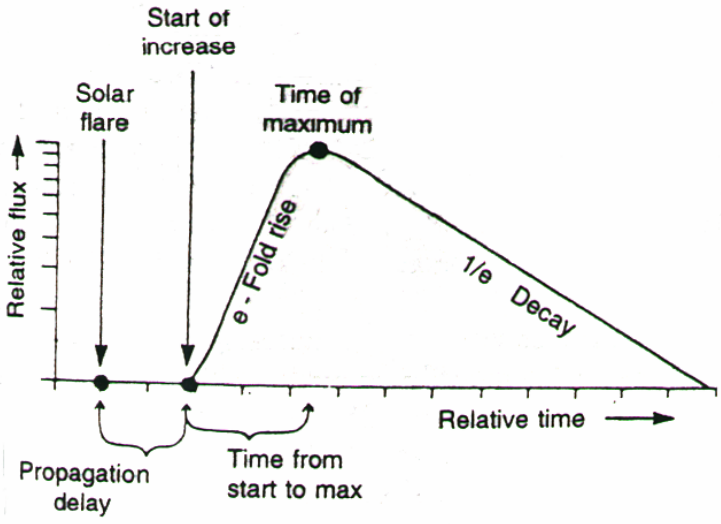

Figure 2.3. Time-intensity profile of a solar particle event at 1 AU (Shea & Smart, 1990)

There is a time difference between the onset of the SPE and the detection of the first solar

particles. After this delay time, the flux intensity is observed to increase exponentially up to a maximum value, followed by a slow decay back to the background. For large SPE, such the October 1989 event, an additional peak can arise due to the interplanetary shock waves produced by coronal mass ejections (Benton & Benton, 2001). For protons with energies of 10 MeV, the delay time is typically 15 hours with a range of 15 minutes to 60 hours (Shea & Smart, 1990). For larger events, the rise time to the maximum of the solar particles flux can be of the order of days. The total duration of an SPE event can last from hours to weeks. The provenance of the SPE was subjected to various speculations over the years. Initially, it was assumed that the solar flares were the source of the energetic particles observed in space. An increase in the SPE fluence rate was observed in correlation with the solar flare events, but only half of the solar proton events could be directly correlated with the solar flares (Smart & Shea, 1997). The second hypothesis suggested that the energetic particles observed in space are the result of acceleration associated with the interplanetary shocks generated by fast coronal mass ejections (Reames, 1995). It has been proved that both assumption are correct and that indeed, there are two types of solar particle events, ones produced by impulsive solar flares and others associated with large coronal mass ejections (CMEs). The first category of SPE is characterized by large electron fluxes, small fluences and they are short-lived (i.e., order of hours). The second type of SPE (i.e., associated with CME) consists of large proton fluxes with large fluences and they can take place for a few days.

The energy spectra of some of the major solar particle events over the last four solar cycles are shown in Figure 2.4 (Benton & Benton, 2001). One of the most intense SPE events occurred between October 19 and November 10, 1989 when the protons reached

1AU (i.e., astronomical unit) after 10 days. The second most intense SPE took place in August, 1972 when almost all of the dangerous energetic protons reached 1AU in 15 hours.

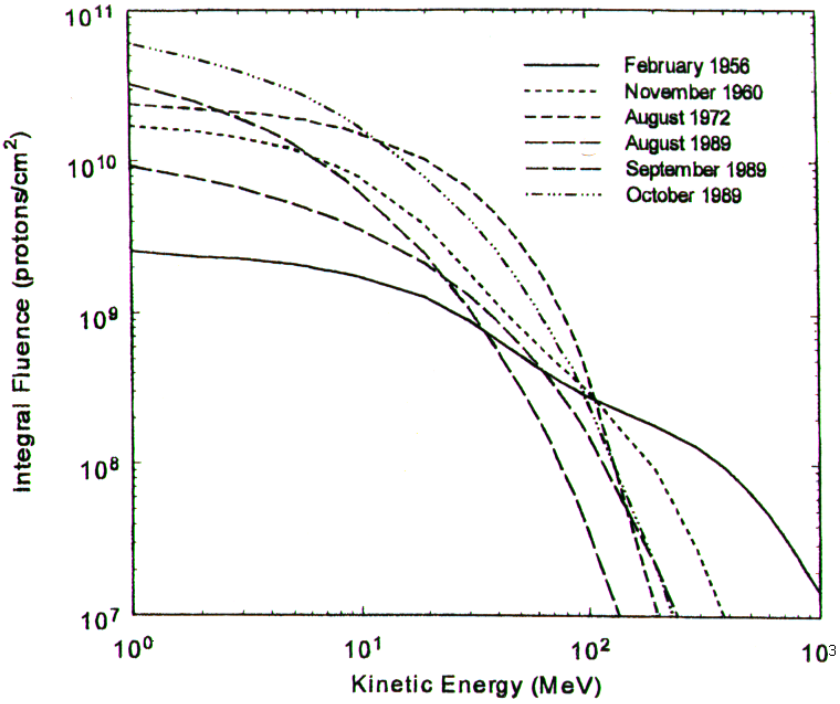

Fig. 2.4. Integral proton fluence for several large SPE events (Benton & Benton, 2001)

2.1.4. Secondary particles

High energy charged GCR particles can interact with the spacecraft walls and undergo nuclear reactions, producing high and low – energy secondary particles that can be even more penetrating than the primary particles. These high-energy secondary particles (i.e., high-energy neutrons and protons, large projectile fragments) have energies larger than 50 MeV/n and can pose a threat both inside and outside the spacecraft and the EVA space suit (NCRP, 2002). Target fragments have short range and energies smaller than 10 MeV/n, thus being able to produce substantial damage within the human body.

These secondary particles (i.e., protons, neutrons, alpha particles, and recoil heavy nuclei) need to be measured only inside the spacecraft and the EVA suit.

GCR can also interact with the atmosphere and produce the so-called *splash albedo electrons* and the *reentrant electrons* that contribute to the total electron dose in LEO. The splash albedo electrons are scattered upward as a result of the nuclear interactions between the GCR and the atmosphere. The reentrant electrons are decay products of the nuclear interactions. The effect of the reentrant electrons on bone marrow was studied by Badhwar and colleagues (2001). It was observed that the contribution of the reentrant electrons to the bone marrow dose was more than ten time larger than the contribution of the trapped electrons. Thus, Badhwar and colleagues suggested that the effects of secondary electrons should be considered when estimating the crew radiation exposure in LEO (Badhwar et al., 2001).

Secondary particles can also be obtained as a result of the interaction of the trapped protons and the protons from SPE with the spacecraft. Nuclear interactions will produce low-energy target fragments (i.e., $Z = 1, 2$ and neutrons). The neutron component of the radiation environment in LEO is also important. Neutrons are highly penetrating particles and their contribution to the total dose equivalent is function of energy. Thus, for neutron energies smaller than $1\,\text{MeV}$ only $5\,\%$ of the total dose is attributed to neutrons, while model calculations show that the neutrons with energies between $1\,\text{MeV}$ and $10\,\text{MeV}$ contribute $50\,\%$ of the total dose equivalent (Badhwar et al., 2001). Recent Monte Carlo transport calculations made by Armstrong & Colborn (2001) suggest that the secondary neutrons with energies between $0.1\,\text{MeV}$ and $100\,\text{MeV}$ have a total contribution of about $50 - 60\,\%$ to the total dose equivalent.

2.2. Radiation protection parameters for stochastic and deterministic effects

So far, we have discussed radiation protection quantities such as the absorbed dose and the dose equivalent. In an attempt to characterize better the impact of ionizing radiation on the human body, factors such as the energy and type of the ionizing radiation together with the type of the exposed tissue need to be considered. From the radiological protection point of view, the absorbed dose averaged over a tissue rather than at a point is of importance. Thus, the mean absorbed dose in an organ or tissue can be weighted by a factor w_R (i.e., radiation weighting factor) that corrects for the relative biological effectiveness of the specific radiation. For stochastic effects, the result is the *equivalent dose* in a tissue or organ and is given by (NCRP, 2000):

$$H_t = \sum_R w_R \, D_{t,R} \qquad [H_t]_{SI} = 1\,Sv \tag{2.1}$$

In equation (2.1), $D_{t,R}$ is the absorbed dose averaged over the tissue t due to radiation R.

Besides the energy and type of radiation, the biological effects depend on the dose distribution inside the body. In order to account for this dependence another weighting factor was introduced. This new factor, called *tissue weighting factor*, represents the relative contribution of the specific organ or tissue to the total detriment due to the stochastic effects. The tissue weighting factor is calculated by taking into consideration factors such as the mortality risk from cancer, the risk of severe hereditary effects for all generations, and the length of life lost. The weighted equivalent dose by w_t is called the *effective dose* and represents the sum of all of the equivalent doses in all the organs and tissues of the body and is used to account for all stochastic effects (NCRP, 2000):

$$E = \sum_{R} w_t \; H_t \qquad [E]_{SI} = 1 \; Sv \tag{2.2}$$

where E is the effective dose and H_t is the equivalent dose in a tissue or organ. The ten-year career limits for delayed stochastic defects are expressed in terms of effective dose, E and are shown in Table 1.1 (Chapter 1). The stochastic limits are presented as function of gender and age and they are estimated considering a ten-year carrier limit.

All radiation protection quantities discussed so far were related to the stochastic effects. For deterministic effects, the mean absorbed dose in an organ or tissue is multiplied by a recommended value of relative biological effectiveness to obtain a quantity called the *gray equivalent* (NCRP, 2002):

$$G_t = \sum R_i \; D_t \qquad [G_t]_{SI} = 1 \; Gy - Eq \tag{2.3}$$

where, G_t is the gray equivalent, R_i is the recommended value of the relative biological effectiveness for a particle i and D_t is the mean absorbed dose in an organ or tissue. The name of the unit for the gray equivalent is *Gy-Eq*. The dose limits for the deterministic effects are expressed in terms of gray equivalent, G_t and are presented in Table 2.1 (adapted from NCRP, 2002). The recommended G_t limits depend on the type of tissue (i.e., bone marrow, skin) and the length of the career. The career dose limits (i.e., presented in Table 1.1) are intended for protection against delayed stochastic effects, while the dose limits for bone marrow, skin, and the lens of the eye are for protection against deterministic effects (i.e., as shown in Table 2.1).

As a conclusion, close monitoring and recording of the doses received by astronauts while in space, for both individual missions as well as cumulative career activities are imperatively needed.

Table 2.1. Deterministic dose limits for astronauts expressed in G_t

CAREER	BONE MARROW (*Gy-Eq*)	LENS OF THE EYE (*Gy-Eq*)	SKIN (*Gy-Eq*)
30 days	0.25	1.0	1.5
1 year	0.50	2.0	3.0
career	-	4.0	6.0

CHAPTER 3

OPTICALLY AND THERMALLY STIMULATED LUMINESCENCE PHENOMENA

3.1. Luminescence materials and applications: Overview

The thermoluminescence (TL) method has been one of the most investigated luminescence dosimetry methods over the past fifty years (Bräunlich, 1979; McKeever, 1985; McKeever et al., 1995; Chen & McKeever, 1997). The TL technique is used in radiation dosimetry to measure the absorbed dose in a material previously exposed to radiation, by linearly heating the sample and monitoring the luminescence emission (TL). The TL signal is directly proportional to the absorbed dose over a wide range of doses. The TLD materials are used as radiation detectors in several radiation dosimetry areas, such as personal dosimetry, environmental dosimetry, medical dosimetry, and retrospective dosimetry (i.e., accident dosimetry, archeological artifacts and TL dating of sediments). For personal and medical dosimetry, the main interest has been focused on LiF:Mg,Ti, while for the environmental and dating dosimetry materials such as quartz and feldspars are the most used.

The optically stimulated luminescence (OSL) method is similar in essence to thermoluminescence, with the difference being in the stimulation source. The OSL signal is obtained by stimulating an irradiated material with light. The intensity of the OSL signal is proportional to the absorbed dose. Huntley et al. (1985) was the first to perform a so-called *continuous-wave OSL* (CW-OSL) experiment in the lab using feldspars and

quartz. Since then, optically stimulated luminescence has become a popular technique in the retrospective dosimetry community (McKeever et al., 1997b; Aitken, 1998; Bøtter-Jensen et al., 1999b; Wintle & Murray, 2000). The use of the OSL method has also started to gain recognition in fields like personal and medical dosimetry. One of the most studied OSL materials is Al_2O_3:C, which has applications in personal, medical and retrospective dosimetry (McKeever et al., 1996; Akselrod et al., 1998b; Akselrod & McKeever, 1999; Bøtter-Jensen et al., 1999a; McKeever, 2001; Polf et al., 2002; Gaza & McKeever, 2003). The OSL technique has several advantages over the TL method, advantages that lie in its all-optical nature. The differences between the techniques pertinent to each type of application are discussed in the following sections.

3.1.1. Personal Dosimetry

About 85% of the average individual radiation exposure comes from natural sources (i.e., gamma rays from buildings and ground, radon from the ground, and cosmic rays), while the remaining 15% is from artificial radiation exposure from medical and occupational sources (i.e., X-rays, radioactive discharges and nuclear plants), as shown in Figure 3.1. The total radiation dose coming from these sources is approximately 3 mSv/y (global average). Several types of radiation detectors have been used to monitor the individual radiation exposure, including TLDs and OSLDs. One of the important requirements for such detectors is that they are tissue-equivalent (i.e., to have an effective atomic number Z_{eff} close to that for tissue, $Z_{eff}^{tissue} = 7.6$). From this point of view, LiF:Mg,Ti with $Z_{eff}^{LiF} = 8.3$ has a slight advantage over the Al_2O_3:C ($Z_{eff}^{Al2O3} = 10.5$). An important parameter to be considered is the high sensitivity of the dosimeter over a wide

dynamic range of doses. With the subsequent development of the Luxel™ personal dosimeters that use Al_2O_3:C in a so-called *pulsed optically stimulated luminescence* (POSL) mode, one can monitor the radiation dose over a large dose range by varying the stimulation power (i.e., 1 μGy up to 10 Gy). Furthermore, due to its high sensitivity, the dosimeter can be read for a short period of time without totally depleting the signal. This OSL method allows the user to re-read the samples obtaining independent measurement results. This feature makes the OSL method more attractive than TL for which the luminescence signal is completely destroyed after one reading.

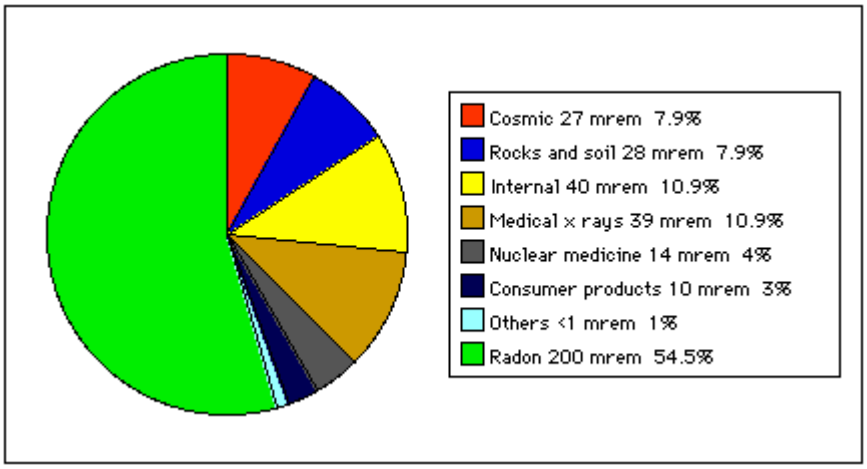

Figure 3.1. Natural and artificial sources of radiation on Earth (data obtained from the National Council for Radiation Protection and Measurements[ii])

Another side of personal dosimetry concerns monitoring the astronauts' radiation exposure while in space. The general requirements for a space dosimeter is to be tissue-equivalent, to have a high sensitivity at low doses and insignificant fading of the luminescence signal with time (i.e., for long space missions). Both LiF:Mg,Ti used in TL mode and Al_2O_3:C used in OSL mode are suitable for passive dosimetry applications in

[ii] Document found on the Internet (September 2004)
http://users.rcn.com/jkimball.ma.ultranet/BiologyPages/R/Radiation.html

Low-Earth Orbit for the low-LET part of the spectra. Nevertheless, the advantages of using OSLD materials instead of TLDs are outlined by the National Council on Radiation Protection and Measurements in the NCRP Report 142, (2002): "One advantage of switching to OSLDs would be the possibility of providing small, lightweight, low-power OSL readers for spacecraft so that the astronauts could read their own dosimeters during long duration flights."

3.1.2. Medical Dosimetry

During the traditional medical dosimetry procedures (i.e., radiotherapy) the radiation dose delivered to the patients is calculated in advance and usually measured by TLD dosimeters placed on the surface of the body. However, the efficiency of the medical treatment ideally requires *in vivo* measurements of the radiation dose as recommended by the International Commission on Radiological Protection (ICRP, 2000). As a result, the TL technique is being replaced by the OSL method that allows performing real-time measurements. For minimally invasive in vivo radiation measurements, the dimensions of the dosimeter are critical. Thus, Polf and colleagues (2002) investigated the luminescence characteristics of Al_2O_3:C optical fibers (i.e., 800 μm diameter and 5 mm length) to be used as real-time OSL dosimeters for possible radiotherapy applications. Gaza (2004) designed and build an operational real-time portable OSL system using both Al_2O_3:C and KBr:Eu optical fibers that were successfully tested in a clinical environment.

3.1.3. Environmental Dosimetry

For environmental radiation monitoring, parameters such as high sensitivity and

stability with respect to external factors (i.e., temperature changes) are important. Besides the TLD materials frequently used for environmental applications, Bøtter-Jensen and colleagues (1997) also used the OSL of Al_2O_3:C for short time assessment of the environmental gamma dose rates. The possibility of developing low-power portable OSL readers for environmental applications was investigated by Klein et al. (2004). The POSL system build by Klein et al. (2004) was able to detect low doses, with a minimum detectable dose of 5 μGy.

3.1.4. Accident and Dating Dosimetry

There is an increasing interest in the retrospective assessment of the radiation dose for accidentally contaminated areas such as Chernobyl. For this purpose, natural materials (i.e., quartz and feldspars) from the accident site are used either in TL or OSL mode to provide information about the incident radiation (Bailiff, 1995). Another retrospective dosimetry application is the dating of geological or archeological samples and consists of measuring the dose absorbed by natural minerals (i.e., quartz and feldspars) since their last heating or light exposure. Thus, the absorbed dose during this period is proportional to the age of the sample (Aitken, 1998):

$$age = \frac{natural\ TL/OSL\ signal}{(TL/OSL\ per\ unit\ dose) \times natural\ dose\ rate} \tag{3.1}$$

Here, the $natural\ TL/OSL\ signal$ is the luminescence signal accumulated in the sample since its last resetting, the $TL/OSL\ per\ unit\ dose$ represents the TL/OSL sensitivity of the sample, and the $natural\ dose\ rate$ represents the rate of which the energy was deposited in the sediments.

3.2. Luminescence processes

The energy structure of a crystalline material can be best described by the energy band model. When atoms are brought together in a solid to form a crystalline lattice, the wave functions of their electrons overlap. As a result, the discrete energy levels of the individual atoms will merge into quasi-continuous energy bands. The bound electrons will have energies within the so-called *valence band* (VB), while free electrons will have energies contained in the so-called *conduction band* (CB). These two 'allowed' bands are separated by 'forbidden' energy regions. The gap between the uppermost filled valence band and the lowermost filled conduction band is called *band gap.* For a semiconductor or insulator at $T = 0\ K$, all the electrons are confined to the valence band, while the conduction band is completely empty (Kittel, 1996).

In an ideal crystalline material, there are no permitted energy levels within the band gap. However, in real crystals, due to the presence of impurities within the lattice and lattice structural defects such as lattice vacancies and dislocations, multiple discrete energy states appear within the 'forbidden' region. For such materials, the existing defect states are localized energy levels and they exhibit statistical behavior acting either as trapping states, **T** or as recombination centers, **RC**, as illustrated in Figure 3.2. For electrons, if transition **(I)** is more probable than transition **(II)**, the energy level is called *trap*. Reversely, if the transition **(II)** is more probable than transition **(I)**, the defect center corresponds to a *recombination center*. The recombination process can be non-radiative or can take place with light emission. When the recombination process is radiative, *luminescence* occurs. Radiative recombination centers are also called *luminescent centers* (**LC**).

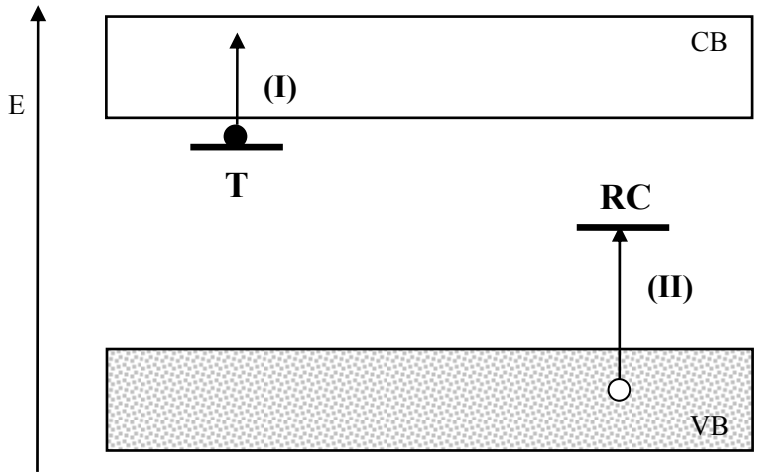

Figure 3.2. Schematic diagram of localized energy states for electrons in real crystals

Detailed schematics of several electronic transitions corresponding to trapping and recombination of the charge carriers involving both continuous bands (i.e., **VB** and **CB**) and localized energy levels (i.e., **T** and **RC**) are shown in Figure 3.3. Ionizing radiation passing through a crystal deposits energy in the lattice. Part of this energy can be transferred to electrons in the valence band. If the amount of energy absorbed by valence electrons is larger than the energy gap, the electrons are excited to the conduction band where they can move freely within the crystal, via transition (i). The freed electrons can dissipate their excess energy non-radiatively, for instance by transferring it to lattice vibrations (phonons). Alternatively, if the material contains radiative recombination centers, the electrons can be captured by them and their excess energy (or a fraction of it) is emitted as light. The possible recombinations available for the electrons in the conduction band, are *direct* recombinations (ii) or *indirect* recombinations (v,vi). Direct recombinations involve only the continuous bands, while indirect recombinations involve also the localized states.

The probability of direct recombinations is higher for narrow band-gap materials than for wide band-gap materials, depending also on temperature. An example of direct recombination is the *band-to-band* transition (ii), as shown in Figure 3.2. Band-to-band transitions have high probability for direct-gap materials (i.e., the transition can take place without momentum transfer), and low probability for indirect-gap materials (i.e., the transition can take place with momentum transfer). Indirect recombinations can take place via *band-to-center* transitions or *center-to-center* transitions. Band-to-center recombinations occur when, for instance, initially trapped electrons (iii) are released and return to the conduction band (iv), from where they recombine with holes at recombination centers (v). Another alternative for the trapped electrons is to undergo *center-to-center* transitions recombining directly with holes at **RC** (vi). This transition has high probability for close neighbor lattice defects, via tunneling processes (McKeever, 1985). If any of these recombination processes is radiative, luminescence occurs.

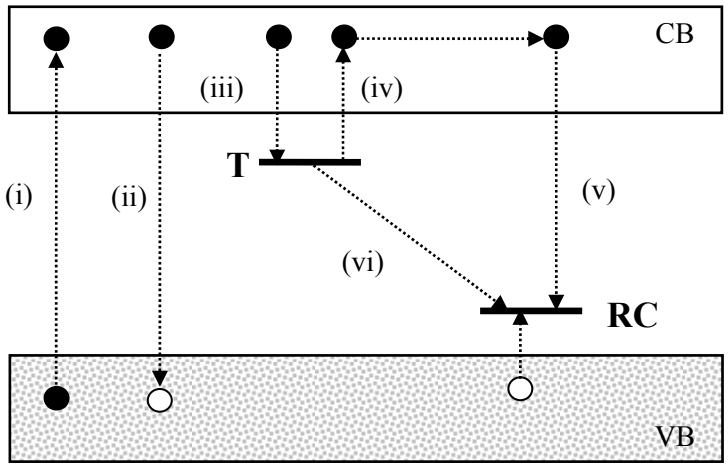

Figure 3.3. Possible electronic transitions in a doped semiconductor or insulator that may result in luminescence production

3.2.1. Phosphorescence

Since the 17th century, it has been observed that some materials glow in the dark after being exposed to heat or light for a period of time. The process was named *phosphorescence* and occurs due to particularities in the energy band diagram of the material. Natural phosphors are able to absorb energy from ambient heat/light (the excitation source), and transfer it to charge carriers, for instance electrons, which are trapped into metastable energy levels. The probability p_{th} that the electron will be thermally released from its trap depends on both the trap depth and the temperature, as follows (McKeever, 1985):

$$p_{th} = \tau^{-1} = s \exp\left(-\frac{\Delta E}{k_B T}\right) \tag{3.2}$$

Here, τ is the *mean time* spent in the trap**,** s is a constant called the *frequency factor*, ΔE is the energy difference between the localized energy level and the corresponding delocalized energy band called *trap depth* and k_B is Boltzmann's constant. The phosphorescence decays for some time after the excitation has been removed. At a given time t and for a given temperature, the decay of phosphorescence is a simple exponential decay (McKeever, 1985):

$$I(t) = I_0 \exp\left(-\frac{t}{\tau}\right) \tag{3.3}$$

In equation (3.3), $I(t)$ is the phosphorescence intensity at time t and I_0 is the phosphorescence intensity at time t_0. This simple exponential decay is considered to be valid if the probability that the excited electron will recombine is much larger than the probability that it will be retrapped**.** For some materials, the probability of detrapping p_{th}

is significant already at room temperature. For materials with trap depth ΔE much larger than $k_B T$ at room temperature, the electrons will never be released from the trap unless they receive enough stimulation energy to overcome the trap depth. When heat is used as stimulation, the process is called *thermally stimulated luminescence* or *thermoluminescence* (TL), whereas the light stimulation gives rise to the *optically stimulated luminescence* (OSL).

3.2.2. Thermoluminescence (TL)

For practical reasons, thermoluminescence is induced by linearly increasing the temperature at a rate $\beta = \frac{dT}{dt}$ (McKeever, 1985). A simple model (schematically shown in Figure 3.4) used to describe the TL production involves two defect states (e.g., a trap and a recombination center) and is called the *one-trap/one-recombination center model*.

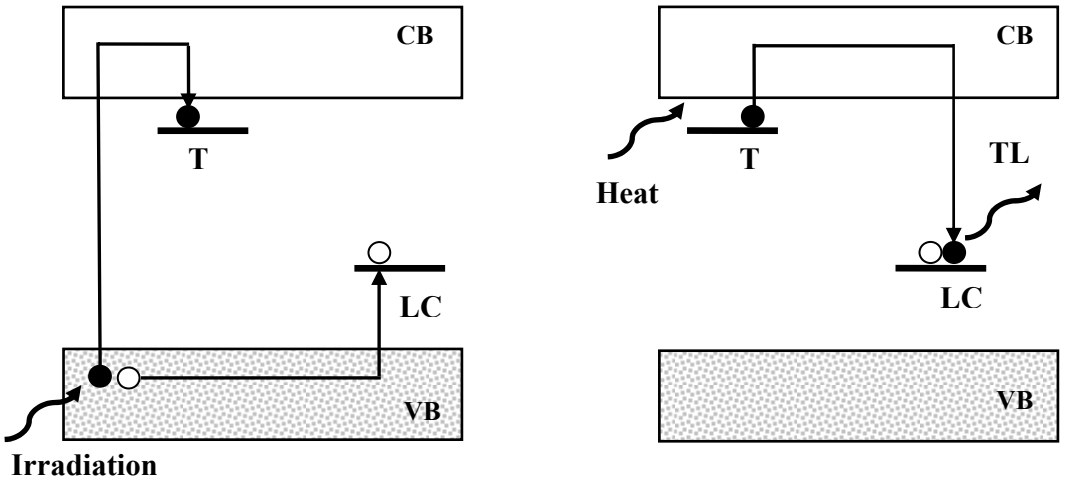

Figure 3.4. The mechanisms of TL production considering the one-trap/one-recombination center model for electrons

The TL mechanism for the one-trap/one-recombination center model is based on the same general luminescence principle already presented: after a previous irradiation of the material, the incident stimulation (i.e., heat) releases electrons from the thermally active trap that can eventually recombine with holes at the radiative recombination center leading to the corresponding TL emission. The TL signal is a convolution of two processes: the rate at which the traps are filled (during the irradiation stage) and the rate at which the electrons are released from their traps (during the heating stage). Considering this simple system, the total number of electrons equals the total number of holes. Thus, the charge neutrality equation gives:

$$n_C + n_T = m_V + m_{RC} \tag{3.4}$$

Here, n_C is the concentration of the electrons in the conduction band, n_T is the trapped electron concentration, m_V is the hole concentration in the valence band, and m_{RC} is the concentration of holes in the recombination centers. Assuming that after the irradiation ceases and just when the stimulation starts, there are no free electrons in the conduction band, nor free holes in the valence band ($n_C, m_V = 0$), the neutrality equation becomes:

$$n_T(t_0) = m_{RC}(t_0) \tag{3.5}$$

Thus, the rate equations describing the charge flow during the production of thermoluminescence are (McKeever & Chen, 1997):

$$\frac{dn_c}{dt} = -\frac{dn_T}{dt} + \frac{dm_{RC}}{dt} \tag{3.6a}$$

$$\frac{dn_T}{dt} = n_c A_T \left(N - n_T\right) - n_T p \tag{3.6b}$$

$$\frac{dm_{RC}}{dt} = -n_C A_{RC} m_{RC} \tag{3.6c}$$

In equations (3.6), p is the probability of releasing the electrons from the trap and is related to the trap depth and the frequency factor as follows:

$$p = s \exp\left(-\frac{\Delta E}{k_B T}\right) \tag{3.7}$$

where s is the frequency factor and ΔE is the trap depth. The other parameters in equations (3.6) represent: A_T and A_{RC} are the trapping and recombination probabilities, respectively (both expressed in units of $m^{-3}s^{-1}$) and N is the concentration of the available electron traps (in units of m^{-3}). In order to solve the rate equations for the TL intensity $I_{TL}(t,T)$, two main approximations are considered (McKeever, 1985):

i. The so called 'quasi-equilibrium approximation' that assumes a quasi-stationary population of free electrons in the CB (i.e., $n_C << n_{T,}\, m_{RC}$ and $\frac{dn_C}{dt} \approx 0$). As a result, $\frac{dn_T}{dt} = \frac{dm_{RC}}{dt}$.

ii. The 'slow re-trapping' approximation, where $n_c A_T \left(N - n_T\right) << n_T p, n_c A_{RC} m_{RC}$.

Considering these two approximations, the thermoluminescence intensity $I_{TL}(t,T)$ has the following expression:

$$I_{TL}(t,T) = -\frac{dm_{RC}}{dt} = -\frac{dn_T}{dt} = n_T p = n_T s \exp\left(\frac{-\Delta E}{k_B T}\right) \tag{3.8}$$

Integrating equation (3.8) over time and assuming a linear temperature increase, the TL intensity becomes:

$$I_{TL}(T) = n_0 s \exp\left(\frac{-\Delta E}{k_B T}\right) \exp\left[-\left(s/\beta\right) \int_{T_0}^{T} \exp\left(-\frac{\Delta E}{k_B T}\right) dT\right] \tag{3.9}$$

where n_0 is the initial value of n_T at $t_0 = 0$ and β is the heating rate (i.e., $\beta = \frac{dT}{dt}$). Equation (3.9) was first derived by Randall and Wilkins in 1945 and is called the Randall-Wilkins expression for first-order kinetics (i.e., the recombination probability dominates the re-trapping probability) (McKeever, 1985). It can be seen that equation (3.9) has no trivial form and the TL mechanism can become even more complicated in practice, where several trap/recombination centers are responsible for the luminescence production. The theory of luminescence models assuming more than one-trap/one-recombination center has been studied in great detail over the years. These theoretical models are not to be presented here, but a detailed analysis is given by Chen and McKeever (1997).

In practice, the thermoluminescence signal is monitored as function of temperature resulting in a so-called 'glow-curve' which may contain one or multiple peaks. The shape of a glow-curve is influenced by a large number of factors such as: the material type, the type and number of the defects initially present within the material, the type and energy of the particles that form the irradiation field, the radiation dose, the pre-or post-irradiation thermal treatments (i.e., annealing) that the material was subjected to, and the TL readout parameters (i.e., heating rate). An example of a thermoluminescence glow-curve for Al_2O_3:C following a beta radiation exposure is given in Figure 3.5. The main TL peak in Al_2O_3:C appears at about 190 °C, for a heating rate of 1°C/s. The glow-curve has an apparently simple structure containing only one peak, but in fact a number of other TL peaks are known to appear at lower or higher temperatures depending on the sample type and the irradiation conditions (McKeever et al., 1999). It has been also suggested that the TL peak of Al_2O_3:C is not a single peak, but in fact a superposition of several

first-order peaks (Walker et al., 1996). The shape of this peak was found to depend on dose, such that the peak shifted to lower temperatures with increasing dose (Akselrod et al., 1996; Walker et al., 1996). The TL signal from Al_2O_3:C was also found to depend on heating rate. It has been experimentally observed that the TL output decreases as the heating rate increases, behavior not expected from the kinematics of the TL production for this material (Akselrod et al., 1990). A possible explanation of this effect is related to the thermal quenching (i.e., reduction in the luminescence efficiency with increasing temperature) of the main TL emission at temperatures close to the temperature of the main TL peak (Akselrod et al., 1998, Akselrod et al., 1999).

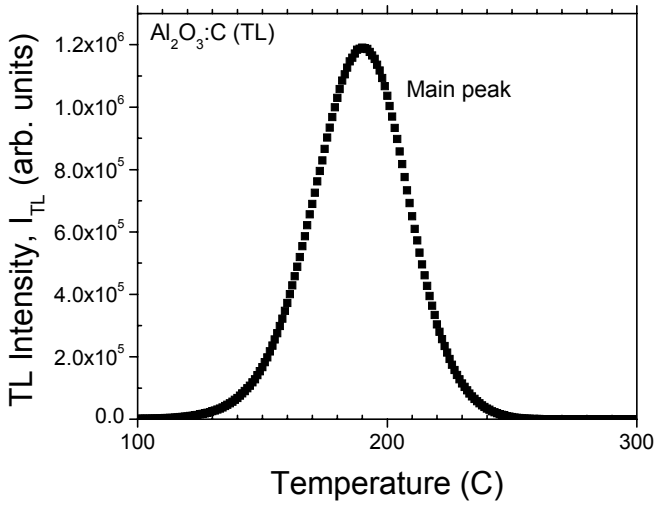

Figure 3.5. TL glow-curve of Al_2O_3:C exposed to 150 mGy using a $^{90}Sr/^{90}Y$ beta source, recorded at a heating rate of $\beta = 1\ ^{\circ}C/s$

The TL emission corresponding to the main peak in Al_2O_3:C is a broad band with a peak at about 420 nm. This emission is associated with the 420 nm emission band of F centers (oxygen vacancies with two-captured electrons), thus leading to the conclusion the F centers have an important role in the TL production from Al_2O_3:C. Also, it has

been experimentally observed that the TL sensitivity of Al_2O_3:C is strongly dependent on the concentration of F^+ centers (oxygen vacancies with one-captured electron) in the material (McKeever, 1999). The concentrations of both F and F^+ centers can be highly controlled during crystal growth. Thus, Al_2O_3:C (single crystals) are grown in a highly reducing atmosphere in the presence of carbon, resulting in F center concentrations of the order of 10^{17} cm^{-3} and F^+ center concentrations of about 10^{15} cm^{-3} (McKeever, 1999). The most probable mechanism of the TL production associated with the main peak is the recombination of an electron with an F^+ center, resulting in an excited F center that decays radiatively with the subsequent emission of a photon $h\nu_{420\,nm}$:

$$e^- + F^+ \rightarrow F^* \rightarrow F + h\nu_{420\,nm} \tag{3.10}$$

The F^+ centers can also be radiation induced, following the recombination of a hole with an F center:

$$h + F \rightarrow F^+ \tag{3.11}$$

Nevertheless, the concentration of the radiation induced F^+ centers is much smaller than the concentration of the preexisting F^+ centers (McKeever et al., 1999), thus the preexisting F^+ centers have a larger contribution to the luminescence signal.

One of the most thoroughly investigated materials for TL dosimetry applications is LiF:Mg,Ti. Several LiF:Mg,Ti versions manufactured by Harshaw are available for TL dosimetry, such as TLD-100, TLD-600 (enriched ^{6}Li) and TLD-700 (enriched ^{7}Li). In this work only the TLD-100 material was investigated. An example of a thermoluminescence glow-curve for TLD-100 is given in Figure 3.6. The TLD-100 glow curve has a complicated form with multiple peaks, Figure 3.6 showing only the first

seven peaks. The main peak is considered to be peak 5 that appears at about 220 °C. Peaks 1-4 are called *low-temperature* peaks and peaks 6 and 7 are called *high-temperature* peaks. The main TL emission in LiF:Mg,Ti at about 412 nm is believed to be due to a trimmer cluster that consists of three $Mg - Li_{vac}$ dipoles (Chen and McKeever, 1997).

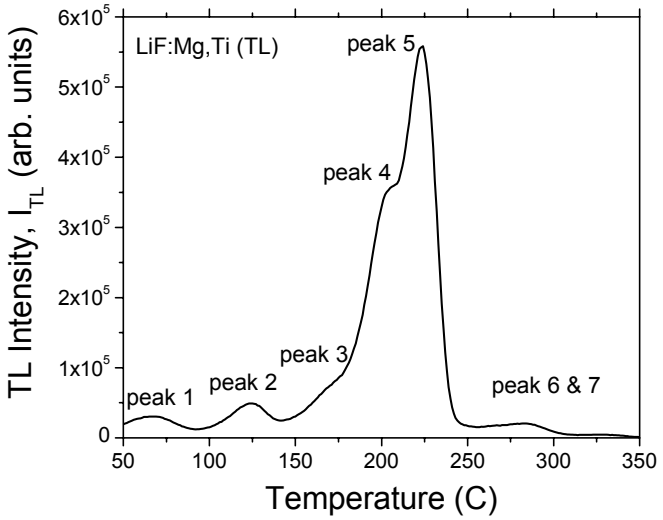

Figure 3.6. TL glow-curve of LiF:Mg,Ti exposed to a dose of 150 mGy using a $^{90}Sr/^{90}Y$ beta source, recorded at a heating rate of $\beta = 1\ ^{\circ}C/s$

3.2.3. Dosimetric requirements for TLD materials

The performance of a thermoluminescent dosimeter is evaluated by looking at properties such as sensitivity, linearity of the luminescence signal with dose, energy response, reproducibility, batch inhomogeneity, fading, influence of the environment, and others. A summary of the main dosimetric characteristics of Al_2O_3:C and LiF:Mg,Ti is given in Table 3.1 (adapted from McKeever, 1985; Akselrod et al., 1993).

Table 3.1. Summary of the main dosimetric TL properties of Al_2O_3:C (single crystal chips) and LiF:Mg,Ti (TLD-100)

TL characteristics	Al_2O_3:C (single crystal chips)	LiF:Mg,Ti (TLD-100)
Sensitivity $R(D)$	60	1
Linear range	~0.1 μGy – 10 Gy	~0.1 mGy – 10 Gy
Energy response	~3.5	1.3
Tissue equivalency (Z_{eff})	10.2	8.14
Thermal fading	< 5 % per year	5 – 10 % per year
Optical fading	*strong	< 5 % per year
Annealing procedure	900 °C for 15 minutes	400 °C for 1h 80 °C for 24 h

A. Sensitivity

The relative TL sensitivity of a specific material is defined as the TL intensity per unit dose relative to the gamma-induced TL signal from LiF:Mg,Ti (Chen and McKeever, 1997):

$$R(D) = \frac{S(D)_{material}}{S(D)_{TLD-100}} \tag{3.12}$$

In equation 3.12, $S(D)_{material}$ represents the TL signal per unit dose D for the investigated material and $S(D)_{TLD-100}$ is the TL signal per unit dose D for TLD-100. The TL sensitivity of Al_2O_3:C was found to be 60 times higher when compared to TLD-100 sensitivity, for a heating rate of 4 °C/s (Akselrod et al., 1993). The TL sensitivity of a specific material depends on dose, the particle type (charge, LET) and heating rate (i.e., Al_2O_3:C). The changes in sensitivity of TLD materials may be corrected by thermal

treatments (annealing) in order to obtain a viable thermoluminescent dosimeter. The recommended annealing procedure for Al_2O_3:C is one time annealing at 900 °C in air for 15 minutes for low doses. After that, repeated low-dose measurements can take place without a change in sensitivity (Akselrod et al., 1993). For high doses, the same annealing procedure should be repeated after each measurement. The recommended annealing procedure for Al_2O_3:C, outlined above, cannot be explained by the one-trap/one-recombination model. In real crystals, additional traps are present, which can act as competitors to the main dosimetric trap. At low doses, the competition of the deep traps (e.g., 600 °C and 900 °C traps) can be ignored and the luminescence sensitivity is constant. At high doses, as the deep traps become full, the charge surplus migrates to the main dosimetric trap resulting in an increase in the luminescence sensitivity. Thus, at high doses, annealing up to 900 °C is recommended to empty the deep traps in order to reduce the sensitivity changes. In the case of LiF (TLD-100), an annealing at 400 °C for 1 hour, followed by a long low-temperature annealing (80 °C for 24 h) is recommended for both low and high doses.

B. Dose response

In order to be able to use the TL signal to extract information about the absorbed radiation dose in a material, it is highly desirable to have a linear dependence between the luminescence signal and dose. Most of the TLD materials exhibit a linear dose response for a specific dose range, followed by a supralinear or sublinear response up to saturation. The dose response is different from sample to sample and an example of different TL dose responses from Al_2O_3:C samples exposed to beta radiation is given in Figure 3.7

(Yukihara et al., 2003).

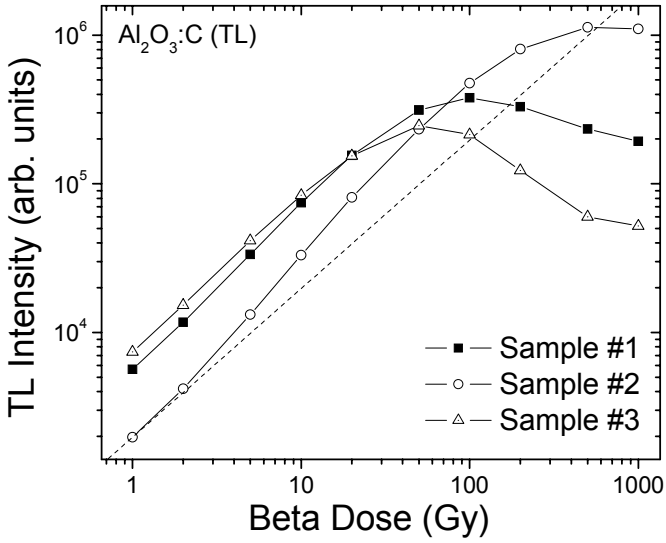

Figure 3.7. TL response of the main peak in Al_2O_3:C as function of beta dose for three different samples (Yukihara et al., 2003)

The dashed line represents the line of linearity (e.g., line of slope equal to 1). Yukihara et al. (2003) observed a linear increase of the beta-induced TL signal with dose up to about $10-20$ Gy for all of the investigated samples, followed by a small increase and then a decrease (samples #1 and #3) or a saturation of the TL signal (sample #2). This behavior was interpreted by Yukihara et al. (2003) by considering the presence of two additional competing traps (i.e., a deep electron trap and a deep hole trap) that are assumed to induce the observed supralinearity/sublinearity of the TL signal. In order to define the degree of supralinearity for a TLD material a so-called *dose response function* was introduced (Chen and McKeever, 1997):

$$f(D) = \frac{S(D)/D}{S(D_l)/D_l} \tag{3.13}$$

In equation 3.13, $S(D)$ represents the TL signal at a dose D and $S(D_l)$ is the corresponding TL signal to a dose D_l in the linear region of the dose response. Thus, if the dose response is linear $f(D)=1$, while $f(D)>1$ indicates supralinearity.

Depending on the application type, parameters such the lowest dose at which the TL response is linear and the saturation dose may become important. For low dose applications, such as environmental dosimetry (doses of order of μGy) and space dosimetry (doses of order of mGy), the minimum detectable dose is of concern. For high dose applications such as cancer radiotherapy, the dose delivered to the tumor is of the order of $1-10\,\text{Sv}$, implying the need for TL detectors with a high saturation limit. The minimal detectable dose for Al_2O_3:C is reported to be approximately $0.1\,\mu\text{Gy}$ (Akselrod et al., 1993), while for TLD-100 is $0.1\,\text{mGy}$ (McKeever, 1985).

C. Energy response

Since the intensity of the TL signal is proportional to the energy absorbed in the material during the irradiation stage, it is desired to have a TLD material that exhibits a constant response over a wide range of energies. For different energy photon irradiations, the relative energy response (RER) is defined with respect to the energy response of a reference gamma source such as ^{60}Co ($1.25\,\text{MeV}$) or $30\,\text{keV}$ photons, as follows (McKeever, 1985):

$$RER_E = \frac{S_E}{S_{30keV\ photons}} \tag{3.14}$$

When trying to asses the dose delivered to the human body (i.e., dose in tissue), an important parameter is the effective atomic number Z_{eff}. Thus, the desired TL detectors

must have Z_{eff} numbers closed to that for tissue ($Z_{eff} = 7.4$). Values of the RER ratio and Z_{eff} for Al_2O_3:C and LiF:Mg,Ti are giving in Table 3.1.

D. Thermal and optical fading

One of the characteristics of TL dosimeters is fading of the luminescence signal at room temperature. Thus, a good TLD material has low fading at room temperature and exhibits a main TL peak at about $200-250\,°C$, the temperature region where the signal is presumably stable enough (McKeever, 1985). Depending on the application (i.e., a low-temperature or high-temperature environment), appropriate choices of material and definition of the TL signal should be made. For example, for high-temperature applications, the main TL peak might show thermal fading and not be stable enough. For such applications, higher temperature peaks can be a suitable choice to define the TL signal. The TL signal of Al_2O_3:C has reduced fading ($<5\,\%$ per year) when kept in the dark, as shown in Table 3.1. It has been observed that the main TL signal of Al_2O_3:C is sensitive to light and three main light effects on the Al_2O_3:C TL signal have been investigated by Walker and colleagues (1996) and Chen and McKeever (1997):

i. The light-induced generation of the TL signal in unirradiated samples
ii. The phototransfer of charge from deep traps to shallow traps giving rise to a phototransferred TL signal (PTTL)
iii. The light-induced fading in irradiated samples. When exposed to light either during the irradiation or between the irradiation and the readout stage, Al_2O_3:C exhibits a significant decrease in the TL signal compared to the situation when the sample was kept in the dark. The optically induced fading in the TL signal of Al_2O_3:C is of

importance for this work, since this has resulted in the development of the widely used luminescence method, namely *optically stimulated luminescence* (OSL).

As a summary, Al_2O_3:C is a highly sensitive TL dosimeter (60 times higher than TLD-100) with a relatively simple glow-curve when compared to other TLD materials (i.e., LiF:Mg,Ti), good sensitivity over a wide dose range (10^{-7} – 10 Gy) , low threshold dose (~1 μGy), and low fading when stored in the dark (< 5 % per year). The material's adverse features when used in TL mode (i.e., heating rate dependence and light-induced fading) can be overcome by using the material in optically stimulated luminescence mode.

3.2.4. Optically Stimulated Luminescence (OSL)

There are several ways of performing an optically stimulated luminescence measurement. For a given wavelength (λ) and constant stimulation intensity (φ), the OSL signal is monitored as a function of the illumination time. The recorded luminescence is called *continuous-wave OSL* (CW-OSL). The integral of the luminescence signal over the stimulated period is proportional to the absorbed dose in the material. Since the luminescence emission is monitored continuously during stimulation, optical filtration is needed to discriminate between the stimulation light and the emission light. When the excitation light starts, the OSL output is observed to have a sudden increase to a maximum value, followed by an exponential-like decrease as the traps are depleted until the luminescence ends. In general, the shape of an OSL decay curve depends on the sample, the irradiation field, the specific characteristics of the stimulation light (i.e., power and wavelength), the absorbed dose and the temperature. Thus, the shape of the OSL decay can be a simple exponential, a non-exponential or a convolution

of different forms (McKeever, 2001). For optically stimulated luminescence processes, the probability (p_{opt}) that an electron is released from its trap and can recombine with subsequent emission of light is given by (Bøetter-Jensen et al., 2003):

$$p_{opt}\left(E_0\right) = \varphi\,\sigma\left(E_0\right) \tag{3.15}$$

Here, φ is the intensity of the stimulation light, σ is the photoionization cross-section of the trap, and E_0 is the optical trap depth (i.e., the minimum energy required to excite the electron from the trap to the conduction band).

During readout, the optical stimulation intensity can be linearly increased with time, $\varphi\left(t\right)$ (i.e., for a constant λ) from zero up to a maximum value. In this case, the luminescence output is known as *linear modulation OSL* (LM-OSL). The resulting luminescence vs. time curve has a peak-like shape. The parameters of the peak (i.e., peak height and peak position with time) are related with the physical characteristics of the trap involved in the production of the stimulated luminescence (Bulur, 1996) and the stimulation rate. Thus, for a given wavelength and a given power stimulation rate, traps with different photoionization cross-sections will give rise to different LM-OSL peaks.

The light stimulation can be also used in a pulsed mode, giving rise to the so-called *pulsed optically stimulate luminescence* (POSL) method (McKeever et al., 1996; Akselrod & McKeever, 1999). During a POSL measurement, the luminescence signal is monitored between pulses, rather than during the pulses As a consequence, one can use less optical filtration between the stimulation and emission light compared to CW-OSL measurements. The choice of the pulsed optical stimulation source (i.e., Nd-YAG laser) is made considering the available power, stimulation pulse width (i.e., smaller than the luminescence lifetime of the material) and frequency. By an appropriate choice of the

stimulation power, one can perform fast high-sensitivity measurements using POSL. A diagram showing the difference in stimulation for the previously discussed optically stimulated luminescence mechanisms (i.e., CW-OSL, POSL and LM-OSL) is shown in Figure 3.8. Several mechanisms of producing OSL together with their mathematical models are discussed by McKeever and colleagues (McKeever et al. 1997a). These models start with the simple model of one electron trap and one hole trap (recombination center), followed by more difficult approaches where competing traps and recombination sites are added to original model (McKeever, 2001; Bøtter-Jensen et al., 2003).

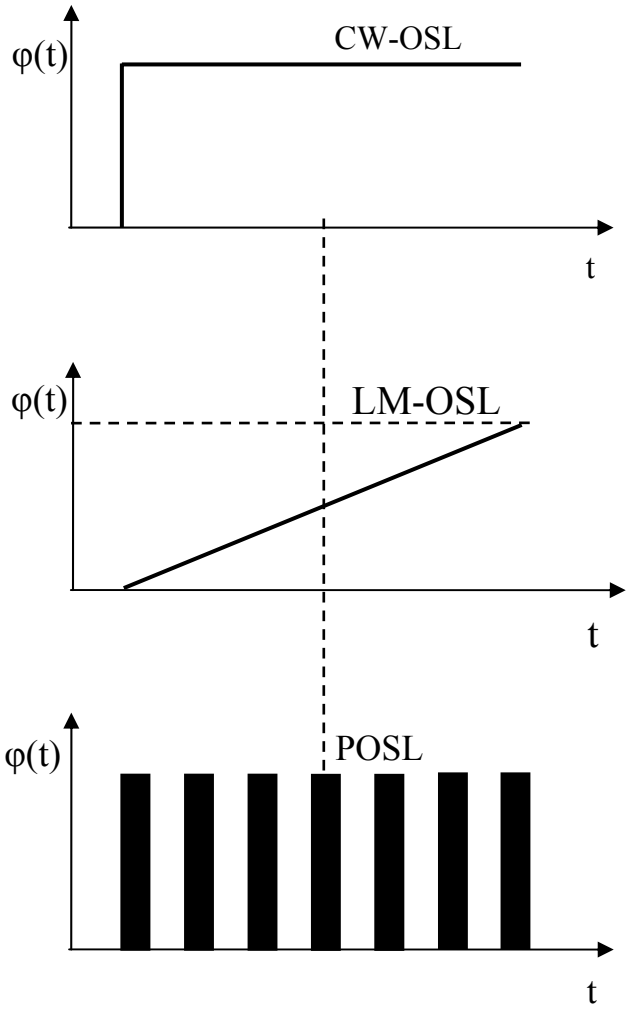

Figure 3.8. Schematics of different OSL stimulation methods (CW-OSL, LM-OSL and POSL)

In this work only the CW-OSL one-trap/one-recombination center model is going to be presented. Considering the initial conditions valid for the one-trap/one-recombination center model shown for TL (equations 3.4 and 3.5), the charge detrapping during the OSL production is described by the following set of rate equations (McKeever, 2001):

$$\frac{dn_c}{dt} = -\frac{dn_T}{dt} + \frac{dm_{RC}}{dt} \tag{3.16a}$$

$$\frac{dn_T}{dt} = -n_T p + n_c A_T \left(N - n_T\right) \tag{3.16b}$$

$$\frac{dm_{RC}}{dt} = -n_C A_{RC} m_{RC} \tag{3.16c}$$

In equations (3.16), p is the stimulation rate of the electron from the trap (expressed in units of s^{-1}) and depends on the incident photon flux φ and the photoionization cross-section σ (as already shown in equation 3.15); N is the concentration of the available electron traps (in units of m^{-3}); A_T is the probability that the electrons are trapped and A_{RC} is the recombination probability (both expressed in units of m^{-3} s^{-1}). In order to solve the CW-OSL rate equations for the OSL intensity $I_{CW-OSL}(t)$, the same approximations are considered as for the TL case (i.e., the 'quasi-equilibrium approximation' and 'slow re-trapping' approximation). Thus, the OSL intensity becomes:

$$I_{CW-OSL}(t) = -\frac{dm_{RC}}{dt} = -\frac{dn_T}{dt} = n_T p \tag{3.17}$$

Solving equation (3.17), for a constant stimulation light intensity:

$$I_{CW-OSL}(t) = n_0 p \exp(-tp) = I_0 \exp\left(-\frac{t}{\tau}\right) \tag{3.18}$$

Here, I_0 is the initial OSL intensity at $t_0 = 0$ and is proportional to the stimulation

intensity φ and the photoionization cross-section σ, and τ is the decay constant and is inversely proportional to the stimulation intensity and the photoionization cross-section. An example of OSL decay from Al_2O_3:C exposed to beta radiation from a $^{90}Sr/^{90}Y$ source and stimulated in green is presented in Figure 3.9. It can be seen that the shape of the OSL decay curve has an exponential–like form similar to the theoretical OSL intensity $I_{CW-OSL}(t)$ in equation (3.18).

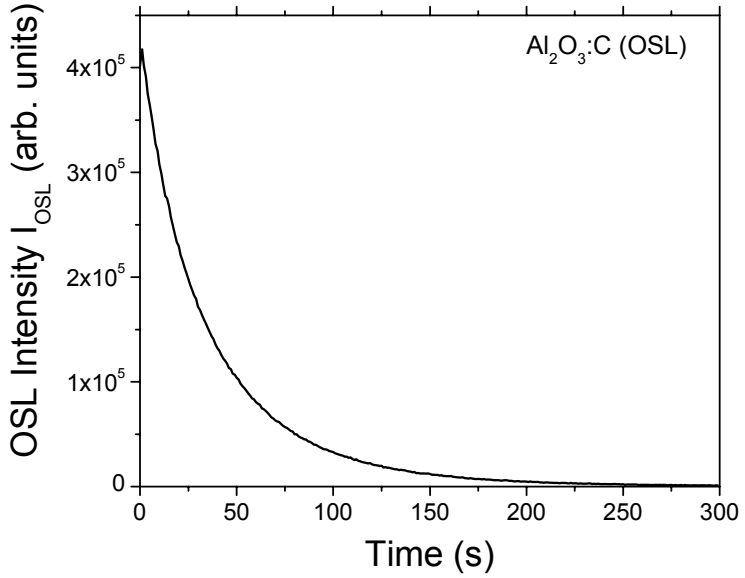

Figure 3.9. OSL decay curve of Al_2O_3:C exposed to a dose of 150 mGy using a $^{90}Sr/^{90}Y$ beta source, stimulated at $\lambda = 525\ nm$

The-light induced fading in Al_2O_3:C irradiated samples was investigated by Moscovitch et al. (1993) and Walker et al. (1996) and the results showed a drastic decrease in the TL signal of the main dosimetric peak. Consequently, it was suggested that the same traps responsible for the main TL peak in Al_2O_3:C are also responsible for the OSL production in this material. Thus, the optically released electrons from the main

trap radiatively recombine with F^+ centers giving rise to the 420 nm OSL emission.

However, the correspondence between the TL and OSL signals from Al_2O_3:C depends from sample to sample and is not always a straightforward relationship. For example, Akselrod & Akselrod (2002) investigated the light-induced fading of two different types of Al_2O_3:C samples (i.e., a narrow TL peak sample and a wide TL peak sample) using green light as stimulation. The results showed that the narrow peak had a strong decrease in sensitivity when exposed to green light, while the wide peak showed two components differently influenced by light. The low-temperature part of the peak was found to be very sensitive to light, while the high-temperature side of the TL peak was found to be light insensitive. Besides the sample type, the shape of the OSL decay curve from Al_2O_3:C depends on the concentration of both shallow traps (i.e., energy levels situated only slightly below the minimum energy of the conduction band – in the case of electrons) and deep traps (i.e., energy levels situated deeper below the conduction band), and the relative contribution of these competing traps to the OSL signal depends on the stimulation wavelength and temperature (Akselrod & Akselrod, 2002; Yukihara et al., 2004). The OSL sensitivity of Al_2O_3:C samples was found to be higher relative to their TL sensitivity, for doses lower than 0.5 μGy and heating rates of 1 – 2 °C/s (Bøtter-Jensen et al., 1997). The beta-induced OSL signal from Al_2O_3:C has a linear-supralinear-sublinear behavior with increasing dose, depending on the sample type (Yukihara et al., 2004). An interesting feature observed by Yukihara et al. (2004) is the change in the OSL decay curve at high doses. For low beta doses (up to 2 Gy), the shape of the OSL curves are similar, while for higher doses the OSL curves decay faster with increasing beta dose, as shown in figure 3.10 (adapted from Yukihara et al., 2004).

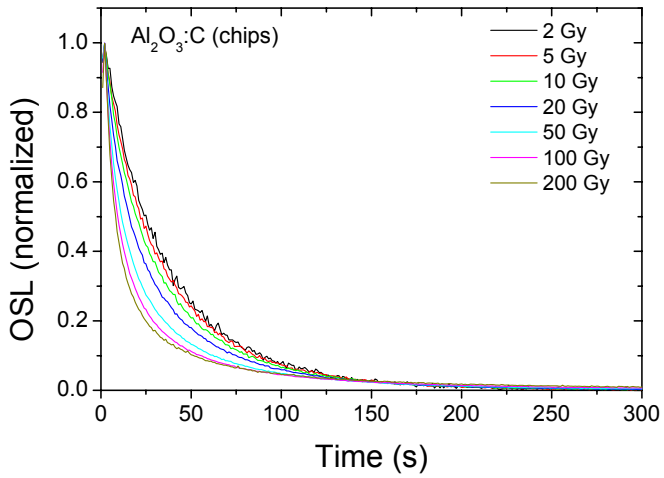

Figure 3.10. Different OSL decay curves from Al_2O_3:C (chips) as function of beta dose (adapted from Yukihara et al., 2004)

The curves were normalized to the initial OSL intensity in order to facilitate the direct comparison. The OSL beta dose response up to high doses, for both Al_2O_3:C-chips (5 mm diameter and 1 mm thickness) and Luxel^{TM} samples (Al_2O_3:C powder in polycarbonate film), was investigated by Yukihara et al. (2004) considering two definitions of the OSL signal: total OSL area (i.e., luminescence integrated over 300 s) and initial OSL intensity (luminescence averaged over the first 3 s). The obtained dose response curves corresponding to the two definitions of the OSL signal overlapped for small doses, but become totally different for high doses starting at about $2-3$ Gy, as shown in Figure 3.11. By comparing Figure 3.11a and Figure 3.10, it can be seen that the OSL dose response is different from the TL dose response for the same material (i.e., Al_2O_3:C-chips).

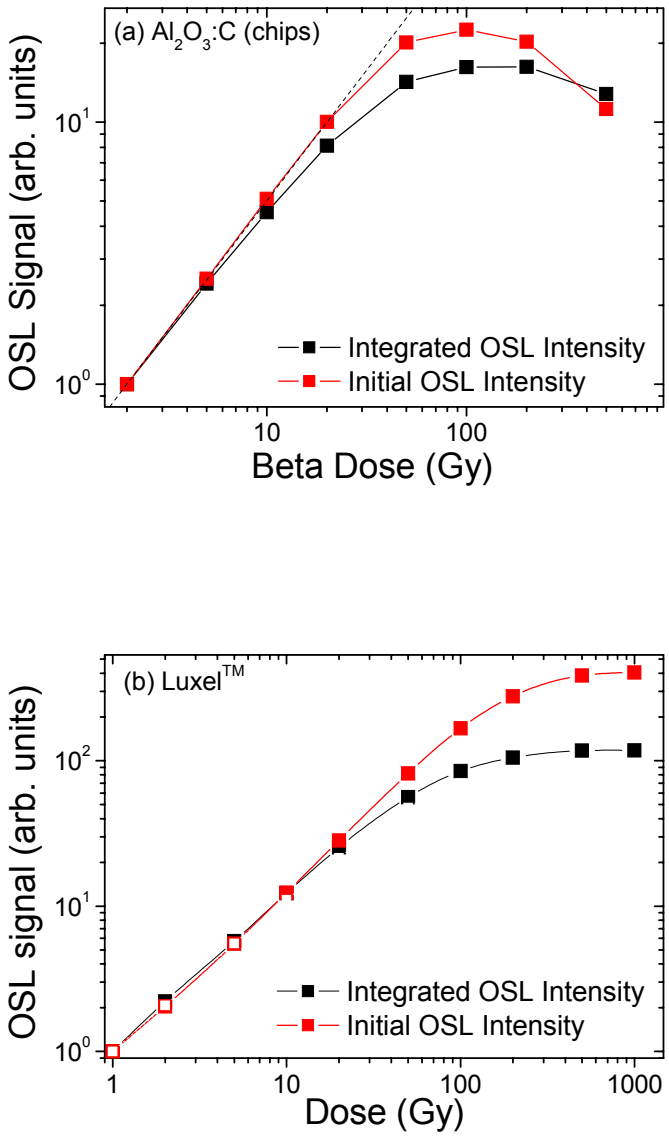

Figure 3.11. Comparison between the dose response of different OSL signals (i.e., total OSL area and initial OSL intensity) for Al_2O_3:C-chips (a) and Luxel™ (b) (adapted from Yukihara et al., 2004)

As a conclusion, the dose response of Al_2O_3:C to high beta doses depends on the sample type, the readout method (TL or OSL) and the definition of the OSL signal (i.e., total OSL area and initial OSL intensity). These properties of the OSL signal may have

implications regarding the OSL efficiency of Al_2O_3:C to heavy charged particles (HCP), since the luminescence response to HCP is dictated by the radial dose distribution along the particle's track and may result in high-dose regions close to the track. These features are to be discussed in the following chapters.

CHAPTER 4

HEAVY CHARGED PARTICLES DOSIMETRY AND TRACK STRUCTURE THEORY MODELS

4.1. The interaction of heavy charged particles with matter

A supplemental level of complexity is added to the picture by the fact that different types of ionizing radiation deposit their energy in different ways within a material. The energy deposited in a material by low-LET ionizing radiation (i.e., X-rays and γ-rays) results in a nearly isotropic distribution of the imparted dose. In contrast, the energy imparted to a medium by heavy charged particles (HCP) induces high-ionization density regions in the proximity of the particle's track, resulting in a very inhomogeneous distribution of dose.

When X-rays and γ-rays photons pass through matter they may undergo interactions via three main processes: the Compton effect, the photoelectric effect, and pair production. During any of these processes the incident photon energy is transferred to the electrons surrounding the atom. Consequently, the electrons will impart the absorbed energy to matter during only a few Coulomb-force interactions along very tortuous paths, resulting in an almost uniform dose distribution within the material.

A charged particle (CP), however, loses its kinetic energy gradually during many interaction events during a so-called *continuous slowing-down approximation* (CSDA) process. Two main types of energy loss events by charged particles in matter are: primary energy deposition events (the energy is transferred from CP to the electrons in the crystal

in close vicinity to the CP track) and secondary energy deposition events (the electrons lose their energy via excitation and ionization events that take place further away from the track), as shown in Figure 4.1. There are several types of possible charged particle interactions with a medium (Attix, 1986):

i. The primary charged particles can interact mainly with the shell electrons of an atom. As a result, the atom can be excited or ionized. The energy transferred by the CP to the atomic electrons can also result in ejected electrons, called δ-rays that will lose their kinetic energy along different tracks from that of the primary charged particle. Other secondary particles that will deposit their energy away from the main track are X-rays and Auger electrons that are produced when the shell electrons are ejected from the atom.

ii. The charged particles may interact primarily with the nucleus. If the collision is elastic (for about $97\,\%$ of the events), the energy loss is minimal and the differential elastic scattering cross-section is proportional to the target's atomic number squared, Z^2. Therefore, thin foils of high-Z materials can be used to spread out a charged particle beam with minimal energy losses in the target. For about $2-3\,\%$ of the cases, the collision is inelastic and *bremsstrahlung* radiation is emitted. In this case, the incoming charged particles give almost all of their kinetic energy to the emitted photons. The differential-cross section for such an event is also proportional to Z^2 and inverse proportional to the CP mass, thus the bremsstrahlung production by CPs compared to that of electrons is insignificant.

iii. For heavy charged particles (high kinetic energy $\sim 100\,\mathrm{MeV}$) nuclear interactions with a target may occur, resulting in the creation of secondary particles. One type of

particles that can be created as a result of such interactions are negative pions. These particles are unstable and they decay to negative muons that decay to electrons. When the negative pion is absorbed by the nucleus, nuclear fragments such as neutrons and charged particles are created. The charged particles deposit their energy close to the negative pion's track, while the neutrons carry their energy away from the track. These secondary particles have high biological effectiveness and the subsequent dose deposition process is difficult to follow. For luminescence dosimetry purposes, the nuclear interactions of heavy charged particles are ignored.

The interaction of charged particles with a medium can be characterized by the rate of energy loss per unit path length, along the particle's track. For radiation protection purposes, the so-called *linear energy transfer* (LET) is used to represent the mean energy loss per unit particle track length in a medium. The LET is inverse proportional to the kinetic energy of the incident charged particle. Thus, the linear energy transfer increases as the energy is lost in a medium, reaching a maximum value at the maximum penetration depth (e.g., the end of the particle's track). The corresponding dose distribution as function of the penetration depth is called the *Bragg curve*. A Bragg curve starts with an almost constant low-dose plateau, followed by a rapid dose increase up to a maximum value, after which the dose decreases drastically. The highly localized dose maximum is called the *Bragg peak*. The Bragg curve depends on the type and energy of the incident CP as well as the characteristics of the medium. The dose deposition profile (Bragg curve) of charged particles is highly desirable for radiotherapy applications and is used to better localize the radiation dose delivered to the tumor at a specific depth in tissue. Contrary to CP, electrons do not give rise to a Bragg peak near the end of their track

resulting in a broad peak distribution of dose situated at about half of their penetration depth (Attix, 1986).

4.2. Theoretical models regarding the energy deposited by HCPs in a material

The luminescence response of a material to any type of radiation (i.e., gamma-rays, HCP) is dictated by two main processes: the radiation energy deposition within the material and the release of the trapped charged carriers following stimulation, leading to the luminescence production. As mentioned before, following a HCP irradiation event, the energy is deposited within a material along highly localized trajectories resulting in a very inhomogeneous distribution of the absorbed dose. The energy deposition pattern for HCP in a detector is illustrated in Figure 4.1. It can be seen from Figure 4.1 that the spatial distribution of the primary energy deposition events dictates the parameters of the incident ion's physical track.

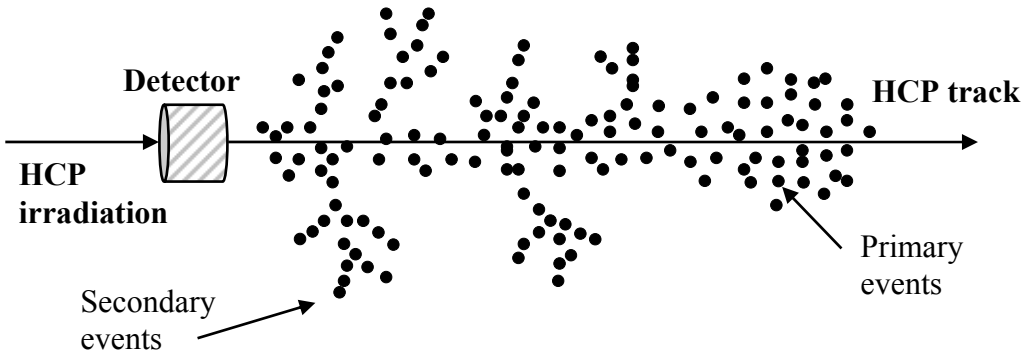

Figure 4.1. An illustration of the HCP energy deposition in matter via primary and secondary events

4.2.1. The track structure theory (TST) model

The first *track structure theory* (TST) approach was initiated by Butts and Katz (1967) when investigating the response of biological systems (i.e., dry enzymes and viruses) to heavy ions. The main hypothesis for the track structure theory states that the luminescence response of a material to HCP irradiation depends on the radial dose distribution along the ion's track (Butts and Katz, 1967). As a result, information about the HCP response of a specific material can be inferred from the dose response of the material to any type/energy of weakly ionizing radiation (i.e., γ-radiation, electrons). This conclusion was drawn considering that the biological end-effects for both HCP and weakly ionizing radiation depend entirely on the secondary electrons (Butts and Katz, 1967). Thus, in order to quantify the thermoluminescence response of a material to HCP the *relative efficiency*, $\eta_{HCP,ref}$ (i.e., the sensitivity to HCP compared to that of a reference radiation) was introduced:

$$\eta_{HCP,ref} = \frac{TL_{HCP}\left(D_{ref}\right)}{TL_{ref}\left(D_{ref}\right)} \tag{4.1}$$

In equation (4.1) the $TL_{HCP}\left(D_{ref}\right)$ represents the TL signal following a HCP irradiation calculated for a reference dose, using parameters experimentally determined from the dose response of the reference radiation. The reference radiation usually used is γ-radiation from a ^{60}Co source.

4.2.2. The modified track structure theory (MTST) model

An improvement to the track structure theory was added by Kalef-Ezra and Horowitz (1982) in considering the importance of matching the energy spectra and the irradiated

volume of the secondary electrons generated by the HCP and gamma reference radiations. The new theory, called the *modified track structure theory* (MTST) introduces a 'dose response function' obtained from a reference radiation that simulates as much as possible the energy spectra and the irradiated volume of the secondary particles produced by the investigated HCP radiation. For example, it has been experimentally proven that $4.7\,\text{keV}$ X-rays are more suitable to be used as the reference test radiation for LiF:Mg,Ti exposed to $4\,\text{MeV}$ alpha particles, when compared to high-energy gamma-rays (Kalef-Ezra and Horowitz, 1982). The MTST relative HCP efficiency to gamma, $\eta_{HCP,\gamma}$ is obtained as follows (Kalef-Ezra and Horowitz, 1982):

$$\eta_{HCP,\gamma} = \eta_{\delta,\gamma} \times \frac{\overline{W}_{\gamma}}{\overline{W}_{HCP}} \times \frac{\int_0^{R_{\max}} \int_0^{r_{\max}} f_{\delta}(D)\, D(r,l,E)\, 2\pi r \times dr \times dl}{\int_0^{R_{\max}} \int_0^{r_{\max}} D(r,l,E)\, 2\pi r \times dr \times dl} \tag{4.2}$$

where $\eta_{\delta,\gamma}$ is the relative TL response of the HCP secondary electrons to the reference radiation, $\overline{W_{HCP}}$ and $\overline{W_{\gamma}}$ are the mean energies necessary to create an electron-hole pair by the HCP and gamma radiation, respectively, $f_{\delta}(D)$ is the measured TL dose response function of the reference radiation (defined in the subsection 3.2.3), $D(r,l,E)$ is the radial dose distribution along the HCP's path, and $R_{\max}$ and $r_{\max}$ are the maximum axial and radial penetration distances reached by the charged carriers. Thus, both the dose response function $f(D)$ and the radial dose distribution $D(r,l,E)$ play an important role in estimating the MTST relative HCP-to-gamma efficiency for a given material.

The modified track structure theory was applied to predict relative TL efficiencies for LiF using either experimentally measured radial dose distributions in tissue equivalent

gases (Kalef-Ezra and Horowitz, 1982) or Monte Carlo (MC) simulated radial dose distributions (Avila et al., 1999). Avila and colleagues (1999) combined ion transport models that consider the energy loss in CSDA fashion and electron transport models in order to simulate the interactions of the secondary electrons, via elastic and inelastic collisions. Elastic collisions are considered to be accompanied by electron trajectory changes with no energy loss, while plastic collisions are responsible for both energy losses and changes in the electron trajectories. The Monte Carlo procedure considers that the energy lost is deposited in concentric cylindrical shells around the HCP path. The energy density is obtained by the ratio of the shell's energy to its corresponding volume. Radial dose distributions for LiF:Mg,Ti exposed to 1.43 MeV protons are shown in Figure 4.2 (Avila et al., 1999). Here, the total distance along z-axis (e.g., track length) was divided in eight different slices and the radial dose distributions were calculated for each slice.

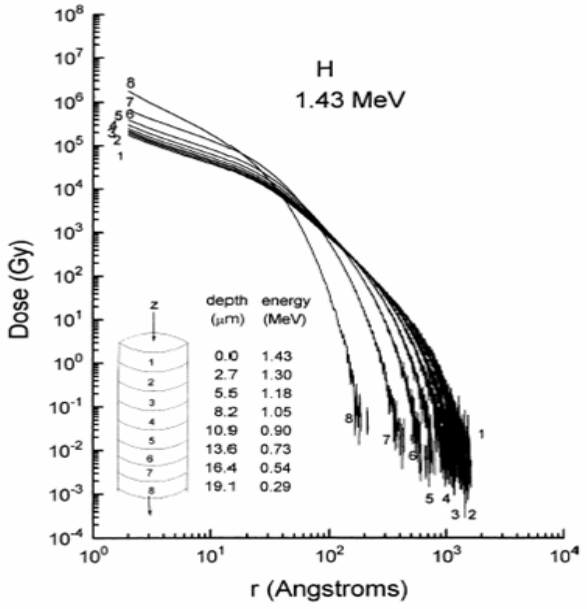

Figure 4.2. The radial dose distributions for LiF:Mg,Ti exposed to 1.43 MeV protons (Avila et al., 1999)

Avila and colleagues (1999) calculated the proton-to-gamma and helium-to-gamma TL efficiencies for LiF by considering both the radial dose distributions obtained from Monte Carlo calculations and the dose response function obtained using an X-rays reference test radiation of 8.1 keV. The MTST calculated efficiencies for protons and helium ions (equation (4.2)) were than compared to the experimentally determined efficiency values (equation (4.3)), and the results were found to be in good agreement (Avila et al., 1999):

$$\eta = \frac{\left(TL/D_0\right)_{HCP}}{\left(TL/D_0\right)_{\gamma}} \tag{4.3}$$

where TL is the TL response per unit irradiated mass at a low-dose D_0 where the response is linear for both HCP and gamma radiation, respectively.

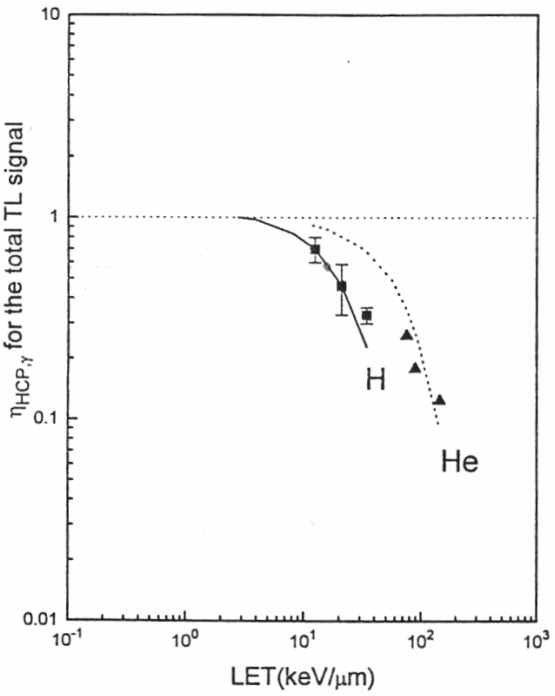

Figure 4.3. The calculated MTST efficiency values (solid/dashed lines) for LiF exposed to 0.7, 1.4 and 2.6 MeV protons and 2.6, 4.9 and 6.8 MeV helium ions compared to the experimentally determined efficiency values (squares/triangles) as function of LET (Avila et al., 1999)

Geiβ and colleagues (1998) applied radial dose distributions models to LiF crystals (TLD-700) and compared the results of the track structure calculations to the experimental data obtained for a wide range of ions and energies, as shown in Figure 4.4. The experimental results were found to be in good agreement with the modeling data, aside from low-energy ions with energies of a few MeV and some heavy ions. These differences are believed to be related to definition of the radial dose distribution ($D(r) \sim 1/r^2$) and the particularities of the Monte Carlo code used (Geiβ et al., 1998).

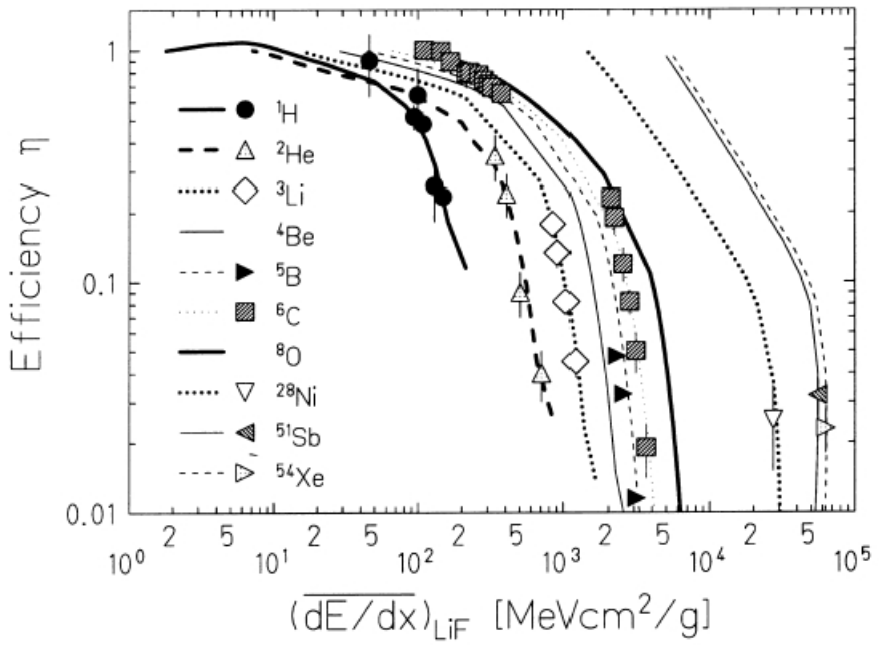

Figure 4.4. The dependence of the efficiency of TLD-700 on the mean energy loss. Comparison between the experimental (symbols) and calculated (lines) results (Geiβ et al., 1998).

4.2.3. Supralinearity in the TL fluence response of LiF:Mg,Ti to HCP

The TL fluence response of LiF to heavy charged particles has been studied in great detail over the years (e.g., Gamboa-deBuen et al., 1998; Aviles et al., 1999). The authors observed that the TL response of LiF to both HCP and γ-rays has a linear-supralinear-

saturation behavior with increasing fluence/dose. The HCP induced TL signal as function of fluence is described by the *fluence response function*, $f(n)$ as follows:

$$f(n) = \frac{F(n)/n}{F(n_{ref})/n_{ref}} \tag{4.4}$$

In Eq. 4.4, $F(n)$ is the TL signal intensity at fluence n and $F(n_{ref})$ is the TL signal intensity at reference fluence n_{ref} in the linear region of the fluence response. Thus, $f(n) = 1$ defines the linear region, while $f(n) > 1$ corresponds to the supralinear region. The degree of supralinearity of the TL fluence response of LiF has been experimentally observed to depend on several factors such as the type and energy of the incident radiation, the material itself (i.e., defects concentration), the definition of the TL signal (i.e., different peaks have different dose or fluence response functions), the experimental parameters (i.e., annealing/cooling treatment, readout procedure, etc.) (Gamboa-deBuen et al., 1998; Gamboa-deBuen et al., 2001). Also, the fluence at which the supralinearity starts has been found to depend on the type/energy of the incident radiation as well as the vector properties of the radiation field (Horowitz, 1996).

4.2.4. The track interaction model (TIM) for HCP-induced supralinearity in LiF

One approach to explain the supralinearity of the TL fluence response of LiF:Mg,Ti exposed to HCP is the track interaction model (TIM) (Horowitz et al., 1996; Horowitz et al., 2001). This model considers three types of defect to be responsible for the linear-supralinear-saturation behavior of the TL signal, namely trap centers (TC), luminescent centers (LC) and competitive centers (non-radiative centers) (CC). For the following discussion, it is assumed that the trap centers are electron centers and the luminescent

centers are hole centers. The TL response of a material exposed to a specific type of radiation is believed to be influenced by both the irradiation stage and the recombination stage.

According to TIM, following HCP irradiation the charge carriers (i.e., electrons) are trapped inside the track where the luminescent centers are activated, while the competing centers are completely deactivated. Nevertheless, the region outside the track is considered to be filled with activated CC. Here, luminescent centers are considered to be 'activated' when they are completely filled with electrons, while competitive centers are considered to be 'activated' when they are completely empty. In the recombination (heating) stage, at low fluences, the recombination occurs entirely inside the HCP track, while the escaped electrons become trapped at CC and do not contribute to the TL signal. Therefore, the TL signal is proportional to the number of HCP tracks (i.e., fluence) resulting in a linear fluence response. As the fluence increases, the distance between neighboring tracks decreases, thus increasing the probability that the escaped electrons will recombine inside the closest neighbor track, resulting in an increased TL efficiency. Thus, the supralinearity of the TL response occurs. For even higher fluences, the traps and/or recombination centers become full and the saturation of the TL signal occurs

.

4.2.5. The unified track interaction model (UNIM)

Similar to the track interaction model for HCPs, the so-called *unified track interaction model* (UNIM) was introduced in order to describe the gamma-induced supralinearity observed in LiF (Horowitz et al., 1996; Horowitz, 2001). As for HCP, the gamma-induced TL signal has a linear-supralinear-saturation response with increasing

dose. The linearity of the gamma-induced TL dose response is believed to be related to the existence of localized doubly occupied spatially correlated trap center/luminescent center pairs in LiF, concept introduced by Mische & McKeever (1989). In other words, the defect distribution in the material is such that localized TC/LC pairs are present, with the TC being occupied by an electron and the LC being occupied by a hole. These highly localized TC/LC pairs are believed to be free of active CC. Thus, for low gamma doses, there is a high probability for a released electron from the TC/LC pair to recombine with a hole from the same TC/LC pair, leading to the so-called *geminate recombination* inside the localized TC/LC pairs (Horowitz, 2001). At higher doses, the distance between neighboring TC/LC pairs decreases resulting in an increase in the TL efficiency and a supralinear dependence of the TL with dose. When the TC/LC are completely filled the TL signal is saturated. UNIM was successfully applied by Rodríguez-Villafuerte and colleagues (2000) to investigate the fluence response of LiF:Mg,Ti exposed to different energies of helium ions (i.e., 3 MeV and 7.5 MeV). The experimentally determined supralinearity functions (i.e., the fluence response function) for different TL peaks (5, 8 and 9) were compared with Monte Carlo simulations of the track interaction model. The experimental data were found to be in good agreement with the theoretical data, as shown in Figure 4.5 (Rodríguez-Villafuerte et al., 2000).

The track interaction model has been further developed to investigate in much more detail the supralinearity and saturation effects in the TL response of LiF, into the so-called *extended track interaction model* (ETIM). The ETIM model (not to be discussed in detail here) investigates the track structure using information from several sources, such as the defect occupation probabilities as function of the radial distance, optical absorption

measurements, and sensitization measurements (Horowitz et al., 2001).

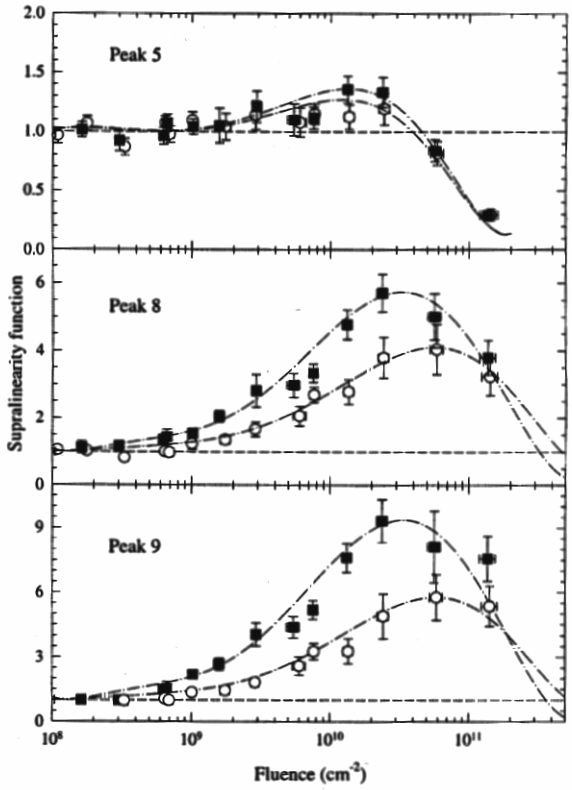

Figure 4.5. Simulated supralinearity data (dashed curve) and experimental data for LiF:Mg,Ti exposed to 3 MeV (open symbols) and 7.5 MeV (solid symbols) helium ions (Rodríguez-Villafuerte et al., 2000)

In this chapter, the TL response of LiF:Mg,Ti to heavy charged particles was explained by several authors in terms of different track interaction models. In the next chapter, experimental results regarding the OSL response of Al_2O_3:C to low-energy particles will be presented together with a simple model for the energy deposition processes by HCP in the Al_2O_3:C dosimeters.

CHAPTER 5

THE TL AND OSL RESPONSE OF Al_2O_3:C TO LOW-ENERGY HEAVY CHARGED PARTICLES: MODELS AND EXPERIMENTAL RESULTS

5.1. Purpose of the project

The current chapter investigates the luminescence response of Al_2O_3:C to low-energy heavy charged particles obtained from a Pelletron accelerator at the Instituto de Fisica, UNAM, Mexico City. The Pelletron accelerator from UNAM can deliver several species of ions such as protons, helium, carbon, and oxygen having energies on the order of units of MeV.

Ideally, a luminescent dosimeter would return an OSL/TL signal which is proportional to the energy deposited in its volume by ionizing radiation, with the factor of proportionality being constant with respect to the radiation quality. This is especially important for a dosimeter designed to measure a radiation field consisting of a wide assortment of particles, of different types (Z number) and energies, as in the case of space radiation. However, the luminescence signals from real dosimeters often exhibit dependences on various parameters of the incident radiation particles, including (but not limited to) energy, charge and size (i.e. the A and Z numbers of the projectile), and intensity of the beam (i.e. particle fluence). To quantify the sensitivity of the OSL/TL response for HCP irradiations relative to that for irradiations performed using standard radioactive sources (i.e, ^{60}Co source), a physical quantity denoted as the efficiency η has been introduced. In the literature, the luminescence efficiency is defined as:

$$\eta = \frac{I_{HCP} / (D_{HCP} \cdot m_{HCP})}{I_{\gamma} / (D_{\gamma} \cdot m_{\gamma})} \tag{5.1}$$

Here, I_{HCP} is the OSL/TL signal measured from the dosimeter following an HCP irradiation that deposited a dose D_{HCP} in its volume, I_{γ} is the OSL/TL signal measured from the dosimeter following absorption of a gamma dose D_{γ}. The masses m_{HCP} and m_{γ} correspond to the fractions of the dosimeter where the doses D_{HCP} and D_{γ}, respectively, were deposited. Usually, the efficiency defined by the equation (5.1) considers that both D_{HCP} and D_{γ} are in the linear range of the OSL/TL dose response. Relation (5.1) can be simply interpreted as the relative sensitivity of the dosimeter to HCP (S_{HCP}), as compared to the sensitivity for standard gamma irradiations (S_{γ}), as follows:

$$\eta = \frac{S_{HCP}}{S_{\gamma}} \tag{5.2}$$

Both the HCP sensitivity S_{HCP} and the gamma sensitivity S_{γ} can be expressed in terms of either the dose D_{HCP} or the total energy E_{HCP} absorbed in the dosimeter. Relation (5.3) applies for both S_{HCP} and S_{γ}.

$$S_X = \frac{I_X}{D_X \cdot m_X} = \frac{I_X}{E_X} \tag{5.3}$$

Here, the subscript X can be substituted for either HCP or γ. Choosing a particular form to express the sensitivity S_X is dictated by the particular experimental considerations. However, both formulations are completely equivalent.

Light particles such as photons and electrons emitted by standard radioactive sources (i.e., ^{60}Co and ^{90}Sr/^{90}Y) have ranges comparable to (or larger than) standard luminescence

samples. Therefore, it is convenient to use these sources in order to calibrate the sensitivity of the sample in terms of the characteristic doses absorbed in the dosimeters:

$$S_\gamma = \frac{I_\gamma}{D_\gamma \cdot m_\gamma} \tag{5.4}$$

In contrast, heavy charged particles with kinetic energies in the range investigated here have penetration depths on the order of few tens to one hundred microns. Therefore, all the incident charged particles will deposit their entire energy, and will come to a complete stop in the volume of the dosimeter (usually of thickness on the order of 1mm). The situation is schematically depicted in Figure 5.1. Irradiation with highly penetrating radiation (e.g., gamma) case is also showed for comparison.

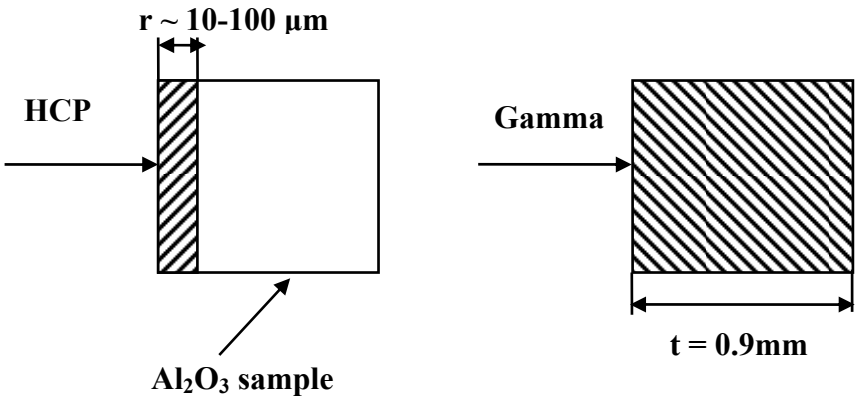

Figure 5.1. Schematics of the energy deposition by low-energy HCP and gamma radiation in Al_2O_3, where t is the sample thickness and r is the HCP penetration range

The total energy deposited by the heavy charged particles in the dosimeter can be most conveniently obtained from the known kinetic energy E_0 of the particles and the total number N of particles incident on the dosimeter surface:

$$E_{HCP} = E_0 N = E_0 \Phi A_{irr} \tag{5.5}$$

Here, the particle fluence Φ (expressed in cm^{-2}) and the incident energy E_0 can be calculated using the experimental parameters recorded during the operation of the accelerator (details on these calculations will be given in section 5.2), and A_{irr} represents the irradiated area of the dosimeter (in units of cm^2). Using equation (5.3) for HCPs and equation (5.5) the sensitivity S_{HCP} becomes:

$$S_{HCP} = \frac{I_{HCP}}{E_{HCP}} = \frac{I_{HCP}}{E_0 N} \tag{5.6}$$

The equations (5.2), (5.3) and (5.4) can be then combined to obtain the following expression for the efficiency η:

$$\eta = \frac{I_{HCP}/E_0 N}{I_\gamma / D_\gamma m_\gamma} \tag{5.7}$$

In order to correct the measured OSL/TL signal I_{HCP} by the sensitivity S_γ, a so-called corrected luminescence signal $I_{HCP,corr}$ is introduced:

$$I_{HCP,corr} = \frac{I_{HCP}}{S_\gamma} \tag{5.8}$$

The efficiency in equation (5.7) can be rewritten in terms of the new variable as:

$$\eta = \frac{I_{HCP,corr}}{E_0 N} \tag{5.9}$$

In terms of the energy per nucleon E_0/A, equation (5.7) can be written as:

$$\eta = \frac{1}{E_0/A} \frac{I_{HCP,corr}}{AN} \tag{5.10}$$

where A the mass number of the incident particle. Equation (5.9) and (5.10) suggest that the efficiency can be interpreted as the slope of the dependence of the corrected

luminescence signal $I_{HCP,corr}$ on any of the parameters E_0, E_0/A, A or N, in case the other parameters are held constant (subject to experimental particularities).

In the following sections, the experimental details of the UNAM irradiations are presented in detail (section 5.2). Also, a simple model for the energy deposition processes by HCP in the Al_2O_3:C dosimeters is proposed. This model will then be used to predict the behavior of the efficiency vis-à-vis the parameters mentioned, and confirm the predictions by comparing them with experimental data (section 5.3). Additional efficiency features for the HCP-induced OSL signal from Al_2O_3:C dosimeters are presented in section 5.4.

5.2. Experimental details of the UNAM irradiations

The OSL/TL responses of different types of luminescence dosimeters were investigated for different low-energy ions (i.e., protons, helium, carbon and oxygen) using a 3 MV Pelletron Tandem accelerator at UNAM. Two different types of Al_2O_3:C samples were used: single Al_2O_3:C crystals (chips) of 5 mm in diameter and 0.9 mm thickness, obtained from Nextep Technologies, and Luxel™ sheets (Al_2O_3:C powder in polycarbonate film) of dimensions of $120\times17\times0.35$ mm obtained from Landauer Inc. In addition, LiF:Mg,Ti dosimeters known as Harshaw/Bicron TLD-100 chips ($3.2\times3.2\times0.9$ mm) were used. The OSL/TL dosimeters were analyzed via the following procedure:

i. Pre-irradiation annealing of the samples (see details in section 5.2.1)
ii. HCP irradiations at UNAM (see details in section 5.2.2)
iii. Readout of the signal induced $(I_{OSL/TL})_{HCP}$ by the HCP irradiations at UNAM (see

details in section 5.2.3)

iv. Post-readout annealing of the samples

v. Irradiation with a known reference beta dose D_R (calibrated with respect to a to a ^{60}Co gamma source at NIST)

vi. Readout of the reference signal I_R.

The reported quantity is the corrected OSL/TL signal $I_{HCP,corr}$ given by equation (5.8).

5.2.1. Preparation of the samples

Prior to irradiations, the OSL/TL samples were subjected to different annealing/bleaching procedures in order reset the luminescence signals to the background level and to re-establish the thermodynamic equilibrium conditions. The Al_2O_3:C chips were annealed at 900 ºC for 15 minutes as recommended by McKeever at al. (1995), then cooled in air by contact with a metal plate at room temperature. The Al_2O_3:C samples were also polished and a surface layer of about 150 μm was removed from each sample in order to reduce the possible surface effects on the luminescence efficiency (to be discussed in more detail in section 5.4). The Luxel samples were bleached for 12 h at room temperature, using a halogen lamp filtered by a Kopp 3-69 filter (yellow light). The Luxel dosimeters were further prepared by removing the plastic film in front of the Al_2O_3 layer in order not to create an obstacle for the incident HCPs. The TLD-100 chips were annealed at 400 ºC for 1 h, followed by a 2 h annealing at 100 ºC, a standard annealing procedure used to re-establish the defect equilibrium and to enhance the luminescence of the main dosimetric peak (~220 ºC), concomitantly reducing the influence of the low temperature peaks (McKeever et al., 1995). After annealing, the TLD-100 samples were

cooled at room temperature. In addition to the HCP radiation, the samples were also subjected to the background radiation during the Oklahoma City – Houston – Mexico City – and return flights. The OSL/TL signal due to the background radiation was taken into account and subtracted from the total luminescence signal.

5.2.2. Radiation exposures

The OSL/TL dosimeters were exposed to low-energy heavy charged particles over a wide range of fluences (i.e, from 10^7 up to 9×10^9 part/cm^2) and nominal energies of 1.0, 2.0 and 4.0 MeV (protons), 2.5, 5.0 and 8.9 MeV (helium), 13 MeV (carbon), and 10 MeV oxygen. Prior to irradiation, the samples were placed in a semi-circular aluminum sample holder specifically designed to fit the geometry requirements of the irradiation setup, at known angles with respect to the direction of the beam. A picture of one of the used sample holders is shown in Figure 5.2.

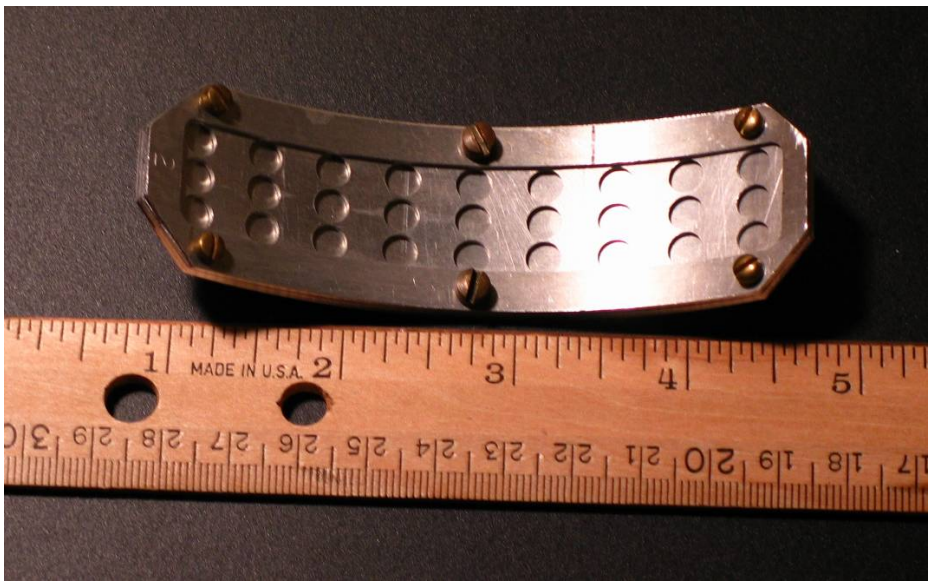

Figure 5.2. Example of sample holder specifically designed for the UNAM projects

Depending on the experiment, for each ion/energy, the distribution of the samples inside the holder was different. The details regarding the sample positions inside the holder, for each ion/energy and material/readout method, are given in Appendix A. The Pelletron irradiation experimental setup is based on elastic Rutherford scattering of the incident ion beam by a thin gold target (of the order of 10^{-4} g/cm^3 thickness), as schematically shown in Figure 5.3. For the carbon ions the incident beam was perpendicular to the gold target, while for the proton and helium irradiations the target was positioned at a $20°$ angle with respect to the direction of the beam. A silicon surface barrier detector, placed at $135°$ angle with respect to the direction of the incident beam, was used to count the elastically scattered particles. Knowing the number of the scattered particles and the geometry of the beam, the HCP fluence can be calculated for each particular experimental setup, as described in section 5.2.4. A more detailed description of the Pelletron accelerator setup can be found elsewhere (Rodríguez-Villafuerte et al., 2000; Gamboa-deBuen et al., 2001).

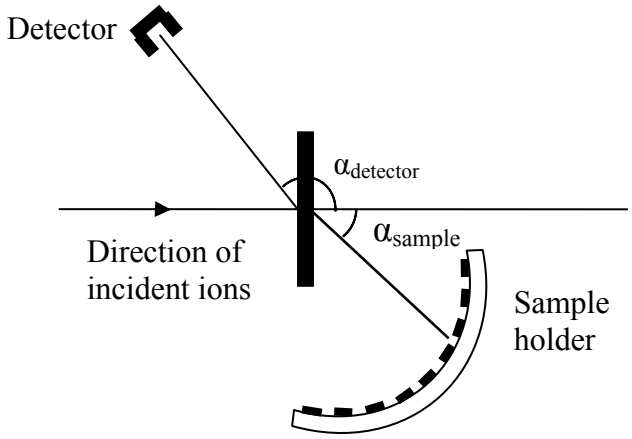

Figure 5.3. Schematics of the irradiation setup for the UNAM experiments

5.2.3. Readout procedures

The samples were analyzed using an automatic Risø TL/OSL-DA-15 reader with an incorporated $^{90}Sr/^{90}Y$ beta radiation source (Bøtter-Jensen et al., 2000), as shown in Figure 5.4. Since the Al_2O_3:C samples are light sensitive, extra precautions were taken so that the Al_2O_3:C samples will not be exposed to light between irradiation and readout. The Al_2O_3:C samples were analyzed using both TL and OSL methods, the Luxel samples were measured in OSL mode and the TLD-100 chips were readout in TL mode. The luminescence signal was recorded using an Electron Tubes 9235QB photomultiplier tube through an appropriate choice of optical filters and apertures.

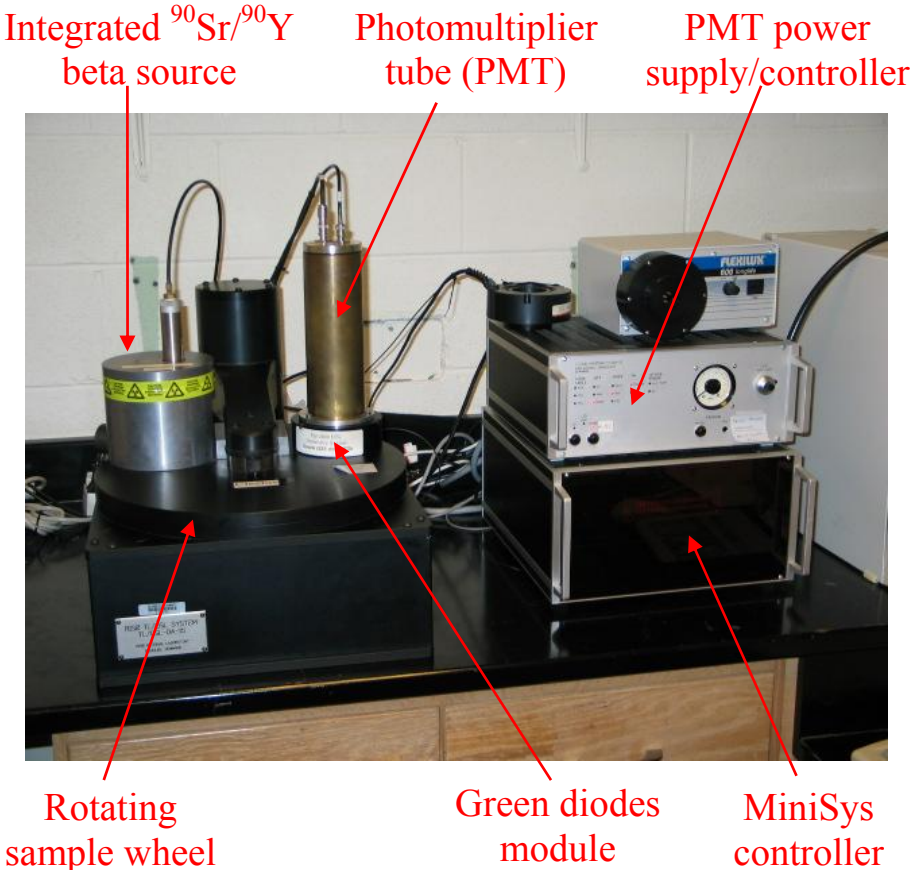

Figure 5.4. Picture of the Risø TL/OSL-DA-15 reader featuring an integrated beta source

The TL signal from Al_2O_3:C was recorded while linearly ramping the temperature at a heating rate of 1ºC/s starting at room temperature up to 350ºC to ensure the full readout of the main dosimetric peak centered at about 185ºC. The experiments were carried out using an 415 nm narrow band optical filter (with transmission band full width at half maximum of ~ 20 nm) and an appropriate aperture in order to maximize the TL signal. The TL signal of the TLD-100 dosimeters was measured at a heating rate of 1ºC/s starting at room temperature up to 380ºC in order to record the luminescence signal coming from the main dosimetric peak as well as the high temperature peaks. The experiments were carried out without any optical filtration or aperture in order to maximize the TL signal. An example of Al_2O_3:C and LiF:Mg,Ti TL glow-curves exposed to 1.0 MeV protons is given in Figure 5.5. The curves were normalized with respect to the peak height of the main peak to allow a direct comparison between the two materials.

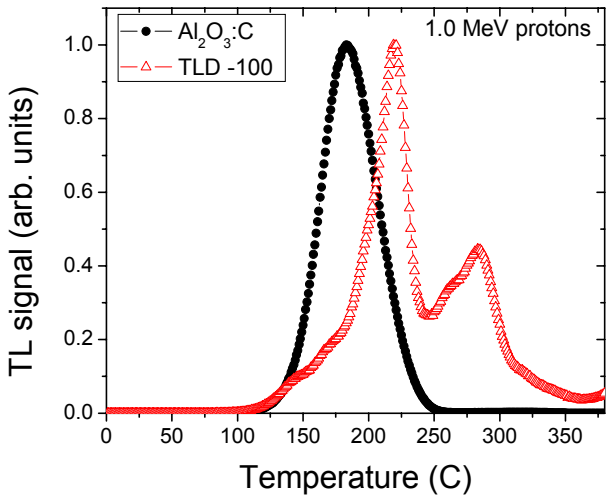

Figure 5.5. TL glow curves for Al_2O_3:C and LiF:Mg,Ti (TLD-100) exposed to 1.0 MeV protons and fluences of 5.8×10^9 part/cm^2 and 4.1×10^9 part/cm^2

The TL signals from the Al_2O_3:C and LiF:Mg,Ti samples were defined as the peak height

of the corresponding main dosimetric peaks, centered at about 180 ºC and 225 ºC, respectively.

The OSL signal from the Al_2O_3:C and Luxel dosimeters was recorded while illuminating the samples with green LEDs (at 525 nm). The luminescence measured by the photomultiplier tube was detected through Hoya U-340 filters (with transmission band centered at 340 nm and transmission band full width at half maximum of about 80 nm) of 7.5 mm total thickness for optimum discrimination between stimulation and emission light. Depending on the material, an appropriate aperture was also used to reduce the luminescence signal coming from the sample. An example of OSL signal from Al_2O_3:C exposed to 1.0 MeV protons and a fluence of 1.5×10^9 part/cm^2 is shown in Figure 5.6. It can be noticed that the OSL curve decayed back to the background level after 5 minutes of light stimulation. The OSL signal from the Al_2O_3:C samples is defined as the OSL signal recorded after the first second of light stimulation (i.e., initial OSL intensity).

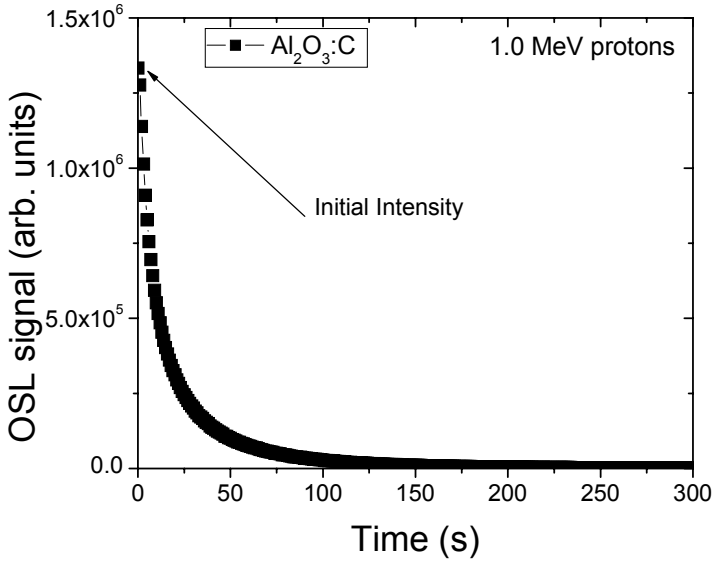

Figure 5.6. CW-OSL decay curve for Al_2O_3:C chips exposed to 1.0 MeV protons

Considering the differences in the optical filtration used for the Al_2O_3:C TL and OSL readout procedures, differences in the corresponding luminescence efficiencies are expected. While the TL signal from Al_2O_3:C is given mostly by the $F-$center emission (the signal is measured trough a 415 nm narrow band optical filter), the OSL signal from the same material is measured through wide band U-340 filters, and may contain a luminescence component due to the F^+-center emission, in addition to the main $F-$center emission. As a result, the TL signal and the OSL signal from Al_2O_3:C may give rise to different luminescence efficiencies due to the difference in the corresponding optical filtrations.

5.3. Data analysis – energy and fluence calculations

Several parameters of interest, such as the energy E_0 at the sample and fluence Φ at a specific position in the sample holder, need to be known when investigating the OSL/TL response of the dosimeters.

5.3.1. Energy calculations

The actual energy incident on the sample E_{sample} is different from the nominal energy E_0 due to the experiment particularities (i.e., the energy loss in the gold target). The corrected energy values were calculated for the two cases of 0° and 20° inclination of the gold target. Considering that the incident particles may follow any path when traveling through the target, two different 'extreme' paths were considered when calculating the actual energies, as shown in Figure 5.7. Here, the incident beam is

assumed to be perpendicular on the target as in the case of carbon ions irradiations.

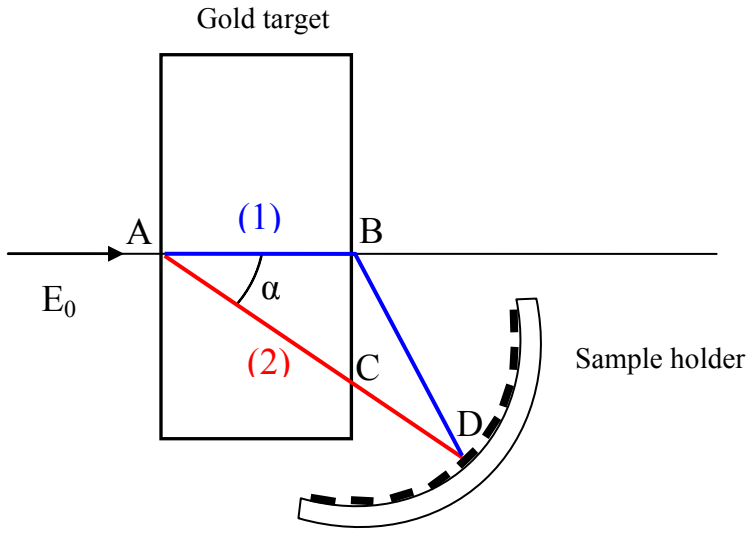

Figure 5.7. Possible paths to be followed by the incident particles when traveling through the target (the beam is perpendicular on the target)

The first path assumed that the direction of the incident particle does not change inside the target (path 1) and the second path (path 2) assumed that the incident particle travels through the target at an angle equal to the sample angle. Considering the geometry in Figure 5.9, the actual energy of the particles when reaching the sample can be calculated as follows:

i. Path 1 ($A \rightarrow B \rightarrow D$)

$$E_{A\rightarrow B} = E_0 - (\frac{dE}{dx})_{Au} \times t \tag{5.11a}$$

$$E_{B\rightarrow D} = E_{A\rightarrow B} \times k \tag{5.11b}$$

ii. Path 2 ($A \rightarrow C \rightarrow D$)

$$E_{A\rightarrow C} = E_0 \times k \tag{5.11c}$$

$$E_{C\rightarrow D} = E_{A\rightarrow C} - (\frac{dE}{dx})_{Au} \times \frac{t}{\cos\alpha} \tag{5.11d}$$

In equations (5.11), E_0 is the nominal energy of the incident particles, $(\frac{dE}{dx})_{Au}$ is the energy loss per unit length in the gold target, t is the target thickness, α is the sample angle and k is a factor that takes into account the energy loss in the target due to changes in the initial energy and momentum of the incident particle, called the *kinematics factor*:

$$k = \left[\frac{m\cos\alpha \pm \left(M^2 - m^2 \sin^2 \alpha\right)^{1/2}}{m + M} \right]^2 \tag{5.12}$$

Here, m is the mass of the particle and M is the target mass. The mathematical details for obtaining the kinematics factor k are presented in Appendix B. If the target is inclined at a specific angle with respect to the beam direction (as for the protons and helium irradiations) the equations (5.11) become:

i. Path 1 ($A \rightarrow B \rightarrow D$)

$$E_{A\rightarrow B} = E_0 - (\frac{dE}{dx})_{Au} \times \frac{t}{\cos\beta} \tag{5.13a}$$

$$E_{B\rightarrow D} = E_{A\rightarrow B} \times k \tag{5.13b}$$

ii. Path 2 ($A \rightarrow C \rightarrow D$)

$$E_{A\rightarrow C} = E_0 \times k \tag{5.13c}$$

$$E_{C\rightarrow D} = E_{A\rightarrow C} - (\frac{dE}{dx})_{Au} \times \frac{t}{\cos(\alpha - \beta)} \tag{5.13d}$$

Here, β is the angle between the target and the direction of the beam. The actual energy values depend on the sample position and were calculated using equations (5.11) or equations (5.13) as appropriate. An average energy value of the two energies corresponding to paths (1) and (2) was considered when calculating the HCP dose.

5.3.2. Fluence calculations

Assuming Rutherford elastic scattering, the scattering differential cross-section is (Eisberg and Resnick, 1985):

$$\frac{d\tau}{d\Omega} = \left(\frac{1}{4\pi\varepsilon_0}\right)^2 \times \left(\frac{zZe^2}{4E}\right)^2 \times \frac{1}{\sin^4\left(\frac{\alpha}{2}\right)} \tag{5.14}$$

where z and Z are the atomic numbers of the incident ion and target, respectively; E is the energy of the incident ion and α is the detection angle. Starting with the Rutherford scattering differential cross-section and considering the specifics of the experimental setup, the UNAM group calculated the fluence Φ (i.e., the number of particles incident on the sample N_S per unit area A_S) as follows[iii]:

$$\Phi = \frac{N_S}{A_S} = N \times \frac{\sin^4\left(\frac{\alpha_D}{2}\right) \times (d_D)^2}{\sin^4\left(\frac{\alpha_S}{2}\right) \times (d_S)^2 \times \pi\,(r_D)^2} \tag{5.15}$$

where N is the total number of particles counted by the detector, α_D and α_S are the angles between the direction of the incident beam and the detector and sample, respectively, d_D is the distance between the detector and the target, d_S is the sample-target, and r_D is the detector radius. All of the geometrical parameters used to calculate the fluence (equation 5.15) were measured prior to irradiation. From the geometry of the system it can be inferred that the fluence values corresponding to rows 1 and 3 of the sample holder are the same, while the fluence value corresponding to row 2 is slightly different. The percentage difference is less than 1 % within the limits of the experimental

[iii] Internal Document Instituto de Fisica, UNAM

error. The corrected energy values and the corresponding fluence range for the 1.0, 2.0 and 4.0 MeV (protons), 2.5, 5.0 and 8.9 MeV (helium ions), 13 MeV (carbon ions) and 10 MeV (oxygen ions) are given in Table 5.1.

Table 5.1. The corrected energy values and the corresponding fluence ranges for the protons, helium, carbon and oxygen irradiations at UNAM

Particle Type	Nominal Energy (MeV)	Corrected energy range (MeV)	Fluence range (part/cm^2)
Protons	1.0	0.91 ÷0.95	1.5×10^{7} ÷8.2×10^{9}
	2.0	1.92 ÷1.96	1.4×10^{7} ÷7.6×10^{9}
	4.0	3.92 ÷3.97	1.4×10^{7} ÷8.9×10^{9}
Helium	2.5	2.33 ÷2.39	1.5×10^{7} ÷5.9×10^{9}
	5.0	4.84 ÷4.92	1.5×10^{7} ÷6.3×10^{9}
	8.9	8.74 ÷8.84	1.5×10^{7} ÷5.8×10^{9}
Carbon	13	11.1 ÷11.6	1.4×10^{7} ÷8.8×10^{9}
Oxygen	10	7.59 ÷7.85	4.0×10^{7} ÷9.2×10^{9}

The corrected energy values and the fluence values were used to calculate the absorbed HCP dose, as follows:

$$D_{HCP} = \frac{1.6\times10^{-10}\times\Phi\times E_S}{R_{HCP}\times\rho_S} \tag{5.16}$$

In equation (5.16), E_S is the actual energy that reaches sample (in units of MeV), R_{HCP} is the range of the heavy charged particle in the sample (in units of cm), and ρ_S is the

density of the sample (in units of g/cm^3). The numerical factor 1.6×10^{-10} is a 'correction for units' factor so that the dose is expressed in units of Gray (Gy). The HCP doses are needed to obtain the efficiency given by equation (5.1).

5.4. The influence of the HCP characteristics on the OSL/TL efficiency – models and experimental results

In this section, the effects of different parameters on the luminescence efficiency are investigated. For this study, the efficiency η is defined as in equation 5.10. The influence of different radiation attributes (i.e., E_0, E_0/A, A and N) on the luminescence signal is followed individually using a controlled irradiation environment as offered by the Pelletron accelerator. The separate effects will allow us to build a simple model of the energy deposition processes by HCP in the Al_2O_3:C dosimeters.

Table 5.2. Possible permutations of the radiation beam attributes used for studying basic behavioral laws of the luminescence signal, where "≠" stands for "vary parameter", "=" stands for "keep constant"

Experiment type	E_0	A	E_0/A	N (Φ)
Fluence Dependence	=	=	=	≠
Particle Energy Dependence	≠	=	≠	=
Particle Size Dependence (at constant energy / nucleon)	≠	≠	=	=

The possible changes in the luminescence signal (i.e., efficiency) with several HCP parameters such as E_0, E_0/A, A and N are described in Table 5.2, considering three basic situations. In the first type of experiment, fluence is varied and the other parameters are kept constant, in the second type the energy and subsequently, energy/nucleon vary, and in the third type of experiment the energy per nucleon and the fluence are kept the same. The outcomes of each type of experiments, as well as its implications on the dose deposition model, are presented in the following sections.

5.4.1. Fluence Dependence

For irradiations with a specific particle/energy (i.e., protons of 4.0 MeV), the particle's fluence can be varied. At low-fluences, where the HCP tracks are considered to be isolated (i.e., not interact with each other), the OSL/TL signal should be linear. As a result, the efficiency η at low fluences should be constant. If the fluence is increased high enough, the HCP tracks come closer together and several situations, such as track interaction and track overlapping, may occur. Gaza et al. (2004) suggested that track interactions may result in the quenching of the OSL response of Al_2O_3:C to HCP due to particularities in the material. In the case of Al_2O_3:C materials, luminescence centers (i.e., F^+ centers) preexist in the material prior to irradiation and the concentration of F^+ centers was observed to decrease at high doses (Yukihara et al., 2003). The main contribution to the OSL signal is believed to be due to electron recombinations at F^+ centers outside the ion's track. At low fluences, the escaped electrons have a high probability to radiatively recombine with preexisting F^+ centers outside the track inducing a linear response. At high fluences, however, the escaped electrons can reach

the close neighboring tracks where fewer F^+ centers exist resulting in a decrease of the OSL signal. Thus, the OSL response of Al_2O_3:C should be linear-sublinear with increasing fluence (Gaza et al., 2004). In addition to the track interaction effects, if the fluence is increased high enough the tracks may overlap resulting in an increased ionization density along the particle's track and a subsequent quenching of the luminescence signal. Thus, at high fluences (e.g. where the OSL signal is sublinear) the efficiency η should decrease with increasing fluence. This model should also apply for the HCP induced TL signal from the Al_2O_3:C dosimeters. Contrary, for the LiF samples the track interaction effects at high fluences induce an increase in the TL signal resulting in a supralinear fluence response, as already mentioned in Chapter 4.

Examples of the fluence influence on the OSL response from Al_2O_3:C (chips) and Luxel samples, over an extended range of fluences (i.e., $1\times10^7 \div 1\times10^{10}$ part/cm^2), are given in Figure 5.8. Here, the corrected OSL signals $I_{HCP,corr}$ induced by 1.0, 2.0 and 4.0 MeV protons together with the corrected OSL signal induced by 13 MeV carbon are represented as function of fluence. The graphs in Figure 5.8 are represented in a log-log scale and the dashed line represents the linearity line (i.e., line of slope equal to 1). In Figure 5.9, the OSL response from the Luxel samples exposed to protons (1.0 MeV), carbon (13 MeV) and oxygen (10 MeV) is shown.

For the Al_2O_3:C measurements, two samples were exposed per fluence as reflected by the error bars in Figure 5.8, while for the Luxel measurements only one sample was exposed for each fluence, thus no error bars are shown in Figure 5.9. It can be observed from Figure 5.8 and Figure 5.9 that, for both Al_2O_3:C and Luxel samples, the OSL response shows a linear-sublinear behavior with fluence. Since the efficiency η is

proportional (up to a constant) to the slope of the graphs shown in Figures 5.8 and 5.9, it can be easily observed that η is constant up to $\sim 1\times10^{8}$ part/cm^2 in the case of 4.0 MeV protons, followed by a decrease with increasing fluence for fluences larger than $\sim 1\times10^{8}$ part/cm^2. These observations confirm the model predictions outlined above.

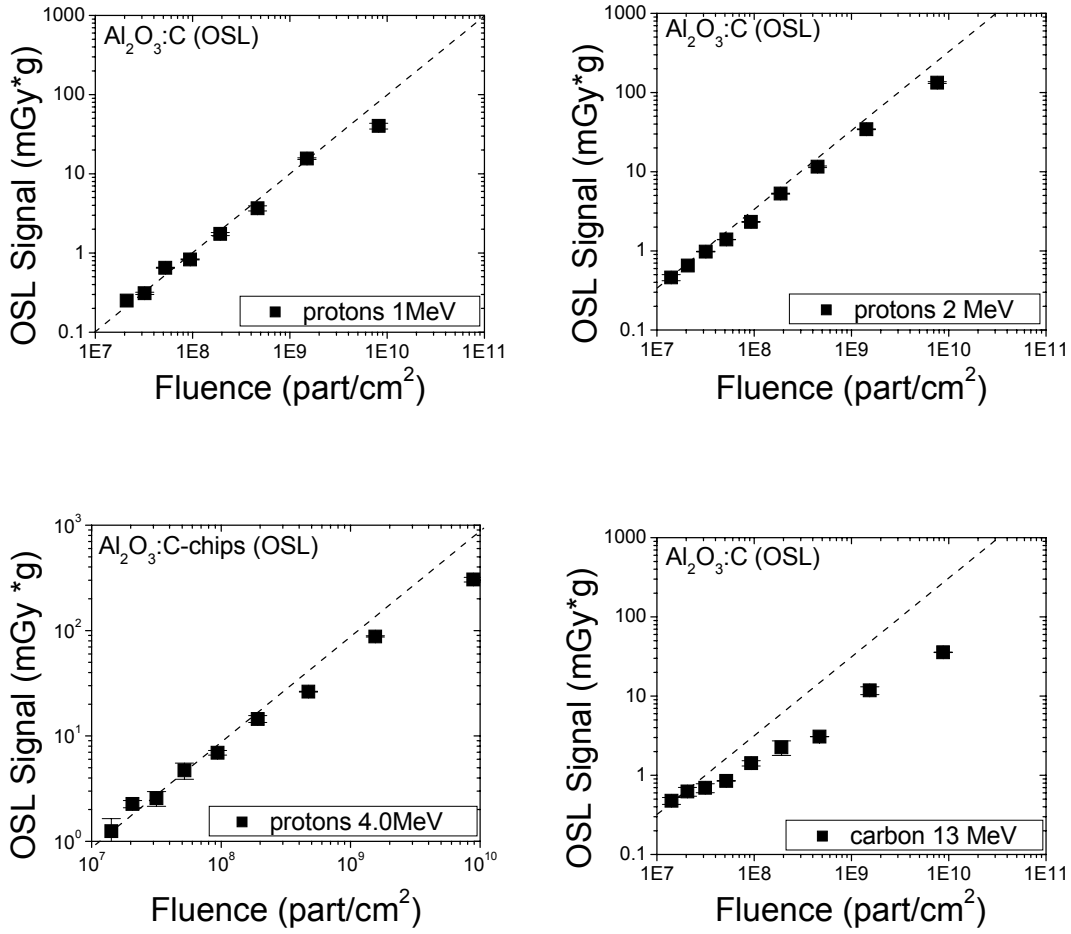

Figure 5.8. The OSL fluence response for Al_2O_3:C exposed to 1.0, 2.0 and 4.0 MeV protons; and 13 MeV carbon. The dashed line is a 1:1 linearity line

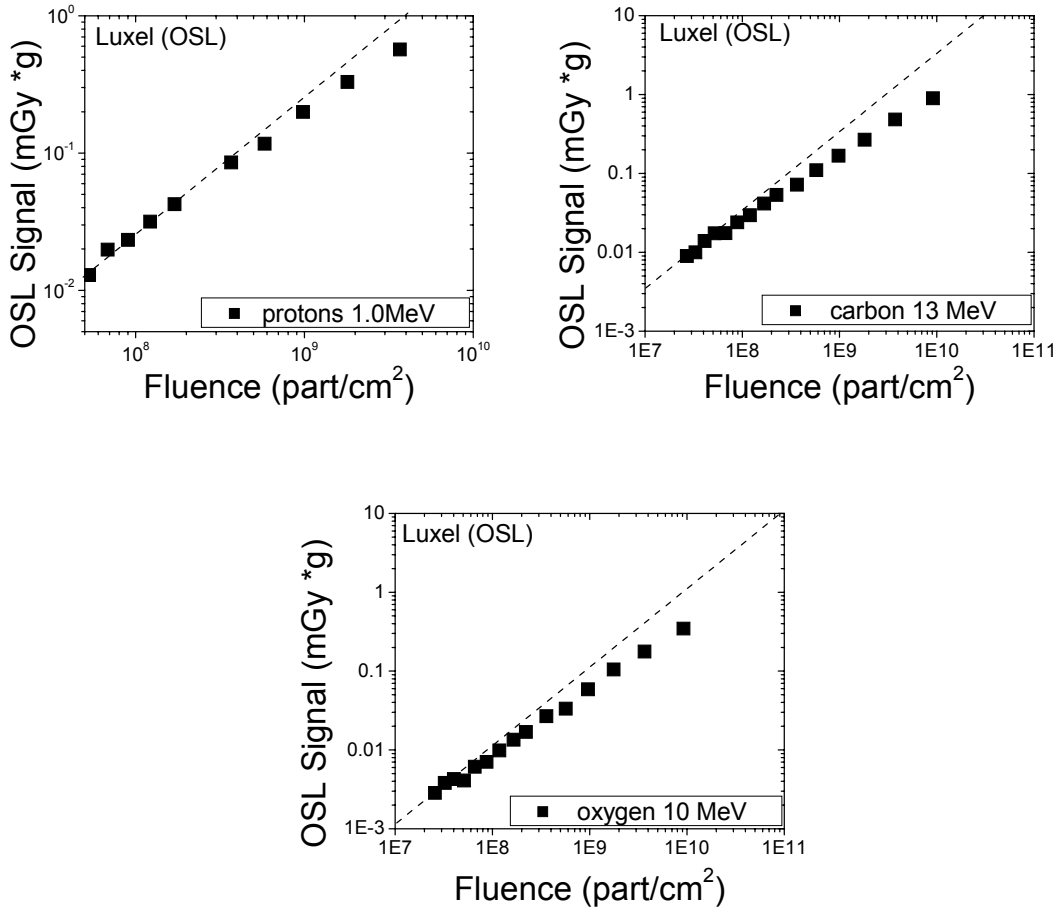

Figure 5.9. The OSL fluence response for Luxel samples exposed to 1.0 MeV protons, 13 MeV carbon and 10 MeV oxygen ions. The dashed line is a 1:1 linearity line

The TL responses from Al_2O_3:C and LiF:Mg,Ti to 4.0 MeV protons are represented as a function of fluence, as shown in Figure 5.10a and Figure 5.10b, respectively. As before, the graphs are represented on a log-log scale and the dashed line represents a 1:1 line. The error bars in Figure 5.10a represent the standard deviation of the mean for three samples. For the LiF measurements only one sample was exposed per fluence. The TL response of Al_2O_3:C exposed to 4.0 MeV protons exhibits a sublinear behavior with increasing fluence, as expected from the model. The LiF samples show a linear response for the investigated fluence range (i.e., $2\times10^7 \div 4\times10^9$ part/cm^2).

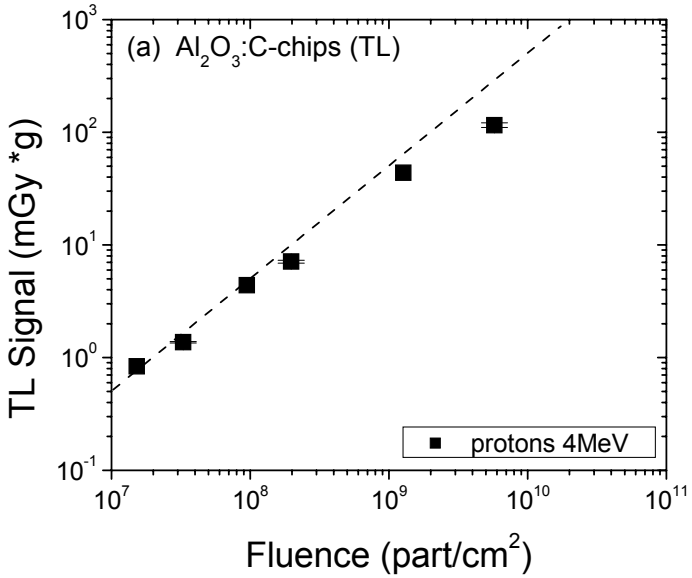

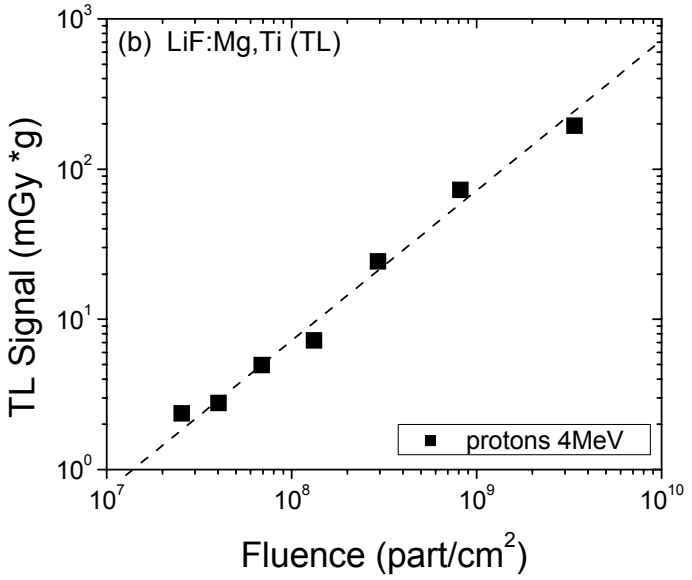

Figure 5.10. The TL fluence response for Al_2O_3:C (a) and LiF:Mg,Ti (b) exposed to 4.0 MeV protons. The dashed line is a 1:1 linearity line

When comparing the OSL fluence response curves from Al_2O_3:C samples irradiated with 1.0, 2.0, and 4.0 MeV protons, it has was observed that the onset of the sublinearity (i.e., the fluence at which the sublinear region starts) depends on the energy and the type

of the incident particle (Gaza et al., 2004). For the same type of particles, the sublinearity has been observed to appear sooner with increasing energy, as shown in Figure 5.11 (Gaza et al., 2004). Gaza and colleagues (2004) attributed this dependence to track interaction effects the changes in the track radius with increasing energy, effects possibly dictated by an increase of the radius of the HCP track with increasing energy. Thus, as the energy increases, the track interaction effects will take place sooner. Nevertheless, Gamboa-deBuen and colleagues (2001) did not observe any significant change in the track radius with increasing energy, when investigating the TL response of LiF dosimeters to 0.7 , 1.5 , and 3.0 MeV protons. The later observation was not expected and remains unexplained.

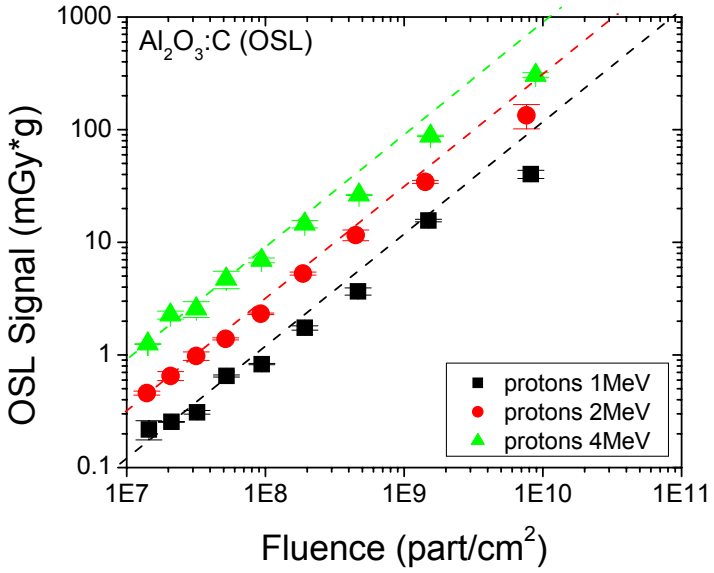

Figure 5.11. The OSL fluence responses for Al_2O_3:C dosimeters exposed to 1.0 , 2.0 and 4.0 MeV protons. The dashed lines represent 1:1 lines

5.4.2. Particle Energy Dependence

Consider irradiations of constant fluence Φ and different energies for a specific

particle (i.e., protons of 1, 2 and 4 MeV). Theoretically, the luminescence signal should increase proportionally to the energy for a given fluence, giving rise to a constant efficiency η with increasing energy. However, Gamboa-deBuen and colleagues (2001) observed an unexpected decrease in the TL signal of LiF at lower energies. A possible explanation for this phenomenon is that as the particle energy is increased, the Bragg peak is expected to appear deeper in the sample, preceded by a longer portion of the track having low LET. Thus, the average ionization density along the track decreases with increasing energy and the luminescence response at higher energies should be higher than expected (Razvan Gaza, personal communication, 2004). As a result, the efficiency η is expected to increase with increasing energy.

An example of the variation of the OSL signal from the Al_2O_3:C samples with increasing particle energy E_0, for constant fluences, is given in Figure 5.12a. The samples were exposed to 1.0, 2.0, and 4.0 MeV protons (fluence of 1.5×10^7 part/cm^2) and to 2.5, 5.0, and 8.9 MeV helium ions (fluence of 1.6×10^7 part/cm^2). The results showed the expected energy dependence with for both proton and helium irradiations. The same dependence was also observed for the TL signal from Al_2O_3:C and LiF:Mg,Ti when exposed to 2.5, 5.0, and 8.9 MeV helium ions (for a given fluence), as shown in Figure 5.12b. Thus, the efficiency η increases with increasing energy for all of the investigated materials/methods and ions/energy combinations as expected.

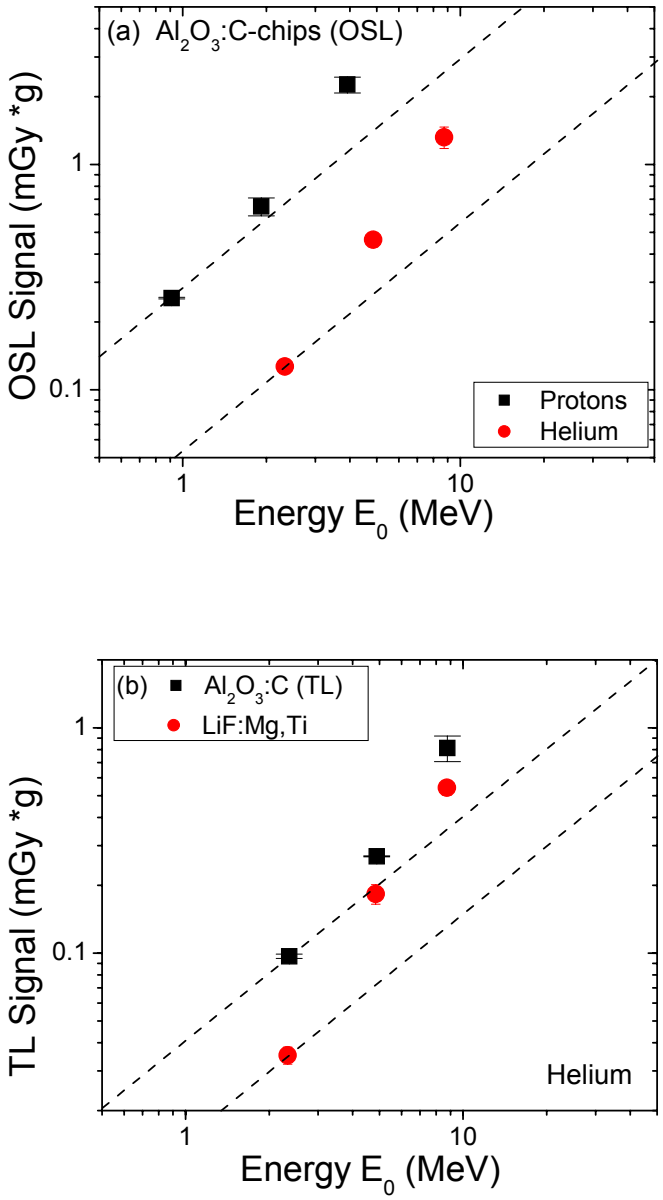

Figure 5.12. The OSL energy response for Al_2O_3:C exposed to protons and helium ions (a) and the TL energy response of Al_2O_3:C LiF:Mg,Ti exposed helium (b). The dashed line is a 'slope 1' line

5.4.3. Particle Size Dependence

For particles with the same energy per nucleon E_0/A, at a given fluence (i.e., H, He

and C with 2.5 MeV/n), Horowitz and colleagues (2001) observed an increase in the dose along the track with increasing energy and atomic number, while the radius of the track did not changed significantly. Assuming that the track geometrical parameters do not change with increasing energy E_0 and mass number A, for constant E_0/A ratios, the ionization density is expected to increase with E_0 and A. As a result, a quenching of the OSL/TL signal should be observed (via saturation effects) and the efficiency η should decrease.

In order to verify the above assumption, the OSL signals from Al_2O_3:C and the TL signals from both Al_2O_3:C and LiF:Mg,Ti exposed to 1.0 MeV protons was compared to the corresponding OSL/TL signals exposed to 12 MeV carbon ions, thus keeping the E_0/A ratios constant (~1). The OSL/TL signals were normalized to the corresponding atomic mass values. The results indicate that the luminescence signals decrease with the atomic number A (shown in Figure 5.13) and with the particle's energy E_0 (not shown). As a result, the corresponding efficiencies decrease with increasing E_0 and A, for constant E_0/A ratios, as expected from the model.

As a conclusion, the presented model regarding the influence of several irradiation parameters such as fluence Φ, energy E_0 and particle size A on the OSL/TL efficiencies from Al_2O_3:C in low-energy HCP fields was confirmed experimentally. Nevertheless, other parameters such as the dimensions of the HCP track and the dose response function of the reference radiation were not considered for the above model, indicating that more complex analysis is needed for calibrating a given OSL or TL dosimeter to low-energy HCP fields.

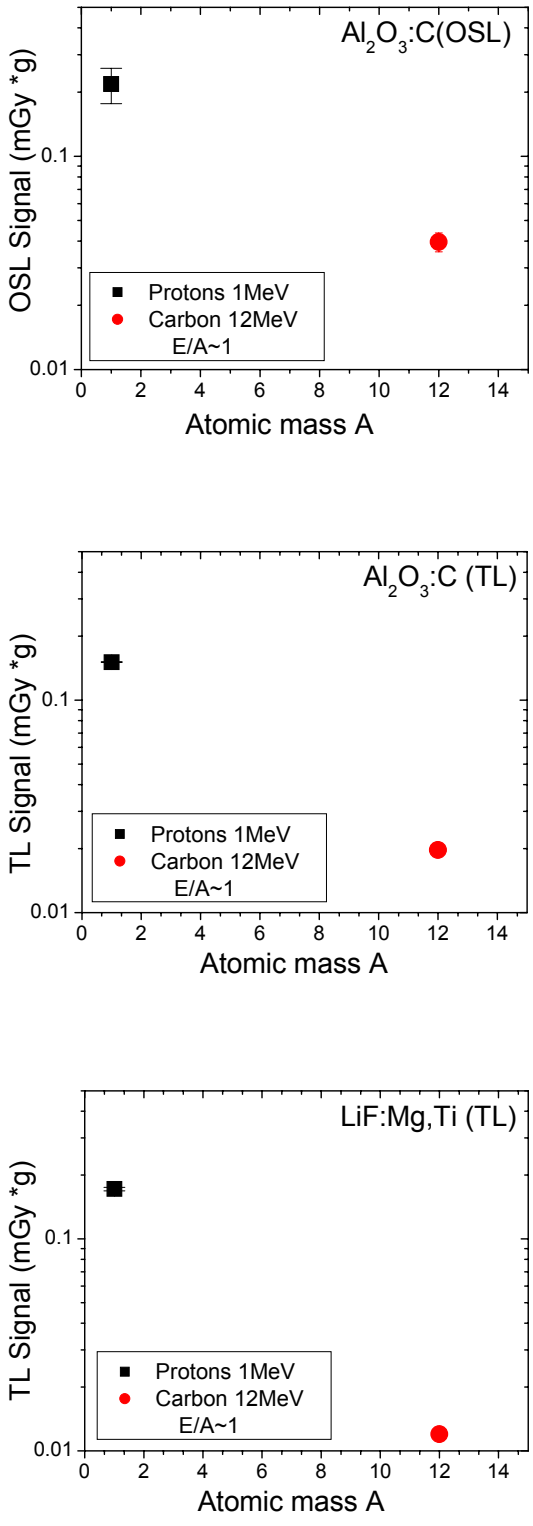

Figure 5.13. Dependence of the OSL/TL signal from Al_2O_3:C and LiF:Mg,Ti irradiated with protons and helium ions of constant energy per nucleon E_0/A

5.5. Additional features regarding the OSL efficiency of Al_2O_3:C to low-energy HCP

In this section, a method of estimating the OSL efficiencies at low doses using the linear-sublinear behavior of the OSL response of Al_2O_3:C to low-energy HCPs is advanced. In addition, possible surface effects on the OSL efficiency from Al_2O_3:C materials when exposed to low-energy HCPs is investigated using both polished and unpolished samples.

5.5.1. Estimating the efficiency by using the dose response curve

For dosimetry purposes, the efficiency η is defined by the equation 5.1 which is valid only for HCP doses in the linear range of the dose response. For particles such as C, it is difficult to isolate the linear region of the dose response and thus, estimating the efficiency, as shown in Figure 5.14. Here, the OSL response is represented as function of the HCP dose (calculated using equation (5.16)), rather than the fluence.

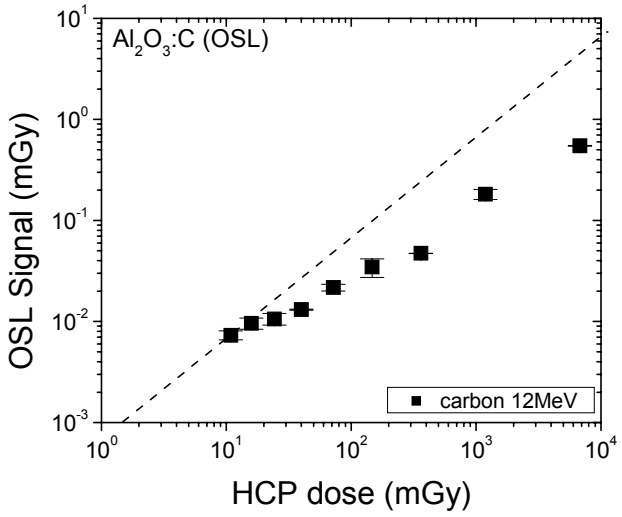

Figure 5.14. The OSL dose response for Al_2O_3:C irradiated with 12 MeV carbon ions

A method of calculating the efficiency by using the whole linear-sublinear OSL curve was developed. As seen from section 5.3., the OSL response of Al_2O_3:C to low-energy HCP shows a linear-sublinear behavior with increasing fluence (dose). By fitting the OSL dose response with a saturating exponential, the OSL sensitivity can be defined as:

$$S(D) = a\left(1 - e^{-bD}\right) \tag{5.17}$$

where D is the dose absorbed in the material and a and b are fitting parameters. Thus, the slope of the OSL dose response curve, defined as in equation (5.17), gives the efficiency:

$$Eff = \lim_{D \to 0} \frac{dS}{dD} = ab \tag{5.18}$$

The efficiency values calculated by combining equations (5.1) and (5.16) and using the data from the linear region of the dose response were compared to the efficiency values calculated by equation (5.18), following the fitting of equation (5.17).

Table 5.3. Efficiency values calculated based on the linear part of the dose response curve (equation 5.1), and using equation (5.17) after fitting the whole dose response curve using equation 5.16, for Al_2O_3:C chips irradiated with protons and carbon ions

Particle (Energy)	Calculated Efficiency (equation 5.1) (Linear range)	Calculated Efficiency (equation 5.17) (Linear-sublinear range)
Protons (1 MeV)	0.39 ± 0.03	0.40 ± 0.05
Protons (2 MeV)	0.46 ± 0.02	0.48 ± 0.03
Protons (4 MeV)	0.69 ± 0.06	0.52 ± 0.02
Carbon (13 MeV)	0.08 ± 0.01	0.02 ± 0.00

The calculated efficiency values (equation 5.18) were found to be in good agreement with the experimental efficiency values (equation 5.1) for the proton irradiations for which the linear region of the dose response is well defined. However, larger differences between the efficiency values calculated using equations (5.1) and (5.18) were obtained for the carbon ions for which the linear region of the dose response is poorly defined. Thus, a better definition of the linearity of the dose response is needed in order to successfully apply equation 5.18.

5.5.2. Surface effects on the OSL efficiency from Al_2O_3:C to low-energy HCP

When dealing with low-energy ions, such as 1.0 and 2.0 MeV protons, the heavy charged particles deposit all of their energy on the surface of the Al_2O_3:C dosimeter (of about 150 μm in thickness) with penetration ranges of about 8 and 25 μm, respectively. The surface of the Al_2O_3:C dosimeters was observed to depend on the heating treatments that the material was exposed to. Thus, following multiple high-temperature annealing procedures of the Al_2O_3:C dosimeters (e.g., standard annealing procedure at temperature equal to 900°C in air), the oxygen (e.g., from the air) can diffuse into the bulk of the material decreasing the concentration of oxygen vacancies at the surface (Akselrod et al., 1993). Since the oxygen vacancies (i.e., $F-$centers) are vital for the luminescence production in Al_2O_3:C, a reduction in the concentration of oxygen vacancies can result in a decrease of the luminescence efficiency. As a result, an 'artificial decrease' in the luminescence efficiency of Al_2O_3:C exposed to such HCP (e.g., with penetration depths comparable to the thickness of the surface layer) should be observed. This feature was investigated by using both unpolished and polished Al_2O_3:C chips and compare their

OSL efficiencies when exposed to 1.0 and 2.0 MeV protons. For the polished samples, a layer of about 70 μm was removed in order to reduce the possible surface effects. For this experiment, the OSL efficiency values were calculated using equation 5.10. The results are shown in Figure 5.15 from where it can be seen that the regarding the presentation of the Al_2O_3:C chips (e.g., polished or unpolished) the OSL efficiency values are the same for the corresponding energy values. Thus, no significant surface effect on the luminescence efficiency was observed for Al_2O_3:C chips exposed to 1.0 and 2.0 MeV protons indicating that there is no need to polish the samples before low-energy HCP irradiations

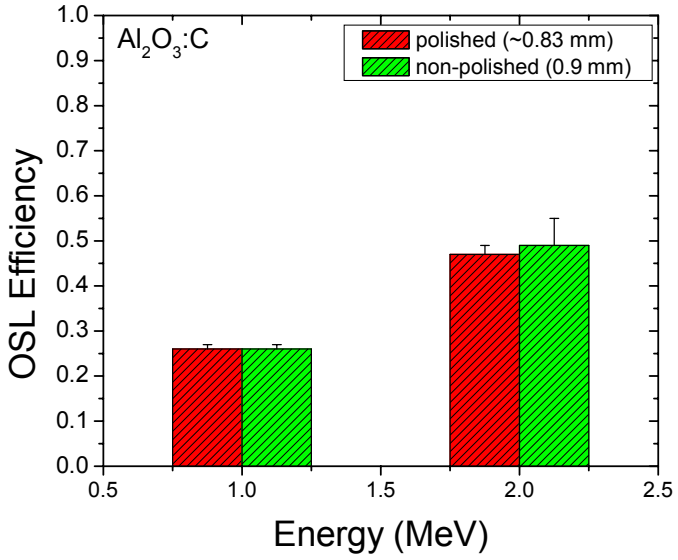

Figure 5.15. The OSL efficiency values for polished and unpolished Al_2O_3:C samples exposed to 1.0 and 2.0 MeV protons

CHAPTER 6

THE LET DEPENDENCE OF THE OSL EFFICIENCY FROM Al_2O_3:C EXPOSED TO HIGH-ENERGY HCPs AND ITS APPLICATIONS TO MIXED RADIATION FIELDS : EXPERIMENTAL RESULTS

6.1. Objective of this chapter and luminescence efficiency considerations

The radiation environment in space is a complex mix of charged particles such as protons, electrons, alpha particles and heavy ions with energy spectra extended over large energy ranges, as shown in Chapter 2. Different particles of different energies have different biological effects on the human body. Thus, a simple radiation detector that measures only the absorbed energy deposited within its volume (i.e., absorbed dose) will not suffice. A good space radiation detector should also give information about the radiation type and energy (i.e., LET). For radiation protection purposes, it is customary to use the linear energy transfer (LET) as a measure of the biological effects of radiation. The linear energy transfer represents the energy deposited by an incident HCP in the detector per unit length, thus being related to the ionization density along the particle's track. Therefore, the linear energy transfer can be used (in the first approximation) as a unifying parameter to quantify the efficiency of a specific radiation detector with respect to the radiation quality. Ideally, a space radiation detector would be equally sensitive to the whole particle/energy radiation spectrum encountered in space. In reality, different types of radiation detectors have different limitations, as discussed in Chapter 1. For personal dosimetry, it was suggested that luminescence detectors (i.e., TLDs and OSLDs)

should be used to measure the low-LET component (i.e., region of $LET < 10$ keV/μm) of the space radiation field (NCRP, 2002). For this portion of the spectrum, the quality factor Q (as defined in Chapter 1) has a value of 1 implying that low-LET particles have similar biological effects. Thus, for the $LET < 10$ keV/μm and $Q = 1$ region, the TL and OSL dosimeters do not have to be an indicator of the radiation characteristics (i.e., type and energy). For the high-LET region (i.e., region of $10 < LET < 100$ keV/μm), the quality factor Q has a strong dependence on LET, as shown in Figure 1.1. Thus, plastic nuclear track detectors (i.e., PNTDs) should be used in this region, since they are more sensitive to high-LET particles than the luminescence detectors, and can also provide information about the LET spectrum of the space radiation. As a consequence, the efficiency of an ideal OSL/TL dosimeter should be equal to one for the $LET < 10$ keV/μm region, and zero for the rest of the LET spectrum. Contrary, an ideal PNTD should only be sensitive for the high-LET region (i.e., $\eta = 1$) and not sensitive to the low-LET region, as illustrated in Figure 6.1.

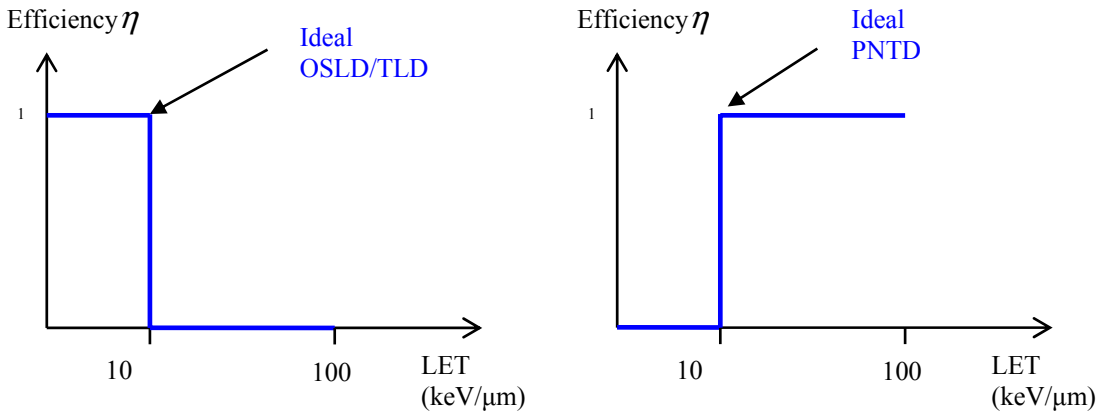

Figure 6.1. Desired efficiency dependence on LET for OSL/TL dosimeters and PNTDs

Thus, for space radiation fields, the radiation protection quantity of interest is the dose equivalent defined as:

$$H = D_{OSLD/TLD} + \int Q(L)\, D_{PNTD}(L)\, dL \tag{6.1}$$

Here, $D_{OSLD/TLD}$ is the absorbed dose measured by OSLD/TLD; D_{PNTD} is the absorbed dose measured by PNTDs and $Q(L)$ is the quality factor. In practice, the efficiencies of luminescence and plastic nuclear track detectors exhibit more complicating dependences on the linear energy transfer. An example of the efficiency vs LET dependence for ^{7}LiF (TLD-700) exposed to several types of HCPs is given in Figure 6.2 (Benton & Benton, 2000).

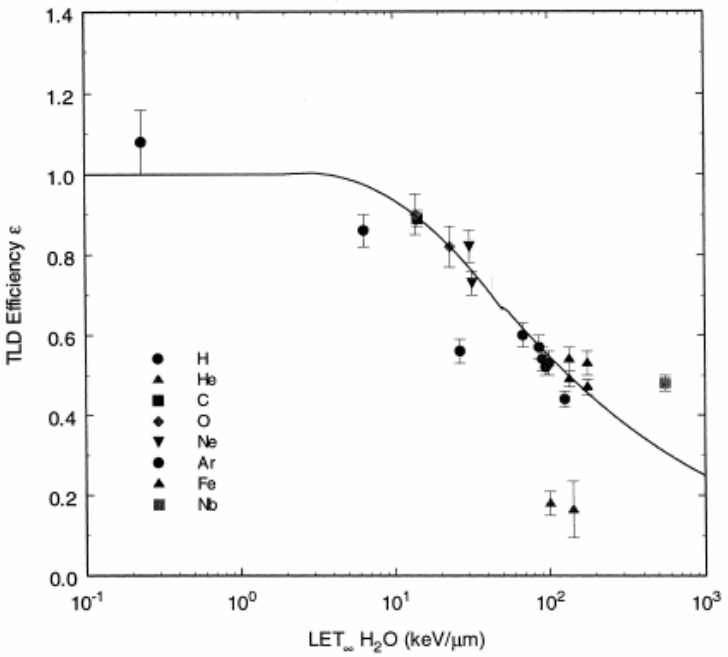

Figure 6.2. Dependence of the TLD efficiency of LET (in water) for TLD-700 (Benton & Benton, 2000)

Here, the TL efficiency ε (equivalent to η defined in equation (5.1) and calculated using a similar relation) is represented as function of the LET in water (e.g., standard

representation). It can be seen from Figure 6.2 that the TLD efficiency ε has an over-response for $LET < 1$ and decreases from $80-50\,\%$ for the high-LET part of the curve (i.e., $20 < LET < 200$ keV/μm). Thus, the efficiency of a luminescence detector should be investigated also for the high-LET region of the space radiation spectrum in order to characterize as well as possible the response of the detector over a wide range of LET.

Another important observation from Figure 6.2 is that for particles with the same LET the efficiency seems to be dictated by the particle's charge number Z, leading to the conclusion that the LET is not a unifying parameter as assumed before (Geiβ et al., 1998; Benton & Benton, 2000). This hypothesis was also confirmed in Chapter 4, when the luminescence efficiency η of a specific material was found to depend on several parameters such the type/energy/size of the incident particle. In addition, η depends on the ionization density along particle track, the dose response function of the reference radiation field and the experimental conditions (Horowitz et al., 2001; Gamboa-deBuen et al., 2001). As a consequence, the efficiency vs. LET curve is not unique for a given dosimeter, but rather depends on the particle characteristics, as shown in Figure 6.2 (for protons and helium ions).

Nevertheless, methods such the high-temperature ratio (HTR) for LiF, were proposed in an attempt to measure the absorbed dose in unknown complex mixed fields similar to space radiation (Vana et al., 1996; Hajek et al., 2002). The HTR is defined as the ratio between the TL signal in the high temperature region (225 to $300\,°C$) after irradiation in an unknown field to the intensity of the TL emission in the same temperature region after irradiation with a reference ^{60}Co source, where both TL curves are normalized to the intensity of peak 5 (Schöner et al., 1999). For LiF materials (i.e.,

TLD-100, TLD-600 and TLD-700), the main dosimetric peak (peak 5) was found to decrease with increasing LET, while the high-temperature peak (225 - 300 °C) was found to increase with increasing LET. This behavior has been exploited by Vana and colleagues (1996) by the use of the HTR method to assess a so-called 'averaged LET' of space radiation fields (Vana et al., 1996). However, Yasuda and Fujitaka showed previously that for mixed fields there is a significant difference between the 'average LET' obtained by the HTR method and the actual average LET value, which may result in underestimation of the quality factor and, subsequently, the dose equivalent (Yasuda & Fujitaka, 1999).

The TL response to heavy charged particles (i.e., TL efficiency) for materials such as LiF:Mg,Ti and CaF_2:Tm has been studied in great detail over the years. In contrast, there is a lack of data regarding the HCP-induced OSL efficiency for materials such as Al_2O_3:C. Yasuda and colleagues (2002) investigated the OSL response of Al_2O_3:C to relativistic ions and observed a decrease in the OSL efficiency, up to 40 %, with increasing LET for LET values between 2.2 and 198 keV/μm (in water). A more recent study of the OSL response of Al_2O_3:C to high-energy HCP was done by Yukihara and colleagues (2004) as part of the 2nd ICCHIBAN project using the HIMAC accelerator in Chiba, Japan. Here, the authors investigated the properties of the OSL efficiency for two types of Al_2O_3:C materials (i.e., Al_2O_3:C chips and Luxel) to several high-energy ions such as helium (150 MeV/u), carbon (400 MeV/u), silicon (490 MeV/u), and iron (500 MeV/u). The experimental results indicated that the luminescence efficiency depends on the material type (i.e., Al_2O_3:C chips and Luxel), measurement technique (i.e., OSL and TL) and the definition of the OSL signal (i.e., integrated OSL and initial

intensity), as shown in Figure 6.3.

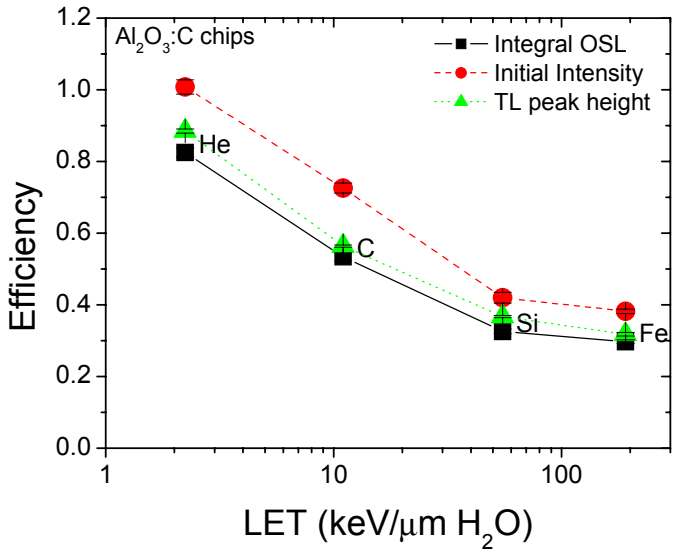

Figure 6.3. CW-OSL efficiencies from Al_2O_3:C chips exposed to high-energy heavy ions (adapted from Yukihara et al., 2004)

In addition, Yukihara and colleagues observed a change in the shape of the CW-OSL signal from Al_2O_3:C as function of the radiation type (i.e., LET), as previously noted by Yasuda and colleagues (2002). This change in the shape of the OSL decay curves was attributed to differences in the mean dose along the particle tracks (Yukihara et al., 2004). Accordingly, the efficiency values for Al_2O_3 should be different for different definitions of the OSL signal (i.e., integral OSL or initial intensity).

The purpose of this chapter is to characterize the dependence of the OSL efficiency from Al_2O_3:C materials to high-energy particles for those particles expected to be part of the space radiation field, for both the low- and high-LET regions. The efficiency vs. LET dependence was investigated using several high-energy HCPs using the HIMAC

accelerator at Chiba, Japan, and the experimental results will be presented in the next sections. In addition, the hypothesis that information regarding the 'mean efficiency' η_{mean} is contained in the shape of the OSL decay curve from Al_2O_3 was investigated, using several approaches in the analysis of the OSL data. This analysis was applied to various mixed field irradiations performed at the HIMAC facility, Chiba, Japan. The results of this analysis will also be discussed. In the last section, several efficiency calibration curves for Al_2O_3:C, Luxel, LiF:Mg,Ti (TLD-100) and CaF_2:Tm (TLD-300) obtained from several irradiations at the HIMAC accelerator at Chiba, Japan, the proton facility at Loma Linda, CA, and the NSRL facility at Brookhaven, NY, will be presented.

6.2. OSL efficiency vs. LET calibration curves for Al_2O_3:C materials

The efficiency of the luminescence emission depends on the LET of the incident particle. The efficiency of a HCP irradiated dosimeter to gamma is defined as follows (e.g., similar definition to equation 5.1):

$$\eta = \frac{S_{HCP}/D_{HCP}}{S_R/D_R} \tag{6.2}$$

Here, S_{HCP} is the luminescence signal after a HCP irradiation of dose D_{HCP} and S_R is the signal of a sample subject to a reference radiation of dose D_R. As a reminder, equation (6.2) is valid only for D_R and D_{HCP} in the linear range of the dose response. The reported quantity is the gamma dose to water D_γ and represents that gamma dose needed to obtain the same OSL signal from a gamma-irradiated sample as from a HCP-irradiated sample:

$$D_\gamma = D_R \times \frac{S_{HCP}}{S_R} \tag{6.3}$$

Thus, the efficiency η becomes:

$$\eta = \frac{D_\gamma}{D_{HCP}} \tag{6.4}$$

6.2.1. Exposure details

The experiments were performed as part of the 4th ICCHIBAN research project using heavy ions at the National Institute of Radiological Sciences (NIRS) in Chiba, Japan. Two types of Al_2O_3:C dosimeters (i.e., Al_2O_3:C chips and Luxel) were exposed to several high-energy ions with nominal energies ranging from 600 MeV up to 28 GeV, with a corresponding LET range from $2.2\,\text{keV/}\mu\text{m}$ up to $\sim 200\,\text{keV/}\mu\text{m}$, using the HIMAC (Heavy Ion Medical Accelerator in Chiba) accelerator at NIRS. The samples were annealed using standard annealing/bleaching procedures already described in Chapter 3 and Chapter 5. The calibration of the samples was done according to the procedure presented in detail in section 5.2. Both the Al_2O_3:C and the Luxel samples were analyzed using a Risø TL/OSL-DA-15 reader in OSL mode, using U-340 filters, as previously described in Chapter 5. The OSL signal from Al_2O_3:C was defined in two ways, namely: the Initial Intensity OSL (i.e., the average of the OSL signal for the first 3 seconds) and the Integral OSL (i.e., the integral OSL signal over the first 300 seconds).

6.2.2. OSL decay curves from Al_2O_3:C exposed to heavy ions

An example of normalized OSL decay curves from Al_2O_3:C chips exposed to $^{90}Sr/^{90}Y$

beta radiation and two different heavy ions (i.e., 145 MeV/n ^{4}He and 367 MeV/n ^{20}Ne) is given in Figure 6.4. Here, the OSL signal was normalized to the initial intensity to allow a direct comparison between the OSL decay curves. The OSL from Al_2O_3:C was observed to decay faster with increasing linear energy transfer (LET), as previously noted by different authors (Yasuda et al., 2002; Yukihara et al., 2004). The same behavior was also observed for the Luxel samples (not shown here).

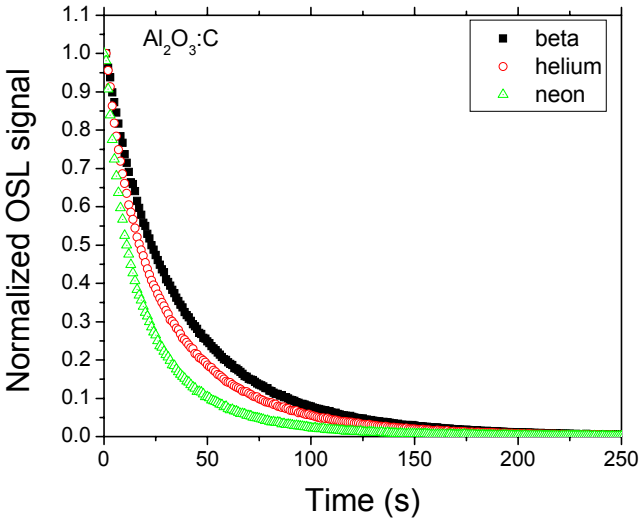

Figure 6.4. OSL decay curves of Al_2O_3:C chips exposed to 150 mGy of beta radiation and to 10 mGy of helium and neon ions

6.2.3. OSL efficiency results for Al_2O_3

The Al_2O_3 samples were exposed to several heavy charged particles, such as: 150 MeV/n ^{4}He, 400 MeV/n ^{12}C, 400 MeV/n ^{20}Ne, and 500 MeV/n ^{56}Fe. The HCP doses (i.e., equal to10 mGy) were in the linear region of the dose response for all of the investigated ions (Gaza et al., 2003; Yukihara et al., 2004). The corresponding efficiency values of the Al_2O_3 materials at producing OSL were calculated using equation (6.4) for

the two definitions of the OSL signal, namely: the Initial intensity OSL and the Integral OSL. The efficiencies were found to depend on the type of Al_2O_3:C material and, for a specific OSL material, on the definition of the OSL signal, as shown in Table 6.1. These results agree with previous measurements by Yukihara and colleagues (2004). The difference in the efficiencies corresponding to a specific definition of the OSL signal (i.e., Integral OSL and Initial Intensity) for a given material (i.e., Al_2O_3:C or Luxel) was exploited in order to obtain information about LET via R-method (Yukihara et al., 2004).

Table 6.1. Efficiency values for Al_2O_3:C and LiF:Mg,Ti corresponding to different OSL/TL parameters

	Al_2O_3:C (chips)		Luxel	
Particle	OSL Area (300 s)	Initial Intensity	OSL Area (300 s)	Initial Intensity
^{4}He	0.848 ± 0.037	1.02 ± 0.05	1.04 ± 0.01	1.28 ± 0.02
^{12}C	0.548 ± 0.022	0.748 ± 0.044	0.833 ± 0.001	1.32 ± 0.01
^{20}Ne	0.411 ± 0.009	0.585 ± 0.017	0.599 ± 0.002	1.00 ± 0.01
^{56}Fe	0.313 ± 0.006	0.417 ± 0.015	0.423 ± 0.004	0.634 ± 0.018

The dependence of the OSL efficiency values (i.e., using integral OSL over the first 300s) for the Al_2O_3:C (chips) and Luxel samples as function of LET is shown in Figure 6.5, together with the corresponding efficiency values previously obtained during the 2nd ICCHIBAN experiment (Yukihara et al., 2004). The OSL signal was measured repeatedly for three different samples exposed to the same ion/energy combination. The efficiency values were averaged over the three values, resulting in the error bars in Figure

6.5. Also, the initial intensity method of estimating the efficiency for all of the investigated materials showed consistency between the two experiments (not presented here).

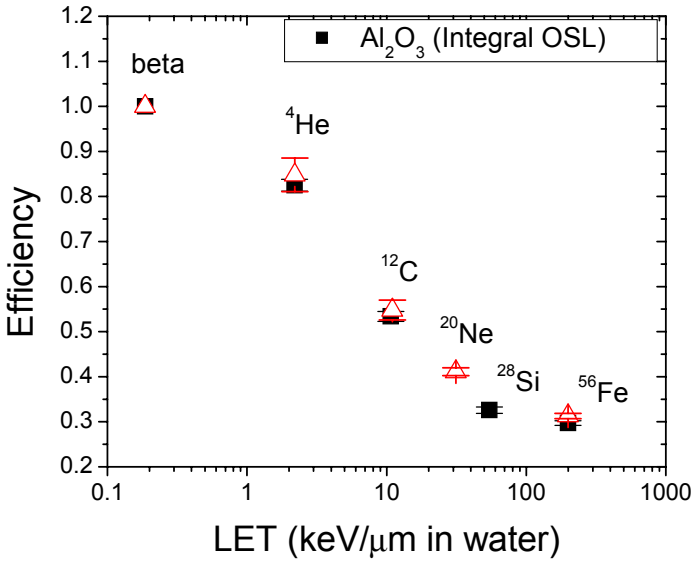

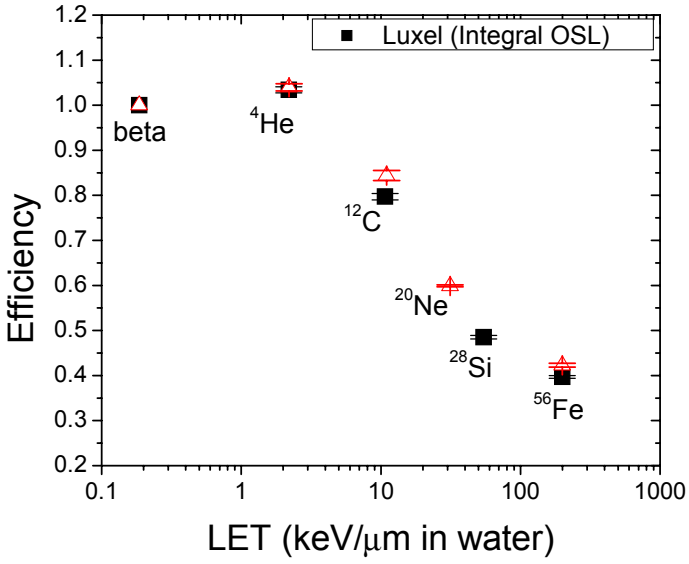

Figure 6.5. Comparison of the efficiency values for Al_2O_3 and Luxel from 2nd and 4th ICCHIBAN (Black symbols – 2nd ICCHIBAN; Red symbols – 4th ICCHIBAN)

6.3. Investigated methods to obtain the absorbed dose for unknown mixed radiation fields using the OSL signal from Al_2O_3:C

For known radiation fields, D_{HCP} is known and D_γ can be obtained by using equation (6.3). For mixed radiation fields, the total absorbed dose D in the OSL dosimeter is calculated by considering the contribution of the different types of radiation, as follows:

$$D = \sum_i D_i = \sum_i \frac{D_{\gamma,i}}{\eta_i} \tag{6.5}$$

In order to determine the absorbed dose according to equation (6.5), it is necessary to know the individual doses D_i for the investigated mixed radiation field. For unknown mixed radiation fields, the individual doses D_i cannot be obtained. In this section we test the possibility of introducing a 'mean efficiency' η_{mean}, that can be used in conjunction with the total dose D_γ (i.e., $D_\gamma = \sum_i D_{\gamma,i}$) measured for an unknown mixed radiation exposure in order to determine the actual absorbed dose without determining first the individual contributions of different types of radiation to the OSL signal, according to:

$$D = \frac{D_\gamma}{\eta_{mean}} \tag{6.6}$$

For the low-LET spectrum, where $Q = 1$, the absorbed dose D has the same meaning as the dose equivalent H. For the high-LET region, where $Q = Q(L)$, information about the 'mean LET' is needed in order to correct the absorbed dose and obtain H, i.e., $H = DQ(L)$. Thus, we need to determine if the 'mean LET' can be used to calculate a

'mean quality factor' that can enable us to obtain information about the dose equivalent.

The experiment was performed in two different ways: 'known-ion' exposures (using single-ion radiation fields) and 'unknown-ion' exposures (i.e., using both single and mixed-ion radiation fields). The purpose of performing the 'known-ion' exposures was to obtain a calibrated efficiency vs. LET curve, whereas the 'unknown-ion' exposures were used to obtain information about the absorbed dose and the dose equivalent via two different methods of quantifying the shape of the OSL decay curve from Al_2O_3:C (e.g., $R-$method and $\tau-$method).

The $R-$method considers the ratio of the integrated OSL intensity for beta irradiation to the integrated OSL intensity for HCP irradiation after normalization of the curves to the initial intensity and displays these R values as a function of the LET of the HCP. Then, by comparing the R value for a mixed field irradiation with the R versus LET curve one can perhaps estimate a 'mean LET', which can yield in turn a 'mean efficiency', as illustrated in Figure 6.6. However, a difficulty with this approach, as noted by Gaza et al. (2004), is that for certain ranges of LET the *R* value is not single valued. This causes substantial uncertainties in which 'mean LET' value to use, and similar uncertainties in the 'mean efficiency'.

An alternative approach to the $R-$method is the $\tau-$method and was applied by Gaza and colleagues (2004) to estimate the 'mean LET' and the corresponding 'mean efficiency' values for Luxel samples exposed to several high-energy heavy ions. Here, the OSL decay curves were fitted with a sum of *k* exponentials thus:

$$I_{OSL} = \sum_k A_k \exp\left(-\frac{t}{t_k}\right) \tag{6.7}$$

The fitted parameter τ, where $\tau = t_1/t_2$ from a two or three exponential fit, was found to depend on the LET of the radiation, as presented in Figure 6.7a. Following this, the 'mean efficiency' was determined, as illustrated in Figure 6.7b.

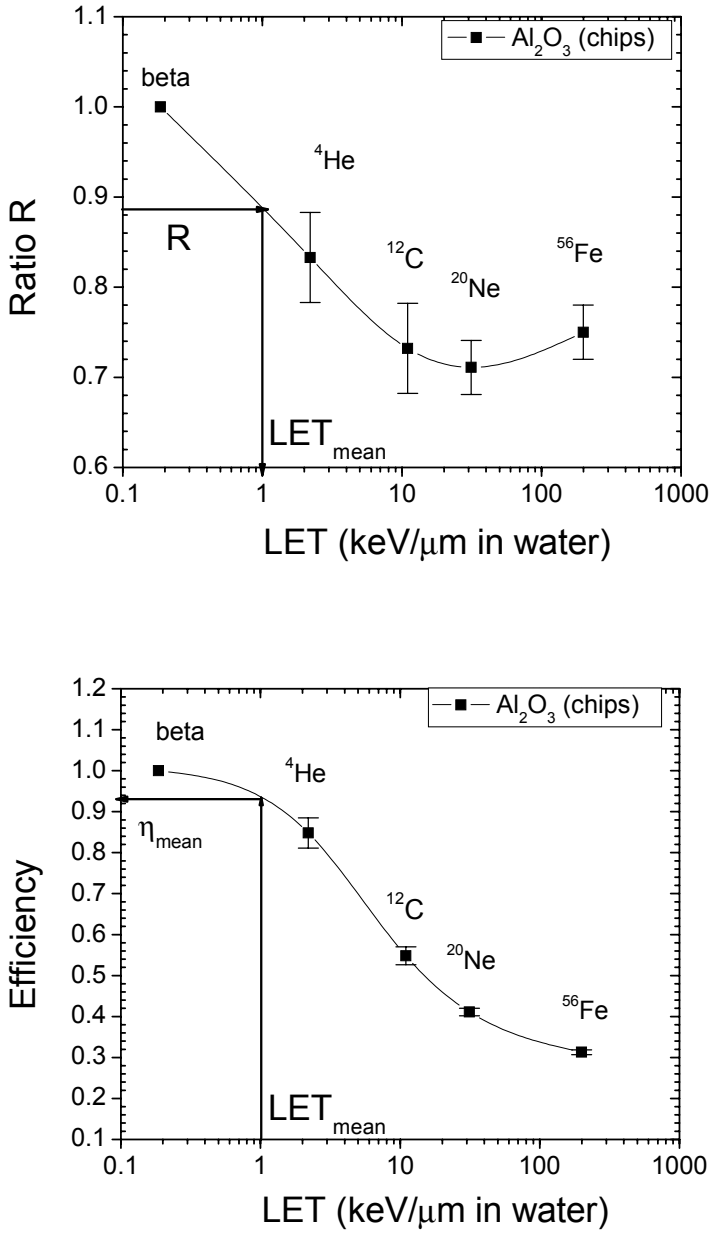

Figure 6.6. Ratio R – method illustrated for the OSL signal of Al_2O_3:C (chips)

As a result, the measured gamma dose was corrected by the 'mean efficiency' (using equation 6.6) in order to obtain the absorbed dose. This calculated absorbed dose was then compared with the actual absorbed dose delivered to the mixed-ion exposures. The results are presented in Table 6.2 (Gaza et al., 2004).

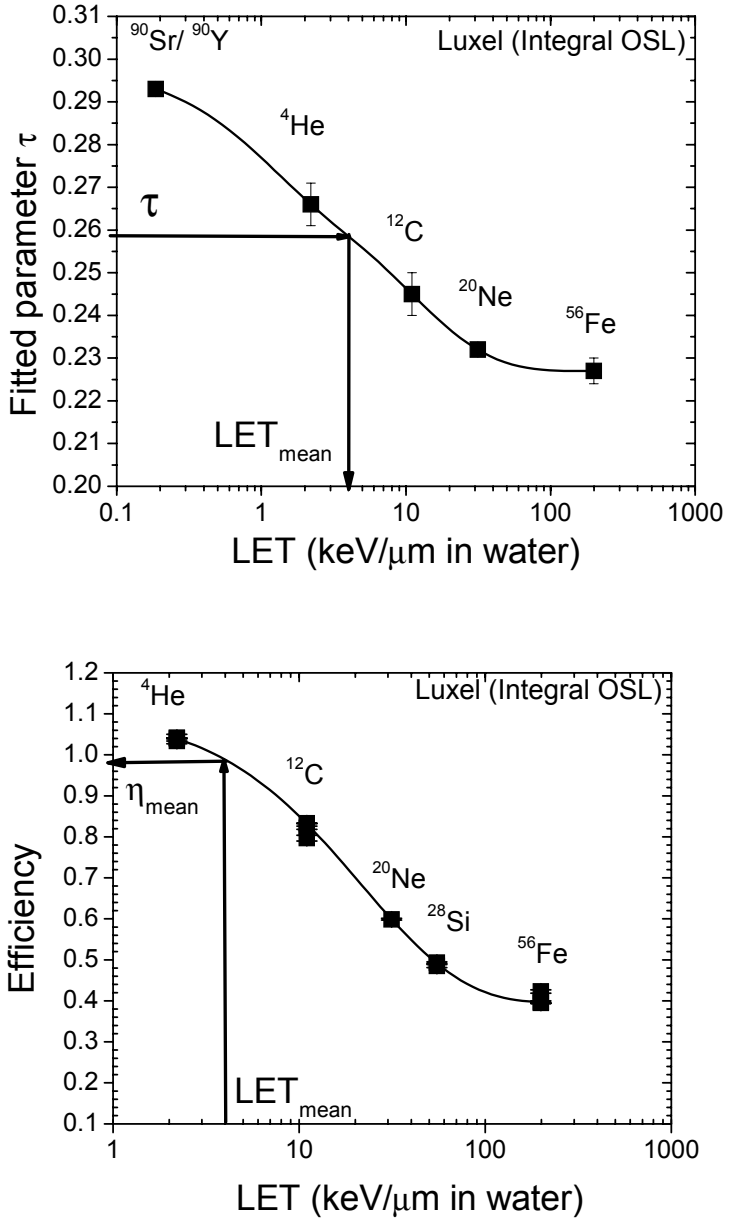

Figure 6.7. The τ – method applied for Luxel using the fitted parameter vs. LET curve (a) and the efficiency vs. LET curve (b) for different ion exposures (Gaza et al., 2004)

Furthermore, one can use the 'mean LET' to estimate a value for Q (ICRP 60, 1991). From this value, and knowing the corrected gamma dose (i.e., absorbed dose) an estimated value for the dose equivalent can be obtained, using $H = QD$. These 'corrected' dose equivalent values may then be compared with the actual dose equivalent values calculated according to $H = \sum_i H_i = \sum_i D_i \times Q_i$, as shown in Table 6.3.

Table 6.2. Comparison between the 'corrected' absorbed doses and the actual absorbed doses, using the 'mean efficiency' values estimated by the $\tau-$method, as applied for the Luxel samples

'Unknown-ion' exposure	Uncorrected D_γ dose (mGy)	Corrected D Integral OSL (mGy) ($\tau-$method)	Actual Absorbed Dose (mGy)
Unknown #1	31.0 ± 0.2	28.5 ± 0.3	27.8
Unknown #2	26.2 ± 0.1	25.3 ± 0.4	25.0
Unknown #3	13.4 ± 0.1	12.5 ± 0.2	12.6
Unknown #4	8.4 ± 0.1	11.2 ± 1.0	10.2
Unknown #5	20.8 ± 0.2	25.4 ± 1.3	25.0

It is observed from Table 6.2 that the $\tau-$method can be used in order to estimate the absorbed dose for both unknown single-ion exposures and unknown mixed-ion exposures, if the composition of the mixed field is dominated by low-LET radiation (e.g., Unknown #1, #2, #3, #5). Nevertheless, if the mixed field has a strong contribution from high-LET radiation (e.g., Unknown #4), the $\tau-$method will give larger errors (up to 10 %) when estimating the absorbed dose. Also, considering the strong dependence of Q on L for high-LET particles, significant additional errors are introduced when the estimating

the dose equivalent, compared with the actual dose equivalent (Table 6.3). Similar results were obtained by applying the $R-$method to the Luxel samples (Gaza et al., 2004).

Table 6.3. Comparison between the dose equivalent values and the 'corrected' absorbed doses, using the 'mean LET' values estimated by the $\tau-$method, as applied for Luxel

'Unknown-ion' exposure	Dose equivalent H (Sv)	Corrected Dose equivalent (Sv) (τ – method)
Unknown #1	27.8	28.5 ± 0.3
Unknown #2	25.0	25.3 ± 0.4
Unknown #3	20.4	12.5 ± 0.2
Unknown #4	64.9	35.7 ± 1.0
Unknown #5	33.0	25.4 ± 1.3

6.4. OSL and TL calibration curves for Al_2O_3:C, Luxel, LiF:Mg,Ti and CaF_2:Tm exposed to high-energy HCPs

In this section, the efficiency vs. LET calibration curves were obtained for several types of luminescence dosimeters (i.e., Al_2O_3:C, Luxel, LiF:Mg,Ti (TLD-100) and CaF_2:Tm (TLD-300)) using high-energy HCP radiation exposures, as shown in Table 6.4. In addition, calibration curves using the $R-$method (for Al_2O_3:C and Luxel), the HTR method (for TLD-100) and the peak $5+6$ / peak 3 method (for TLD-300) were obtained. These calibration curves will be used in Chapter 7 in order to obtain information about the absorbed dose D and equivalent dose H for several space radiation exposures.

The samples were irradiated with several types of HCP as shown in Table 6.4. Here,

the absorbed doses together with the nominal energies and the corresponding LET values are shown. The nominal energy values were provided by the experiment organizers and the corresponding LET values were calculated using the SRIM-2003 software[iv].

Table 6.4. Exposure details for the investigated materials for several projects between May 2002 and June 2004 using several irradiation facilities such as the HIMAC accelerator (Japan), the proton facility (Loma Linda) and the NSRL facility (Brookhaven)

Particle	Nominal Energy (MeV/n)	LET (keV/μm in water)	Absorbed Dose (mGy)	Materials	Project (Date)
^{1}H	70	1.0	5, 50, 100	Luxel	Proton Icchiban (Sep 2003)
^{1}H	70	1.0	100, 300	Luxel	Loma Linda (July 2004)
^{1}H	155	0.55	20, 50, 225	Luxel	Proton Icchiban (Sep 2003)
^{1}H	230	0.42	12, 110, 400	Luxel	Proton Icchiban (Sep 2003)
^{1}H	250	0.40	50, 100, 300, 1000	Luxel	Loma Linda (July 2004)
^{4}He	150	2.2	1, 10, 50, 100	Al_2O_3:C, Luxel, TLD-100	2^{nd} Icchiban (May 2002)
^{4}He	150	2.2	10	Al_2O_3:C, Luxel, TLD-100	4^{th} Icchiban (May 2003)
^{4}He	150	2.2	3, 10, 50, 100, 300, 1000, 3000	Al_2O_3:C, Luxel, TLD-100, TLD-300	HIMAC-1 (Feb 2004)

[iv] SRIM 2003 can be found at http://www.srim.org/

^{12}C	135	24	10, 50, 100	Al_2O_3:C, Luxel, TLD-100, TLD-300	HIMAC-1 (Feb 2004)
^{12}C	135	24	50	Al_2O_3:C, Luxel, TLD-100, TLD-300	6th Icchiban (May 2004)
^{12}C	400	11	1, 10, 50, 100	Al_2O_3:C, Luxel, TLD-100	2nd Icchiban (May 2002)
^{12}C	400	11	10	Al_2O_3:C, Luxel, TLD-100	4th Icchiban (May 2003)
^{20}Ne	400	31	10	Al_2O_3:C, Luxel, TLD-100	4th Icchiban (May 2003)
^{28}Si	400	55	1, 10, 50, 100	Al_2O_3:C, Luxel, TLD-100	2nd Icchiban (May 2002)
^{28}Si	600	50	50	Al_2O_3:C, Luxel, TLD-100, TLD-300	NSRL (Mar 2004)
^{40}Ar	500	96	50	Al_2O_3:C, Luxel, TLD-100, TLD-300	6th Icchiban (June 2004)
^{56}Fe	500	190	1, 10, 50, 100	Al_2O_3:C, Luxel, TLD-100	2nd Icchiban (May 2002
^{56}Fe	500	199	10	Al_2O_3:C, Luxel, TLD-100	4th Icchiban (May 2003)
^{56}Fe	500	198	10, 50, 100	Al_2O_3:C, Luxel, TLD-100, TLD-300	HIMAC-1 (Feb 2004)
^{84}Kr	400	459	50	Al_2O_3:C, Luxel, TLD-100, TLD-300	6th Icchiban (June 2004)

The samples were placed in polycarbonate Lexan detector holders, as shown in Figure

6.8. The Al_2O_3:C and Luxel samples were read in CW-OSL mode and the TLD-100 and TLD-300 samples were read in TL mode using a Risø TL/OSL-DA-15 reader. Details of the readout procedures are given in Table 6.5. The OSL/TL efficiency values were calculated for all of the materials using equation 6.4 and are represented as function of the linear energy transfer as shown in Figures 6.9a (Al_2O_3:C), 6.10a (Luxel), 6.11a (TLD-100) and 6.12a (TLD-300).

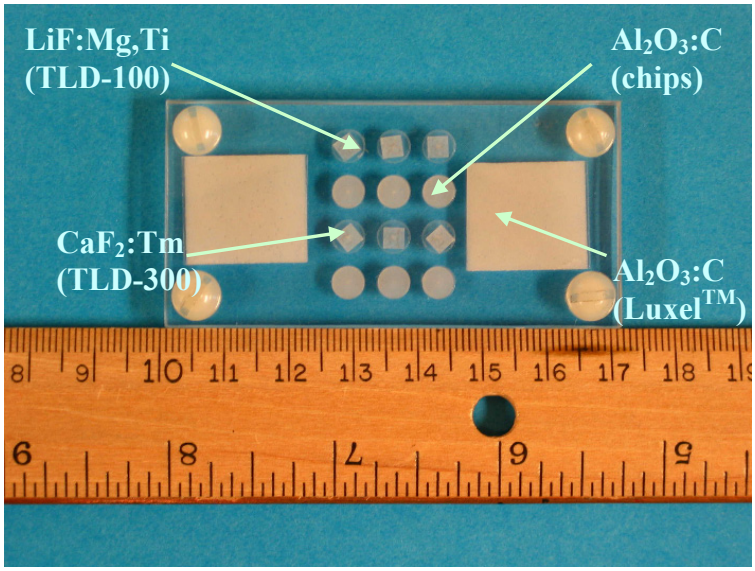

Figure 6.8. The detector package used for the HCP radiation exposures

Table 6.5. Summary of the readout techniques used for different types of dosimeters

Particle	Al_2O_3:C (chips)	Al_2O_3:C (Luxel™)	LiF:Mg,Ti (TLD-100)	CaF_2:Tm (TLD-300)
Annealing/ Bleaching	900 ºC for 15 minutes	Yellow light for 12 h	400 ºC for 1 h & 100 ºC for 2	400 ºC for 1 h
Measurement Technique	CW-OSL	CW-OSL	TL	TL
Stimulation wavelength	525 nm	525 nm		
Heating Rate	-	-	1 ºC/s	1 ºC/s
Optical Filtration	U-340	U-340	none	none

Several methods for extracting information about the 'mean efficiency' and the 'mean LET' from the OSL/TL curves were applied. For the Al_2O_3:C dosimeters the R – method was used and the results are shown in figure 6.9.

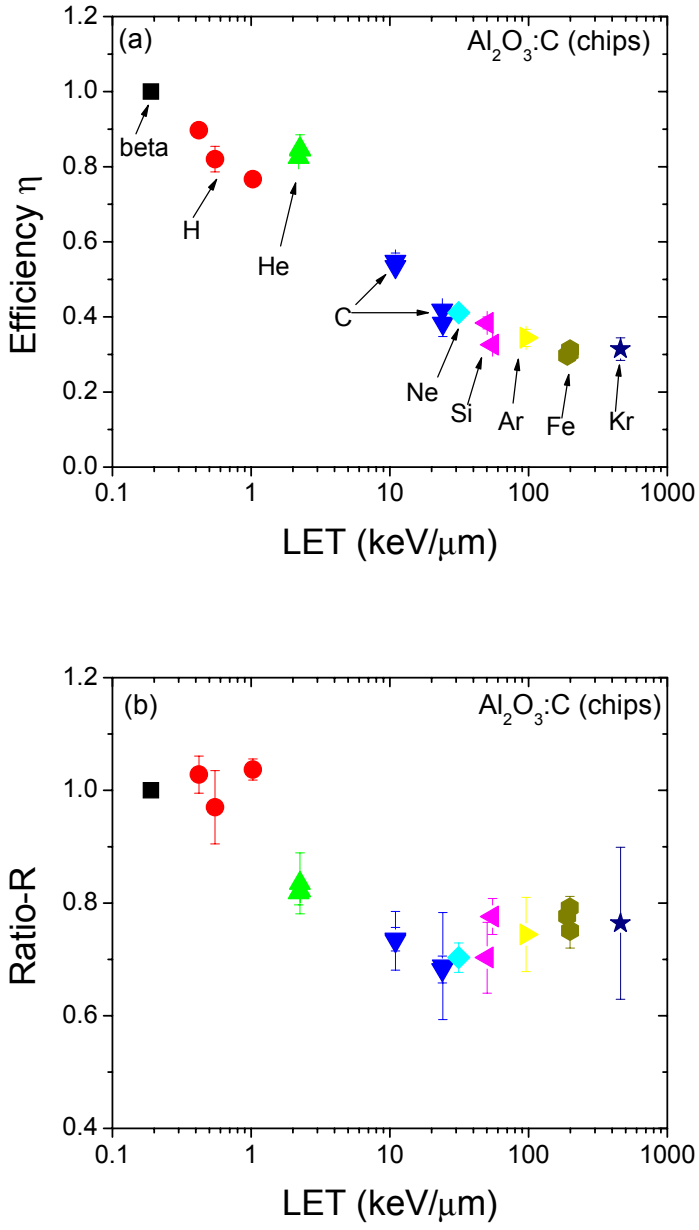

Figure 6.9. The R – method applied for the Al_2O_3:C samples using the efficiency vs. LET curve (a) and R vs. LET curve (b) for different HCP radiation exposures

The efficiency values in Figure 6.9a were obtained by averaging the efficiencies for different doses used for the same ion/energy combination (as shown in Table 6.4), exposing three samples per dose. The color/symbol code used to distinguish between different ion irradiations, shown in Figure 6.9, is also valid for Figures 6.10, 6.11 and 6.12. The proton data presented in Figure 6.9 are from the Proton ICCHIBAN project and are not to be trusted completely since the experiment organizers were not able to provide the actual absorbed doses. Since both Al_2O_3:C and Luxel samples were used for the Proton ICCHIBAN, the corresponding efficiency values were corrected by a correction factor obtained from subsequent proton irradiations of Luxel samples using the same energy range as that used for the Proton ICCHIBAN experiment. It can be seen from Figure 6.9b that the R dependence on the LET is not a single valued function, making it difficult to be used for unknown radiation fields (i.e., space applications).

Both the $R-$method and the $\tau-$method were used for the Luxel samples, as illustrated in Figure 6.10.

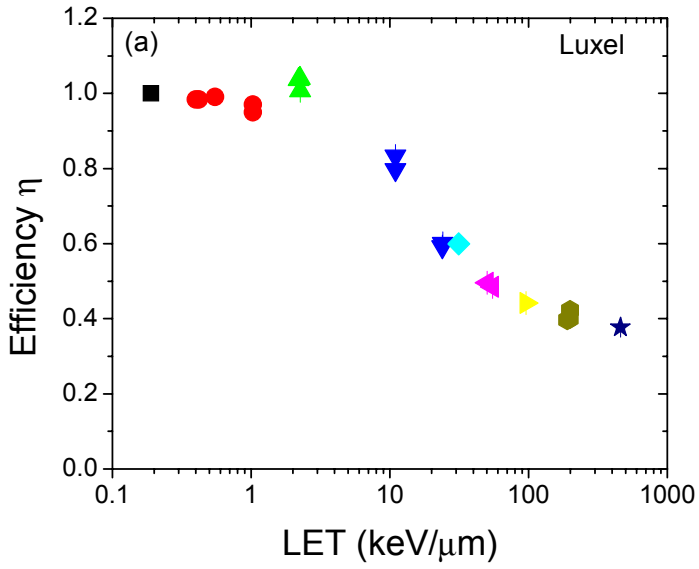

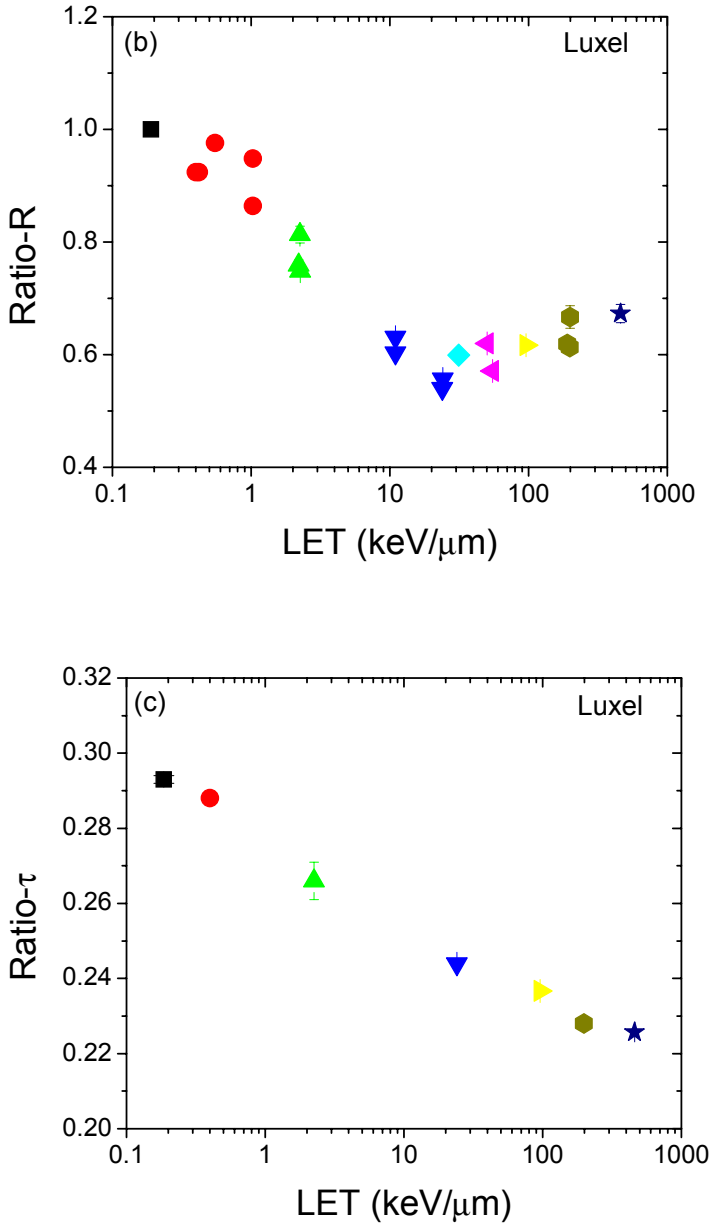

Figure 6.10. The $R-$ and $\tau-$ methods applied to Luxel using the efficiency vs. LET curve (a), the R vs. LET curve (b) and the τ vs. LET curve (c), for different HCPs

The τ values were calculated for selected HCP exposed to the same radiation dose (i.e., 50 mGy). As shown in figure 6.10, the τ vs. LET curve appears to be a single valued function for the corresponding ions/energies/doses used. This feature makes the

τ – method more appealing to be used for space applications. Nevertheless, this method requires increased reproducibility between different measurements and the margins of error need to be reduced in order to obtain good results.

The HTR method was applied to the TLD-100 chips and the resulting calibration curves are shown in Figure 6.11. The HTR values seem to reach a saturation plateau at about $500\,\text{keV/}\mu\text{m}$ even though the data are highly scattered in that region. For the CaF_2:Tm samples, the $\text{peak}\,5+6\,/\,\text{peak}\,3$ method was applied and the results are shown in Figure 6.12.

The $\text{peak}\,5+6\,/\,\text{peak}\,3$ method for TLD-300 is similar to the HTR method for LiF and considers the ratio between the TL signal for the $\text{peak}\,5+6$ (200 to $300\,°\text{C}$) from after irradiation in an unknown field to the intensity of the TL emission in the same temperature region after irradiation with a reference ^{60}Co source, where both TL curves are normalized to the intensity of peak 3 (i.e., the main dosimetric peak in TLD-300). It can be seen from Figures 6.11b and 6.12b the both the HTR vs. LET curve (for LiF) and the $\text{peak}\,5+6\,/\,\text{peak}\,3$ vs. LET curve (for CaF) are not single valued functions, presenting the same problems in estimating the 'mean LET' as the R – method for Al_2O_3:C.

All of the presented calibration curves will be used in the following chapter in order to obtain information about the 'mean efficiency' and 'mean LET' for space applications.

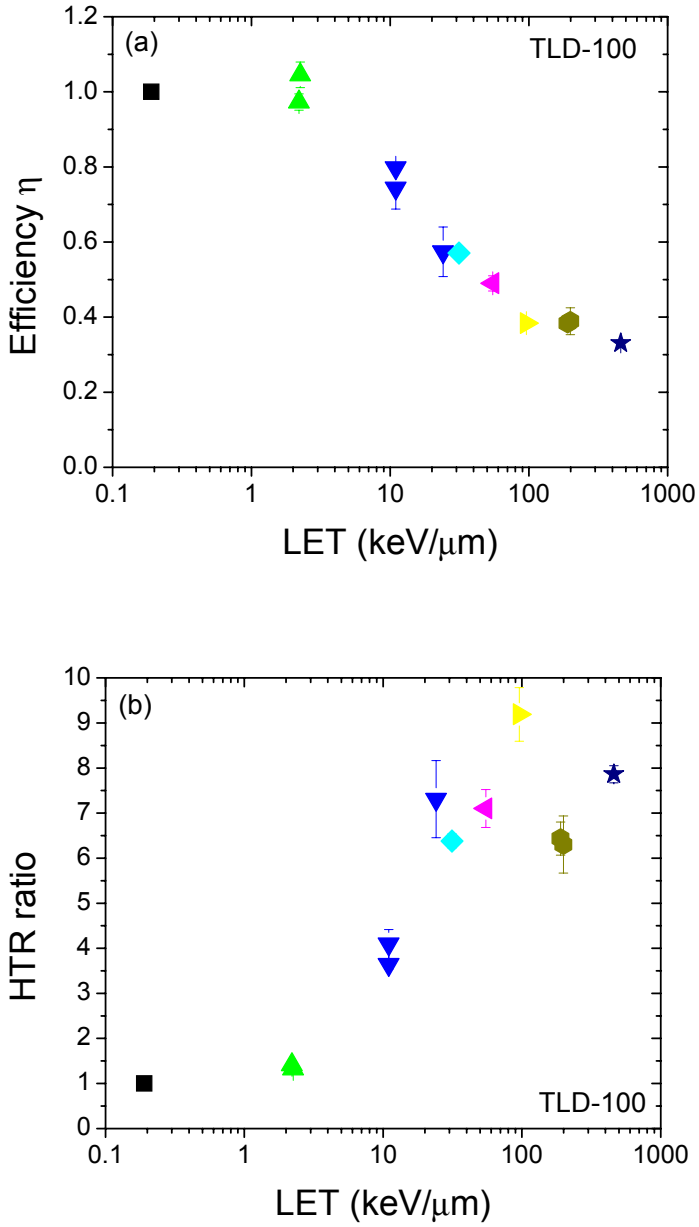

Figure 6.11. The HTR method applied to TLD-100 using the efficiency vs. LET curve (a) and the HTR vs. LET curve (b) for different HCP radiation exposures

.

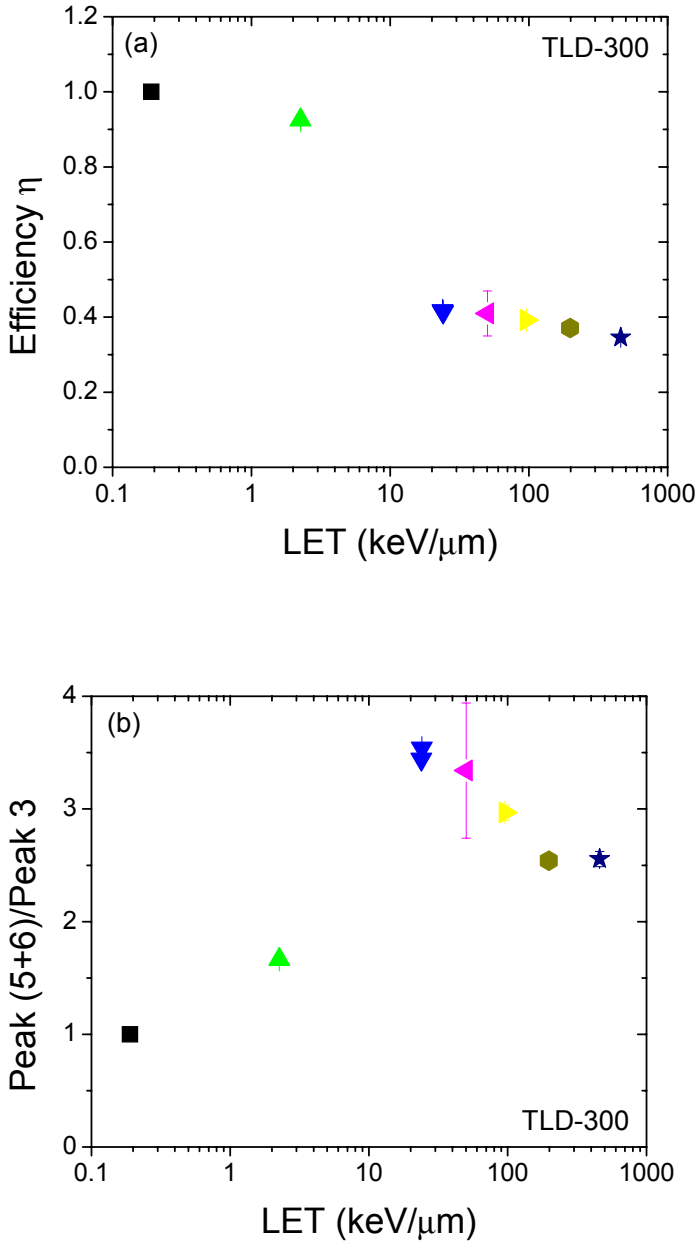

Figure 6.12. The peak $5+6$ / peak 3 method applied to TLD-300 using the efficiency vs. LET curve (a) and the peak $5+6$ / peak vs. LET curve (b) for different HCP exposures

Form the graphs presented in Figures 6.9-6.12, the efficiency η vs. LET curve seem to depend only on LET, being independent on other parameters such as the particle's charge Z. However, it can seen from Figure 6.13, where the data from the low-energy

HCPs (i.e., UNAM projects) and the data from the high-energy projects (Figure 6.9a) are shown together, that each particle seems to have its own η vs. LET curve. This prediction was made by several authors from both Monte Carlo calculations and low-energy ion irradiations experimental results (Geiβ et al., 1998; Avila et al., 1999; Benton et al., 2000).

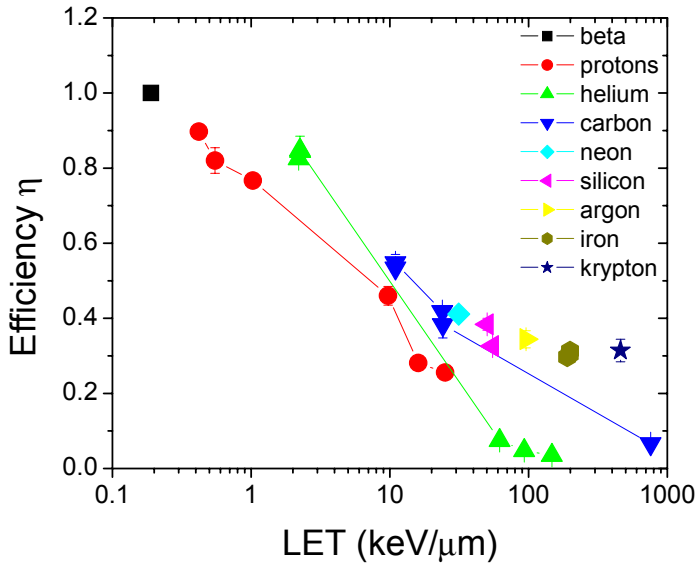

Figure 6.13. Efficiency data for Al_2O_3:C chips exposed to low-and high-energy heavy charged particles as function of the corresponding LET values

As a conclusion, future research is needed in order to calibrate properly common used luminescence dosimeters for both the low-LET and the high-LET part of the radiation spectrum. In the meantime, methods such as the $R-$method and the $\tau-$method can be used to obtain information about the LET for unknown single particle fields from the OSL of Al_2O_3:C materials, thus allowing for the correction of the measured gamma dose by the efficiency, in order to obtain the absorbed dose. Nevertheless, using the presented methods one cannot estimate quantitatively the components of a mixed field.

Thus, further investigation is needed in order to efficiently extract LET information from the OSL curves of Al_2O_3:C.

CHAPTER 7

SPACE RADIATION MEASUREMENTS IN LOW-EARTH ORBIT: EXPERIMENTAL RESULTS

7.1. Space radiation projects

The possibility of using Al_2O_3:C luminescence dosimeters for space applications was investigated in three different projects: the STS-105 project (July 2001) in collaboration with Edward Semones from Johnson Space Center (JSC), the International BRADOS experiment (Jan 2004) and the Antarctica Balloon Flight, both in collaboration with Eric Benton from Eril Research, CA. Besides Al_2O_3:C, other luminescence dosimeters such as LiF:Mg,Ti (TLD-100), CaF_2:Tm (TLD-300) and LiF:Mg,Cu,P (GR-200A) were used. The exposure details together with the corresponding OSL/TL results will be presented in the following subsections. The reported quantity is gamma dose to water D_γ as defined in equation 6.3. In addition, the calibration curves presented in section 6.4 will be used to correct D_γ by the efficiency and obtain the corresponding absorbed doses (i.e., corrected gamma doses). A discussion of the space measurements results is provided in section 7.5.

7.2. Discovery STS-105 and International Space Station (ISS) Irradiations

Several luminescence dosimeters (i.e., Al_2O_3:C chips, TLD-100 and TLD-300) were flown aboard the shuttle Discovery during the STS-105 mission. The samples were placed in the forward mid-deck in the medical locker (ATD) for the 11-day mission, being returned back to Earth with the STS-105 crew. In addition several dosimeters (i.e.,

TLD-100, TLD-300 and GR-200A) were left on board the International Space Station for about 130 days. The ISS samples were placed at four different locations inside the International Space Station, as follows: the TLD-100 and TLD-300 samples were placed at two different locations (i.e., SM-P307 and SM-P339) as part of the radiation area monitor dosimeter package in the Service Module, while the TLD-300 and GR-200A samples were placed at two different locations (i.e., LAB1-D3 and LAB1-PD2) in the Lab. A picture showing the position of the dosimeter package in SM-P307 is given in Figure 7.1, courtesy of Edward Semones of the NASA Space Radiation Analysis Group (SRAG) at JSC. No major solar particles events took place during the STS-105 and ISS exposures.

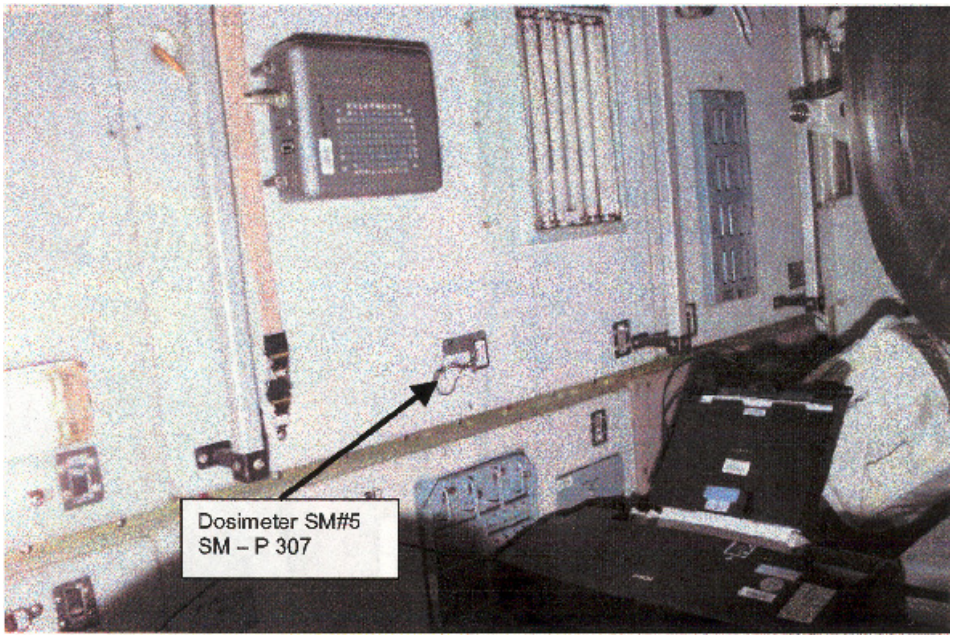

Figure 7.1. Placement of the dosimeters inside ISS (Service Module SM-P307)

After their return on Earth, the dosimeters were analyzed in the laboratory using a Risø TL/OSL-DA-15 reader, in TL mode. The heating rate was 1°C/s. The annealing and calibration procedures for a specific material were already described in Chapter 6. For the

GR-200A material, an annealing of 10 minutes at 240 °C was applied. The results, presented in terms of the uncorrected gamma dose, are given in Table 7.1.

Table 7.1. The uncorrected gamma dose values for the STS-105 and ISS exposures

	Uncorrected gamma dose (mGy) (Al_2O_3:C)	Uncorrected gamma dose (mGy) (TLD-100)	Uncorrected gamma dose (mGy) (TLD-300)	Uncorrected gamma dose (mGy) (GR-200A)
Shuttle STS-105				
ATD	1.46 ± 0.06	1.78 ± 0.14	1.36 ± 0.11	N/A
ISS Locations				
SM-P307	N/A	21.0 ± 0.5	17.4 ± 0.4	N/A
SM-P339	N/A	19.3 ± 1.3	N/A	N/A
LAB D3	N/A	N/A	29.5 ± 0.4	39.8 ± 2.0
LAB PD2	N/A	N/A	N/A	28.9 ± 5.7

As can be seen from Table 7.1, the measured gamma doses vary from material to material, depending also on the location of the dosimeters inside ISS. The gamma doses from the shuttle project could not be corrected for the efficiency since the corresponding luminescence signals were extremely low and since both the HTR and the $\text{peak}\,5+6/\text{peak}\,3$ methods cannot be applied without a good definition of the high-temperature region of the glow-curves. Thus, only the gamma doses from the TLD-100 and TLD-300 measurements exposed inside the ISS were corrected by the efficiency, via the HTR method and the $\text{peak}\,5+6/\text{peak}\,3$ method, respectively. The results are shown

in Table 7.2. Also, the gamma doses from the GR-200A samples exposed on ISS could not be corrected since no calibration curves are currently available for GR-200A.

Table 7.2. The absorbed doses for TLD-100 and TLD-300 exposed on ISS

	Absorbed dose (mGy) (TLD-100)	Absorbed dose (mGy) (TLD-300)
SM-P307	21.2 ± 0.5	17.6 ± 0.4
SM-P339	19.3 ± 1.3	N/A
LAB D3	N/A	33.1 ± 1.2
LAB PD2	N/A	N/A

It can be seen from Table 7.2 that the dose rate ranged from $135 \pm 8\,\mu$Gy/d to $255 \pm 9\,\mu$Gy/d depending on the location inside the ISS.

7.3. BRADOS space radiation exposures on ISS

Luminescence dosimeters such as Al_2O_3:C (i.e., TLD-500 chips from Harshaw/Bicron) and LiF:Mg,Ti (TLD-100) samples were launched aboard the Russian Progress space vehicle on January 29th, 2004 as part of the space project BRADOS. The samples were placed on the wall of the Engineer's cabin in the Russian segment of ISS (#443 panel) and returned back to Earth on April 30th after spending 41.5 days in the Low-Earth Orbit. The exposure took place during a quiet solar period (i.e., no major SPEs). The samples were placed inside nine Lexan holders. The holders containing the OSL/TL dosimeters were stacked in layers alternatively with the CR-39 detectors and formed a compact package that was placed inside a metal box provided by the experiment

organizers together with the detector holders from the other participants, as shown in Figure 7.2.

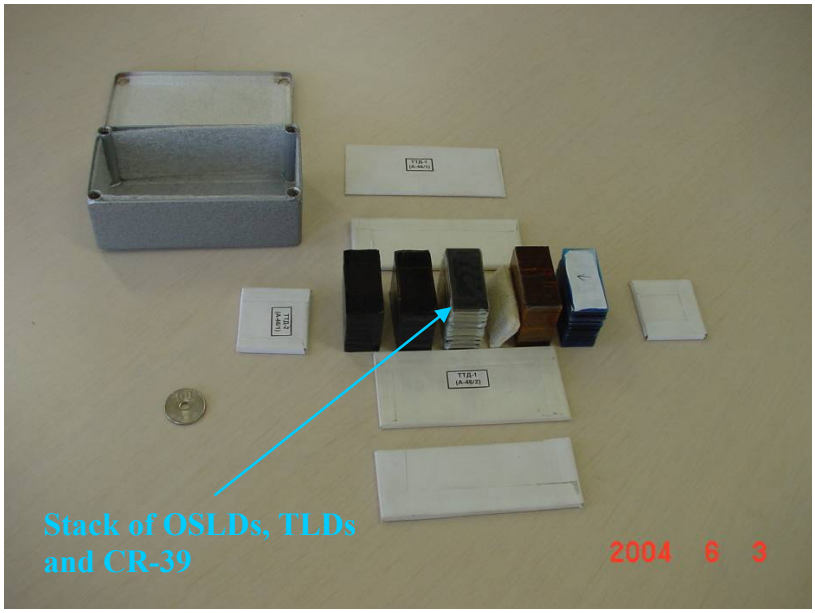

Figure 7.2. Picture of the detector holders used for the BRADOS experiment

The TLD-500 samples were analyzed in OSL mode and the TLD-100 samples were analyzed in TL mode using the corresponding standard annealing/readout procedures as outlined in Table 6.5. The resulting uncorrected gamma dose values are presented in Table 7.3, where the detector #1 is from the top of the stack and detector #9 is from the bottom. The dose values showed a somewhat decreasing trend as function of the depth inside the stack. The $R-$method was applied to the Al_2O_3:C samples and the HTR method was applied to the LiF:Mg,Ti dosimeters. The R and HTR values calculated for each layer by using the definitions provided in section 6.4 are represented in Figure 7.3. It can be seen from Figure 7.3 that both the R values and the HTR values are fairly constant for the all nine layers. The lack of difference between the R and HTR values as function of depth suggests that the luminescence signal is due primarily to the low-LET

particles having a small contribution from the high-LET particles. In order to obtain the absorbed dose values (i.e., corrected gamma dose values by the efficiency), the calibration curves shown in Figure 6.9 were applied for the Al_2O_3:C samples, while the calibration curves shown in Figure 6.11 were applied for the TLD-100 chips. The results are presented in Table 7.4.

Table 7.3. The uncorrected gamma doses for the Al_2O_3:C (TLD-500) and LiF:Mg,Ti (TLD-100) samples

Layer #	TLD-500 D_γ (mGy) Integral OSL	TLD-500 D_γ (mGy) Initial Int.	TLD-100 D_γ (mGy) Peak Height	TLD-100 D_γ (mGy) Area HT
1	16.8 ± 0.1	19.1 ± 0.5	22.1 ± 0.5	36.2 ± 0.8
2	16.2 ± 0.6	17.3 ± 0.8	21.6 ± 0.4	36.2 ± 3.2
3	16.0 ± 0.8	17.8 ± 1.3	22.1 ± 0.4	33.8 ± 1.9
4	15.0 ± 1.3	16.7 ± 1.9	20.2 ± 0.5	32.1 ± 0.4
5	16.8 ± 0.7	19.1 ± 0.6	20.7 ± 0.9	32.0 ± 1.0
6	15.1 ± 0.2	16.8 ± 0.3	19.8 ± 0.7	34.1 ± 1.3
7	15.2 ± 0.2	17.5 ± 0.6	19.4 ± 1.1	31.0 ± 0.4
8	14.5 ± 0.3	15.7 ± 0.5	19.4 ± 0.1	30.5 ± 0.7
9	14.3 ± 0.6	15.9 ± 1.0	19.2 ± 0.1	32.2 ± 1.0

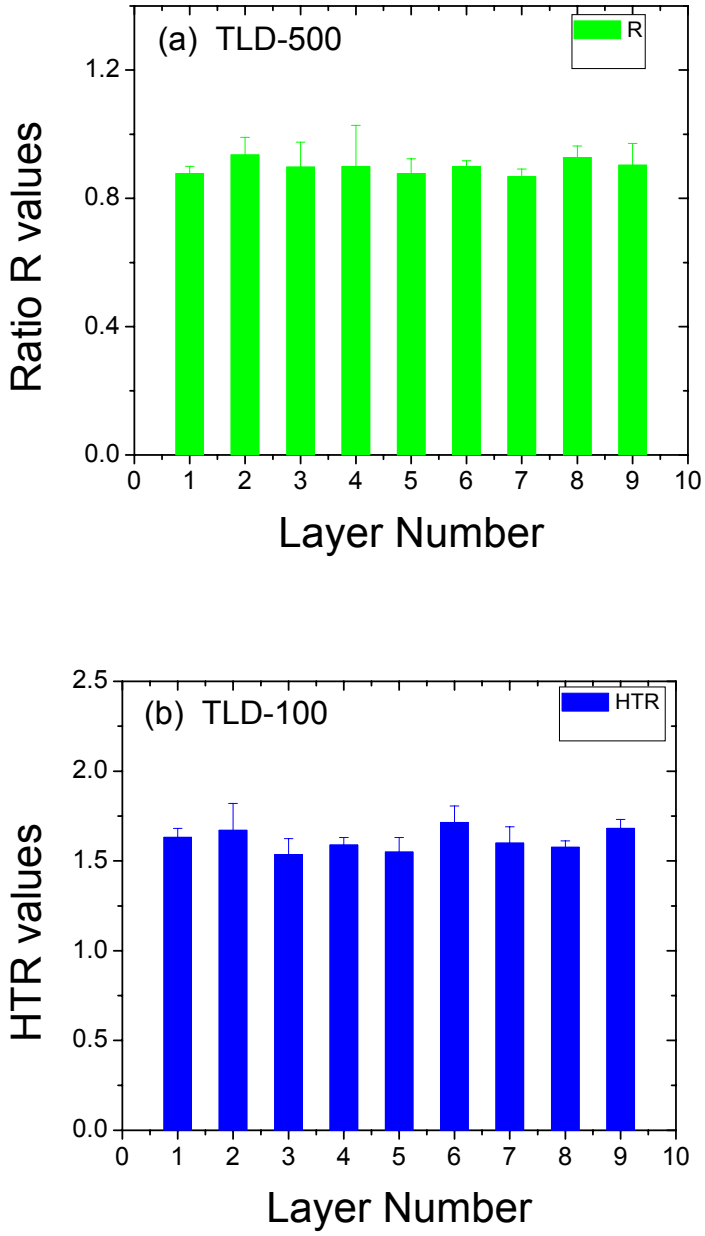

Figure 7.3. The R values for the TLD-500 chips (a) and the HTR values for the TLD-100 dosimeters (b) corresponding to each layer of the BRADOS detector holder

The corresponding 'mean LET' values for the Al_2O_3:C samples ranged from 0.5 to 1.3 keV/µm, while for the LiF:Mg,Ti samples the 'mean LET' values were between 2.3 and 2.6 keV/µm. There may be some small errors in estimating 'mean LET' values by

the two methods that include the insufficient data for the calibration curves for the $LET < 2.2\,\text{keV}/\mu\text{m}$ region for both TLD-500 and TLD-100. In addition, errors in the calculation of 'mean LET' values may appear considering that the calibration data (Figure 6.9) were obtained for Al_2O_3:C chips obtained from Nextep Technologies, while the samples exposed during BRADOS were Al_2O_3:C chips obtained from Harshaw (TLD-500). Nevertheless, considering the two types of Al_2O_3:C material are similar these errors should be small.

Table 7.4. The absorbed doses for the Al_2O_3:C (TLD-500) and LiF:Mg,Ti (TLD-100)

Layer #	TLD-500 Estimated Absorbed Dose (mGy)	TLD-100 Estimated Absorbed Dose (mGy)
#1	18.6 ± 1.0	22.7 ± 0.5
#2	16.6 ± 1.4	22.2 ± 0.6
#3	17.0 ± 2.8	22.3 ± 0.4
#4	15.9 ± 4.9	20.7 ± 0.5
#5	18.5 ± 1.7	21.0 ± 0.9
#6	16.1 ± 0.4	20.5 ± 0.9
#7	17.0 ± 1.0	19.9 ± 1.1
#8	14.9 ± 0.7	19.9 ± 0.1
#9	15.2 ± 1.9	19.8 ± 0.4

7.4. Antarctica Balloon Flight project

In addition to the space projects in Low-Earth Orbit, several luminescence

dosimeters were flown aboard the TRACER balloon around the South Pole at an altitude of about 125,000 ft during a 14 day mission (Dec 12 – Dec 27, 2003). The TRACER (i.e. Transition Radiation Array for Cosmic Energetic Radiation) instrument was used by a group of scientists from the University of Chicago to measure the heavy ions from cosmic rays, from oxygen up to iron and energies between $10^{13} - 10^{14}$ eV/nucleus[v]. The dosimeter packages were mounted onto the Tracer gondola and they consisted of: Al_2O_3:C chips, Luxel, LiF:Mg,Ti (TLD-100) and CaF_2:Tm (TLD-300) dosimeters. The samples were returned to the laboratory in July 2004 and they were analyzed using both OSL (i.e., Al_2O_3:C chips, Luxel) and TL (i.e., TLD-100 and TLD-300) methods.

Table 7.5. Gamma dose from the TRACER Antarctic Balloon radiation measurements

Material	**Gamma Dose (mGy) Integrated OSL**	**Gamma Dose (mGy) Initial OSL**
Al_2O_3:C/holder 1	1.33 ± 0.03	1.55 ± 0.05
Al_2O_3:C/holder 2	1.34 ± 0.05	1.67 ± 0.09
Luxel/holder 1	1.75 ± 0.00*	2.03 ± 0.00*
Luxel/holder 2	1.79 ± 0.00*	1.99 ± 0.00*
Material	**Gamma Dose (mGy) Area main peak**	**Gamma Dose (mGy) HT peak**
TLD-100/holder 1	1.66 ± 0.15	2.56 ± 0.34
TLD-100/holder 2	1.72 ± 0.11	2.67 ± 0.34
TLD-300/holder 1	1.59 ± 0.02	2.17 ± 0.02
TLD-300/holder 2	1.68 ± 0.04	2.26 ± 0.05

*Errors smaller than 0.005

[v] More information about TRACER can be found at http://tracer.uchicago.edu/science.html

The corresponding gamma doses to water for all of the investigated luminescence dosimeters from the Balloon Experiment are given in Table 7.5. The errors in the table represent the standard deviation of the mean for 6 samples (Luxel) and 4 samples/each for the other materials. The reported gamma doses were of the order of a few mGy. These values were corrected using several methods: the $R-$ method for the Al_2O_3:C chips and the Luxel samples, the HTR method for the TLD-100 samples and the peak $5+6$ / peak 3 method for the TLD-300 samples. The estimated absorbed doses are presented in Table 7.6.

Table 7.6. Estimated absorbed doses from the TRACER Antarctic Balloon measurements

Material	Corrected Gamma Dose (mGy) Al_2O_3:C	Corrected Gamma Dose (mGy) Luxel	Corrected Gamma Dose (mGy) TLD-100	Corrected Gamma Dose (mGy) TLD-300
holder 1	1.57 ± 0.10	1.76 ± 0.02	1.69 ± 0.15	1.59 ± 0.03
holder 2	1.78 ± 0.30	1.80 ± 0.04	1.75 ± 0.11	1.68 ± 0.05

7.5. Space irradiations projects: discussion of the results

It can be seen from Table 7.2, Table 7.4 and Table 7.6 that the estimated absorbed doses given by different dosimeters exposed to the same space radiation fields have different values. This result can be related to the different behavior of the OSL/TL efficiencies for different dosimeter materials as functions of the LET of the incident particles (shown in graphs 6.9a-6.12a), as explained in the next paragraphs.

Consider a mixed radiation field with a continuous LET spectrum within the limits of

L_1 to L_2 incident on a dosimeter. Moreover, suppose the dose delivered by each LET component is the same, i.e. $\frac{dD}{dL} = C$ for the entire LET range, where C is a constant with units of Gy/(keV/μm). Then the total dose absorbed in the dosimeter can be obtained via an integration (summation) procedure, as follows:

$$D = \int_{L_1}^{L_2} C \cdot dL \tag{7.1}$$

The signal measured from the dosimeter can be obtained from a similar summation, where the efficiency η appears in the integral as a function of the linear energy transfer, L:

$$S = \int_{L_1}^{L_2} C \cdot \eta(L) \cdot dL \tag{7.2}$$

The above relation indicates that the total signal measured from a dosimeter exposed to a mixed radiation field is obtained from a convolution of the actual dose distribution (which, for the sake of simplicity, was considered uniform for purposes of the argument above) and the shape of the efficiency as a function of LET, $\eta(L)$. An equivalent statement would be that the 'mean LET' measured from the OSL/TL signals, by methods such as $R-$method and HTR method, is not the average LET of the incident radiation, but rather the 'mean LET' of the radiation "seen" by the dosimeter, i.e. the average LET weighted by the dosimeter efficiency.

This concept is illustrated by a simple numerical example that considers two types of dosimeters, A and B, exposed to the same mixed radiation field of a given dose with an LET region of interest from 1 to 4 keV/μm, as illustrated in Figure 7.4.

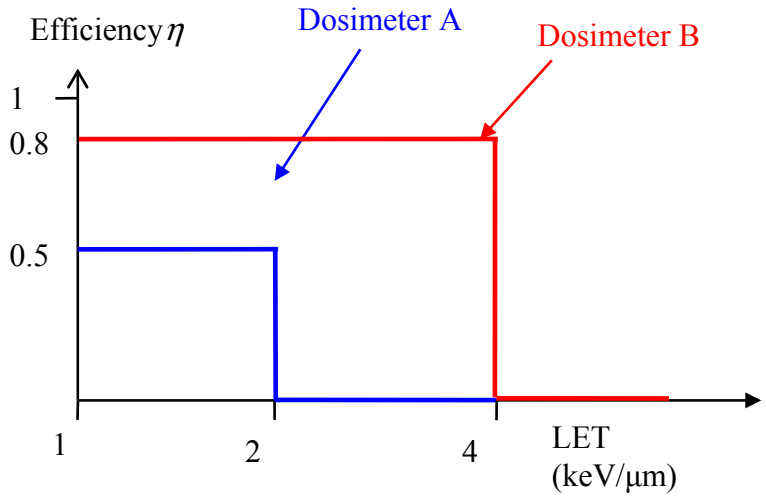

Figure 7.4. Illustration of the numerical example regarding for dosimeters A and B

The LET spectrum in Figure 7.4 is composed of four different particles, p_n each with a corresponding LET value L_n, with $n = 1..4$. The dosimeter A is considered to have an efficiency $\eta_A = 0.5$, for the $1 < L < 2\,\text{keV/μm}$ region and $\eta_A = 0$ for the $2 < L < 4\,\text{keV/μm}$ region. The dosimeter B has $\eta_B = 0.8$ for $1 < L < 4\,\text{keV/μm}$. Thus, for both A and B the average LET of the incident radiation spectrum is calculated as follows:

$$\overline{L}_{A,B} = \frac{\sum_n L_n}{n} = 2.5 \tag{7.3}$$

Nevertheless, the actual 'mean LET' seen by the dosimeters A and B is calculated considering the different efficiencies of the two materials, as follows:

$$\overline{L}'_{A,B} = \frac{\sum_n \eta_n L_n}{n} \tag{7.4}$$

Thus, by applying equation (7.4) to A and B:

$$\overline{L}'_A = \frac{0.5\times 1 + 0.5\times 2 + 0\times 3 + 0\times 4}{4} = 0.375 \qquad (7.5a)$$

$$\overline{L}'_B = \frac{0.8\times 1 + 0.8\times 2 + 0.8\times 3 + 0.8\times 4}{4} = 2 \qquad (7.5b)$$

By comparing equations (7.3), (7.5a) and (7.5b) it is clearly seen that the 'mean LET' values 'seen' by the dosimeters A and B are different and they also differ from the actual 'mean LET' value of the incident mixed radiation field.

7.6. Future space projects

The MATROSHKA Project started in 2003 in collaboration with the European Space Agency (ESA). The project is an international collaboration between several research groups from Austria, Germany, Hungary, Japan, Poland, Russia, UK and USA, under the patronage of ESA. The scientific objective of the MATROSHKA experiment is to study the radiation exposure of the astronauts during extravehicular activities (i.e., spacewalks) outside the International Space Station, by using a so-called 'phantom' made of materials very similar to human tissue in order to simulate the human body. The phantom consists of slices composed of natural bones, embedded in tissue equivalent plastic that accounts for the difference in the density of different biological end points (i.e., tissue and lung). A picture of the 'phantom' is shown in Figure 7.5. The phantom is made out of slices which can be equipped with hundreds of radiation dosimeters in order to measure the absorbed dose at different locations inside the body (i.e., lungs, torso, head, etc.). Also, the phantom is covered by a 'poncho' that simulates the astronauts/cosmonauts space suits.

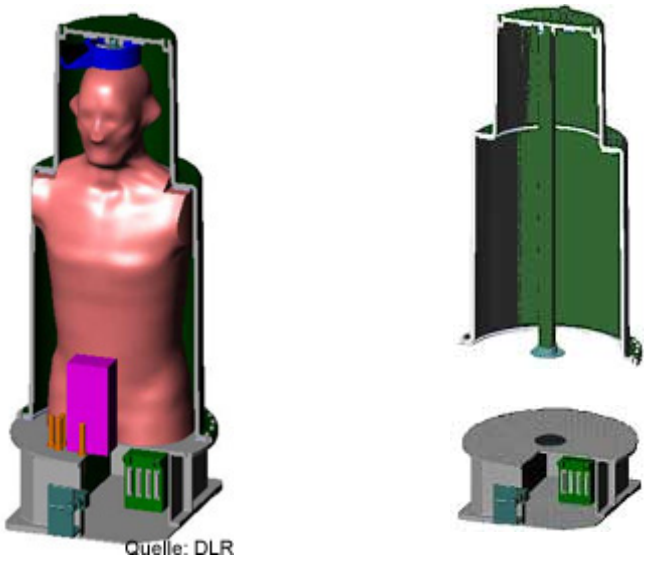

Figure 7.5. Picture of the human 'phantom' MATROSHKA[vi]

MATROSHKA was launched on January 29, 2004 onboard the Russian space vehicle Soyuz and was placed outside the ZVEZDA module of the Russian segment of the International Space Station during a spacewalk on February 26, 2004. The phantom will remain outside the station for almost a year, after which it will be retrieved by astronauts/cosmonauts and brought back to Earth. A picture of the launch is provided in Figure 7.6, courtesy of Thomas Berger of the German Aerospace Center (DLR).

Both active and passive dosimeters were used inside the MATROSHKA phantom by the several participating groups. Oklahoma State University (OSU) has of the order of a few hundred phantom passive dosimeters, including both OSLDs and TLDs (i.e., Luxel TLD-100 and TLD-300). The samples were placed on the phantom torso, phantom head and on the phantom poncho and will yield depth-dose data inside the stimulated human body, and, when used in conjunction with the CR-39 detectors will yield more

[vi] Picture obtained from
http://www.dlr.de/me/Institut/Abteilungen/Strahlenbiologie/arbeitsgruppen/Biophysik/matroshka_dos

information on the response of these detectors to high-LET fields. The luminescence dosimeters are expected to return to OSU in the spring of 2005 for analysis.

Figure 7.6. Picture of the launch of the Russian spacecraft Soyuz that carried MATROSHKA to the ISS

7.7. Conclusions regarding the space irradiations

Considering the present results, the main conclusion is that all of the correction methods presented in Chapter 6 (i.e., $R-$method, HTR method and peak$5+6$/peak3 method) can be used, in the first approximation, in order to obtain information about the absorbed dose values in space radiation fields. Nevertheless, none of these correction

methods can give information about the actual ‘mean LET’ of the space radiation field, but rather about the ‘mean LET’ values as ‘seen’ by different dosimeters (i.e., Al_2O_3:C, LiF:Mg,Ti and CaF_2:Tm).

Also, since the actual absorbed doses during the STS-105, ISS, BRADOS and TRACER projects are not known, it cannot be inferred from the above experiments which material/method gives the most accurate result in terms of absorbed doses. In addition, further research is needed in order to improve the calibration curves and to investigate further the luminescence response of Al_2O_3:C materials to space radiation fields. The MATROSHKA project as well as the collaborations with Johnson Space Center and the European Space Agency will continue in the future with the purpose of better understanding of the behavior of luminescence dosimeters in space radiation fields.

CHAPTER 8

SUMMARY AND CONCLUSIONS

This thesis presents the results of an investigation on the applicability of OSL from Al_2O_3:C as dosimetry method for the characterization of the radiation field in space. The space environment is a complex mix of charged particles, thus studies of the OSL response from Al_2O_3:C exposed to a large variety of HCP are imperative. In Chapter 5 the OSL response from Al_2O_3:C was investigated for irradiations with low-energy charged particles. Even though these HCPs are not expected to be part of the space radiation fields, by studying their influence on the luminescence response of our material (Al_2O_3:C), one can gain better knowledge about the HCP-induced luminescence efficiency and the effects of factors such as E (energy), Z (atomic number) and E/A (energy per nucleon) that may influence this luminescence efficiency. From preliminary experiments performed for irradiations with high-energy heavy charged particles with characteristics similar to those in space, presented in Chapter 6, we concluded that the relative OSL sensitivity (i.e., efficiency η) of Al_2O_3:C decreases with an increase in the particle LET. Thus, it is not possible to accurately determined the dose D absorbed in luminescence dosimeters from unknown particle fields (or dose equivalent H) if the variations in efficiency are not considered.

To correct for the variations in the efficiency, we suggested two empirical methods (i.e., the $R-$method and the $\tau-$method) that allow the determination of the 'mean LET' from the shape of the OSL decay, after a pre-calibration in known particle fields. This information, in conjunction with the subsequent 'mean efficiency', allows us to estimate

one of the parameters of interest, the absorbed dose D. In addition, 'mean LET' can give us information about 'mean Q' (since $Q = Q(L)$) which can be used to estimate the other parameter of interest, the dose equivalent H.

Various experiments were performed in order to ensure the validity of the procedure, as presented in Chapter 6. Multiple irradiations using a variety of radiation fields allowed a better characterization of the behavior of the OSL signal from the dosimeter over a large range of radiation quality. Absorbed dose (i.e., corrected dose) values obtained in subsequent tests involving mixed irradiations agreed well with the actual absorbed doses for mixed fields with strong low-LET components, while for mixed fields with strong high-LET components errors up to 10% were observed when estimating the absorbed dose (Table 6.2). However, significant additional errors may be introduced when estimating the dose equivalent (Table 6.3), considering the strong dependence of Q on L for high-LET particles (Figure 1.1).

Finally, the calibrated responses were used to extract information regarding the dose absorbed in the Al_2O_3:C dosimeters during exposures to actual space radiation fields, during the STS-105 flight of the space shuttle Discovery (July 2001), the ISS radiation exposures (July-Dec 2001), and the BRADOS experiment on the ISS (Oct-Dec 2003). In addition, high-altitude radiation exposure was measured during the TRACER Antarctic Balloon project (Dec 2003).

The results indicated the validity of using the OSL signal from Al_2O_3:C in order to determine correct, in the fist approximation, the measured signal by the efficiency in order to obtain the absorbed dose and, to some extent, the dose equivalent for exposures in Low-Earth Orbit. Nevertheless, these correction methods cannot give information

about the actual ‘mean LET’ of the space radiation field, but rather about the ‘mean LET’ values as ‘seen’ by the Al_2O_3:C dosimeters. Thus, the NCRP recommendation for mixed space radiation fields (i.e., use of OSL/TL dosimeters together with PNTDs) should be followed.

In addition, the dose estimations obtain for all of the presented materials/methods need to compared with the actual doses absorbed during the STS-105, ISS, BRADOS and TRACER experiments in order to gain a better insight about what material/method is most suitable for space applications.

REFERENCES

Aitken, M.J., 1998. An Introduction to Optical Dating. Oxford University Press, Oxford.

Akselrod, A.E., Akselrod, M.S., 2002. Correlation between OSL and the distribution of TL traps in Al_2O_3:C. Radiat. Prot. Dosim. 100, 217 – 220.

Akselrod, M.S., Agersnap Larsen, N., McKeever, S.W.S., 2000. A procedure for the distinction between static and dynamic radiation exposures of personal radiation badges using pulsed optically stimulated luminescence. Radiat. Prot. Dosim. 32, 215 – 225.

Akselrod, M.S., Agersnap Larsen, N., Whitley, V., McKeever, S.W.S., 1998. Thermal quenching of F -center luminescence in Al_2O_3:C. J. Appl. Phys. 84, 3364 – 3373.

Akselrod, M.S., Agersnap Larsen, N., Whitley, V., McKeever, S.W.S., 1998. Thermal quenching of F centre luminescence in Al_2O_3:C. Radiat. Prot. Dosim. 84, 39 – 42.

Akselrod, M.S., Kortov, V.S., Gorelova, E.A., 1993. Preparation and properties of $\alpha - Al_2O_3$:C. Radiat. Prot. Dosim. 47, 159 – 164.

Akselrod, M.S., Kortov, V.S., Kravetsky, D.J., Gotlib, V.I, 1990. Higly sensitive thermoluminescent anion-defect $\alpha - Al_2O_3$:C single crystal detectors. Radiat. Prot. Dosim. 33, 119 – 122.

Akselrod, M.S., Lucas, A.S., Polf, J.C., McKeever, S.W.S., 1998b. Optically stimulated luminescence of Al_2O_3:C. Radiat. Meas. 29, 391– 399.

Akselrod, M.S., McKeever, S.W.S., 1999. A radiation dosimetry method using pulsed optically stimulated luminescence. Radiat. Prot. Dosim. 81, 167 – 176.

Akselrod, M.S., McKeever, S.W.S., Moscovitch, M., Emfietzoglou, D., Durham, J.S., Soares, C.G., 1996. A thin-layer Al_2O_3:C beta TL detector. Radiat. Prot. Dosim. 66,

105 – 110.

Armstrong, T.W., Colburn, B.L., 2001. Predictions of secondary neutrons and their importance to radiation effects inside the international space station. Radiat. Meas. 33, 229 – 234.

Attix, F.H., 1986. Introduction to Radiological Physics and Radiation Dosimetry. Wiley, New York.

Avilés, P., Gamboa-deBuen, I., Rodríguez-Villafuerte, M., Buenfil, A.E., Ruiz-Trejo, C., López, K., Brandan, M.E., 1999. Thermoluminesnce response of TLD-100 to low energy protons. Radiat. Prot. Dosim. 84, 83 – 86.

Avilla, O., Gamboa-deBuen, I., Brandan, M.E., 1999. Study of the energy deposition in LiF by heavy charged particle irradiation and its relation to the thermoluminescence efficiency of the material. J. Phys. D: Appl. Phys. 32, 1175 – 1181.

Badhwar, G.D., 1997. The radiation environment in low-Earth orbit. Radiat. Res. 148 (Suppl.), S3-S10.

Badhwar, G.D., Keith, J.E., Cleghorn, T.E., 2001. Neutron measurements onboard the space shuttle. Radiat. Meas. 33, 235 – 241.

Badhwar, G.D., Watts, J., Cleghorn, T.E., 2001. Radiation dose from reentrant electrons. Radiat. Meas. 33, 369 – 372.

Bailiff, I.K., 1995. The use of ceramics for retrospective dosimetry in the Chernobyl exclusion zone. Radiat. Meas. 24, 507 – 511.

BCRM, 2003. An Approach to Risk Reduction and Management for Human Space Flight, Bioastronautics Critical Road Map, Baseline Document, http://criticalpath.jsc.nasa.gov/.

Benton, E.R., Frank, A.L., Benton, E.V., 2000. TLD efficiency of ^{7}LiF for doses deposited by high-LET particles. Radiat. Meas. 32, 211 – 214.

Benton, E.R., Benton, E.V., 2001. Space radiation dosimetry in low-Earth orbit and beyond. Nucl. Instr. Meth. Phys. Res. B. 184, 255 – 294.

Bøtter-Jensen, L., Agersnap Larsen, N., Markey, B.G., McKeever, S.W.S., 1997. Al_2O_3:C as a sensitive OSL dosemeter for rapid assessment of environmental photon dose rates. Radiat. Meas. 27, 295 – 298.

Bøtter-Jensen, L., Banerjee, D., Jungner H., Murray, A.S., 1999a. Retrospective assessment of environmental dose rates using optically stimulated luminescence from Al_2O_3:C and quartz. Radiat. Prot. Dosim. 84, 537 – 542.

Bøtter-Jensen, L., Bulur, E., Duller, G.A.T., Murray, A.S., 2000. Advances in luminescence instrument systems. Radiat. Meas. 32, 523 – 528.

Bøtter-Jensen, L., Duller, G.A.T., Murray, A.S., Banerjee, D., 1999b. Blue light emitting diodes for optical stimulation of quartz in retrospective dosimetry and dating. Radiat. Prot. Dosim. 84, 335 – 340.

Bøtter-Jensen, L., McKeever, S. W. S., Wintle, A. G., 2003. Optically stimulated luminescence dosimetry. Elsevier, New York.

Bräunlich, P. (Ed.), 1979. Thermally Stimulated Relaxation in Solids. In: Topics in Advanced Physics, 31. Springer, Berlin.

Bulur, E., 1996. An alternative technique for optically stimulated luminescence (OSL) experiment. Radiat. Meas. 26, 701 – 709.

Butts, J.J., Katz, R., 1967. Theory of RBE for heavy ion bombardment of dry nezimes and viruses. Radiat. Res. 30, 855 – 871.

Chen, R., McKeever, S.W.S., 1997. Theory of Thermoluminescence and Related Phenomena. World Scientific Publishing, Singapore.

Eisberg, R., Resnick, R, 1985. Quantum Physics of Atoms, Molecules, Solids, Nuclei, and Particles. Wiley & Sons, New York.

Gamboa-deBuen, I., Avilés, P., Rodríguez-Villafuerte, M., Buenfil, A.E., Ruiz-Trejo, C., Brandan, M.E., 2001. Supralinear response and efficiency of LiF:Mg,Ti to 0.7, 1.5 and 3 MeV protons. Nucl. Instr. Meth. Phys. Res. B. 183, 487 – 496.

Gamboa-deBuen, I., Ruiz, C., Oliver, A., López, K., Brandan, M.E., 1998. Measurement of the thermoluminescent response (supralinearity and efficiency) of LiF:Mg,Ti to 0.7 MeV protons. Nucl. Instr. Meth. Phys. Res. B. 134, 136 – 148.

Gaza, R., Yukihara, E.G., McKeever, S.W.S., (2003). The 4th ICCHIBAN report on the optically stimulated luminescence of Al_2O_3:C to high-energy heavy charged particles. HIMAC Internal Document, NIRS, Japan.

Gaza, R., Yukihara, E.G., McKeever, S.W.S., (2004). The response of thermally and optically stimulated luminescence from Al_2O_3:C to high-energy heavy charged particles. Radiat. Meas. 38, 417 – 420.

Gaza, R., Yukihara, E.G., McKeever, S.W.S., (2004). The use of optically stimulated luminescence from Al_2O_3:C in the dosimetry of high-energy heavy charged particle fields. Radiat. Meas. (submitted in July 2004).

Gaza, R., Yukihara, E.G., McKeever, S.W.S., Avila, O., Buenfil, A.E., Gamboa-deBuen, I., Rodríguez-Villafuerte, M., Ruiz-Trejo, C., Brandan, M.E., (2004). Ionization density dependence of the optically stimulated luminescence dose response of Al_2O_3:C low-energy charged particles. Radiat. Meas. (submitted in July 2004).

Gaza, R., 2004. A fiber-optics, real-time dosimeter based on optically stimulated luminescence of Al_2O_3:C and KBr:Eu, for potential use in the radiotherapy of cancer. PhD Thesis. Oklahoma State University, Stillwater.

Geiβ, O. B., Krämer, M., Kraft, G. (1998). Efficiency of thermoluminescent detectors to heavy charged particles. Nucl. Instr. Meth. Phys. Res. B 142, 592 – 598.

Hajek, M., Berger, T., Schöner, W., Summerer, L., and Vana, N., 2002. Dose assessment of aircrew using passive detectors. Radiat. Prot. Dosim. 100, 511 – 514.

Hess, W.N., 1968. The Radiation Belt and Magnetosphere. Blaisdell Publishing Co., Waltham.

Horowitz, Y.S., 2001. Theory of thermoluminescence gamma dose response: The unified interaction model. Nucl. Instr. Meth. Phys. Res. B. 184, 68 – 84.

Horowitz, Y.S., Avila, O., Rodríguez-Villafuerte, M., 2001. Theory of heavy charged particle response (efficiency supralinearity) in TL materials. Nucl. Instr. Meth. Phys. Res. B. 184, 85 – 112.

Horowitz, Y.S., Mahajna, S., Rosenkrantz, M., Yossian, D., 1996. Unified theory of gamma and heavy charged particle TL supralinearity: The track/defect interaction model. Radiat. Prot. Dosim. 65, 7 – 12.

Horowitz, Y.S., Rosenkrantz, M., Mahajna, S., Yossian, D., 1996. The track interaction model for alpha particle induced thermoluminescence supralinearity: Dependence of the supralinearity on the vector properties of the alpha particle radiation field. J. Phys. D. 29, 205 – 217.

Horowitz, Y.S., Satinger, D., Oster, L., Issa, N., Brandan, M.E., Avila, O., Rodríguez-Villafuerte, M., Gamboa-deBuen, I., Buenfil, A.E., Ruiz-Trejo, C., 2001. The

extended track interaction model: Supralinearity and saturation He-ion TL fluence response in sensitized TLD-100. Radiat. Meas. 33, 459 – 473.

Huntley, D.J., Godfrey-Smith, D.I., Thewalt, M.L.W., 1985. Optical dating of sediments. Nature 313, 105-107.

ICRP, 1991. 1990 Recommendations of the International Radiological Commission on Radiological Protection, International Commission on Radiological Protection, Publication 60.

Kalef-Ezra, J., Horowitz, Y.S., 1982. Heavy charged particle thermoluminescence dosimetry: Track structure theory and experiments. Int. J. Appl. Radiat. Isot. 33, 1085-1100.

Kittel, C., 1996. Introduction to Solid State Physics. John Wiley & Sons, Inc., New York.

Klein, D.M., Yukihara, E.G., Bulur, E., Durham, J.S., Akselrod, M.S., McKeever, S.W.S., 2004. An optical fiber radiation sensor for remote detection of radiological materials. IEEE Sensors (submitted).

McKeever, S.W.S., 1985. Thermoluminescence of Solids. Cambridge University Press, Cambridge.

McKeever, S.W.S., 2001. Optically stimulated luminescence dosimetry. Nucl. Instr. Meth. Phys. Res. B. 184, 29 – 54.

McKeever, S.W.S., Agersnap Larsen, N., Bøtter-Jensen, L., Mejdahl, V., 1997b. OSL sensitivity changes during single aliquot procedures: Computer simulations. Radiat. Meas. 27, 75 – 82.

McKeever, S.W.S., Akselrod, M.S., Markey, B.G., 1996. Pulsed optically stimulated luminescence dosimetry using $\alpha - Al_2O_3$:C . Radiat. Prot. Dosim. 65, 267 – 272.

McKeever, S.W.S., Akselrod, M.S., Colyott, L.E., Agersnap Larsen, N., Polf, J.C., Whitley, V., 1999. Characterization of Al_2O_3 for use in thermally and optically stimulated luminescence dosimetry. Radiat. Prot. Dosim. 84, 163 – 168.

McKeever, S.W.S., Bøtter-Jensen, L., Agersnap Larsen, N., Duller G.A.T., 1997a. Temperature dependence of OSL decay curves: Experimental and theoretical aspects. Radiat. Meas. 27, 161 – 170.

McKeever, S.W.S., Chen, R., 1997. Luminescence models. Radiat. Meas. 27, 625 – 661.

McKeever, S.W.S., Moscovitch, M., Townsend, P.D., 1995. Thermoluminescence dosimetry materials: Properties and uses. Nuclear Technology Publishing, Ashford.

Mewaldt, R.A., 1996. Cosmic Rays. Macmillan Encyclopedia of Physics. http://www.srl.caltech.edu/personnel/dick/cos_encyc.html.

Mische, E.F., McKeever, S.W.S., 1989. Mechanisms of supralinearity in lithium fluoride luminescence dosimeters. Radiat. Prot. Dosim. 29, 159 – 175.

Moscovitch, M., Tawil, R.A., Svinkin, M., 1993. Light induced fading in $\alpha - Al_2O_3$:C. Radiat. Prot. Dosim. 47, 251 – 253.

NCRP, 1989. Guidance on Radiation Received in Space Activities, National Council on Radiation Protection and Measurements, Report 98.

NCRP, 2000. Radiation Protection Guidance for Activities in Low-Earth Orbit, National Council on Radiation Protection and Measurements, Report 132.

NCRP, 2002. Operational Radiation Safety Program for Astronauts in Low-Earth Orbit: A Basic Framework, National Council on Radiation Protection and Measurements Report 142.

Polf, J.C., 2002. A study of optically stimulated luminescence in Al_2O_3 fibers for the

development of a real-time, fiber optic dosimetry system. PhD Thesis, Oklahoma State University, Stillwater.

Randall, J.T., Wilkins, M.H.F., 1945. Phosphorescence and electron traps I. The study of trap distributions. Proc. Roy. Soc. London 184, 366 – 389.

Reames, D.V., 1995. Solar energetic particles: A paradigm shift. Rev. Geophys. 33, 585 – 589.

Rodríguez-Villafuerte, M., Buenfil, A.E., Gamboa-deBuen, I., Ruiz-Trejo, C., Brandan, M.E., Yossian, D., Satinger, D., Horowitz, Y.S., 2000. Study of the TL response of LiF:Mg,Ti to 3 and 7.5 MeV helium ions: Measurement and interpretation in terms of the track interaction model. Nucl. Instr. Meth. Phys. Res. B. 160, 377 – 386.

Schöner, W., Vana, N., Fugger, M., 1999. The LET dependence of LiF:Mg,Ti dosimeters and its applications for Let measurements in mixed radiation fields. Radiat. Prot. Dosim. 85, 263 – 266.

Shea, M.A., Smart, D.F., 1990. A summary of major solar proton events. Solar Phys. 127, 297 – 320.

Simpson, J.A., 1983a. Elemental and isotopic composition of the galactic cosmic rays. Ann. Rev. Nucl. Part. Sci. 33, 323 – 381.

Smart, D.F., Shea, M.A., 1997. Solar radiation. Encycl. Appl. Phys. 18**,** 394 – 429.

Vana, N., Schöner, W., Fugger, M., Akatov, Y., 1996. Absorbed dose measurement and LET determination with TLDs in space. Radiat. Prot. Dosim. 66, 145 – 152.

Vana, N., Schöner, W., Fugger, M., Akatov, Y., Shurshakov, V., 1996. ADLET-Absorbed dose and average LET determination with TLDs on the space station MIR during a Russian long-term flight. in space. Radiat. Prot. Dosim. 66, 173 – 177.

Walker, F.D., Colyott, L.E., Agersnap Larsen, N., McKeever, S.W.S., 1996. The wavelength dependence of light-induced fading of thermoluminescence from $\alpha - Al_2O_3$. Radiat. Meas. 26, 711 – 718.

Walters, H., 1962. Hermann Oberth: Father of Space Travel. Macmillan, New York.

Wintle, A.G. Murray, A.S., 2000. Quartz OSL: Effects of thermal treatment and their relevance to laboratory dating procedures. Radiat. Meas. 32, 387 – 400.

Yasuda, H., Fujitaka, K., 2000. Non-linearity of the high temperature peak area ratio of ^{6}LiF:Mg,Ti (TLD-600). Radiat. Meas. 32, 355 – 360.

Yasuda, H., Kobayashi, I, 2002. Optically stimulated luminescence from Al_2O_3:C irradiated with relativistic heavy ions. Radiat. Prot. Dosim. 66, 339 – 343.

Yasuda, H., Kobayashi, I, Morishima, H., 2002. Decaying patterns of optically stimulated luminescence from Al_2O_3:C for different quality radiations. J. Nucl. Sci. Technol. 39, 211 – 213.

Yukihara, E.G., Gaza, R., McKeever, S.W.S., Soares, C.G., 2004. Optically stimulated luminescence and thermoluminescence efficiencies for high-energy heavy charged particle irradiation in Al_2O_3:C. Radiat. Meas. 38, 59 – 70.

Yukihara, E.G., Whitley, V.H., McKeever, S.W.S., Akselrod, A.E., Akselrod, M.S., 2004. Effects of high-dose irradiation on the optically stimulated luminescence of Al_2O_3:C. Radiat. Meas. 37, 317 – 330.

Yukihara, E.G., Whitley, V.H., Polf, J.C., Klein, D.M., McKeever, S.W.S., Akselrod, A.E., Akselrod, M.S., 2003. The effects of deep trap population on the thermoluminescence of Al_2O_3:C. Radiat. Meas. 37, 627 – 638.

Appendix A. Distribution of the Al_2O_3:C and LiF:Mg,Ti samples inside the holder

For the helium irradiations (2.5, 5.0 and 8.9 MeV), each holder contained eighteen Al_2O_3:C samples and nine LiF:Mg,Ti samples, as shown in Figure A1. The Al_2O_3:C samples positioned in columns 1, 4 and 7 were read in TL mode, while the Al_2O_3:C dosimeters from columns 2, 5 and 8 were read in OSL mode. The LiF:Mg,Ti samples (positioned in columns 3, 6 and 9) were read in TL mode.

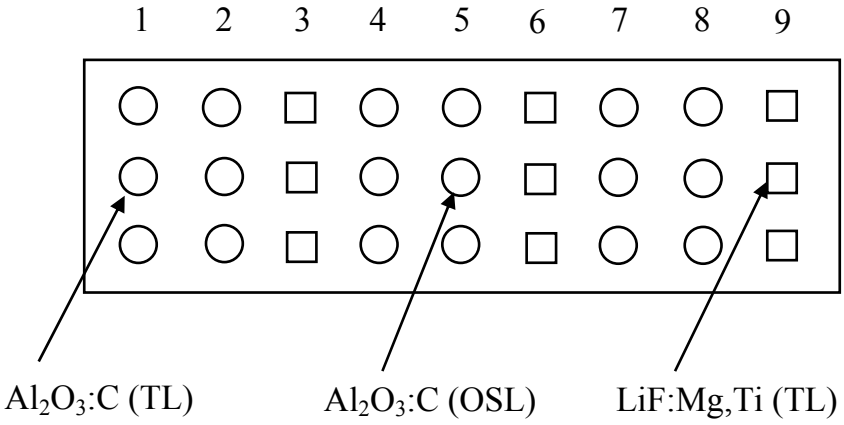

Figure A1. The distribution of Al_2O_3:C and LiF:Mg,Ti samples inside the holder for the 2.5, 5.0 and 8.9 MeV helium irradiations.

For the proton, carbon and oxygen irradiations the each chip holder contained eighteen polished Al_2O_3:C chips. For some of the irradiations (1.0 and 2.0 MeV protons) the sample holder contained also nine unpolished Al_2O_3:C chips and 8 LiF chips placed on the middle row, as shown in Figure A2. Also, Luxel sheets were placed in the sample holder with one sheet/holder for the proton (1 MeV), carbon and oxygen irradiations. All of the Al_2O_3:C samples were read in OSL mode, while the LiF samples were read in TL mode.

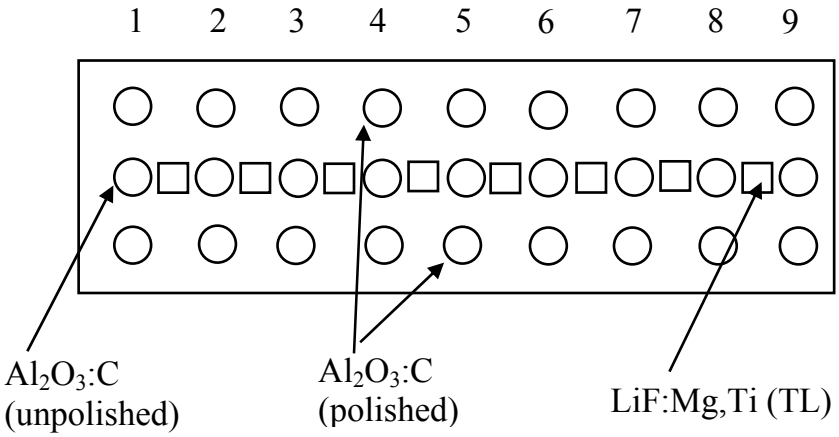

Figure A2. Distribution of the Al_2O_3:C and LiF:Mg,Ti samples inside the holder for the 1.0 MeV protons exposure.

Appendix B. Calculation of the kinematics factor k

In this appendix the expression $k = \dfrac{\left\{m\cos\theta \pm \left(M^2 - m\sin^2\theta\right)^{1/2}\right\}^2}{\left(m+M\right)^2}$ is to be demonstrated.

An incident particle of initial energy E and momentum $\vec{p}$ is elastically scattered by the target, as shown bellow. After collision, the particle is scattered at angle θ and has energy E_1 and momentum $\vec{p}_1$, while the target changes direction by angle φ with energy E_2 and momentum $\vec{p}_2$.

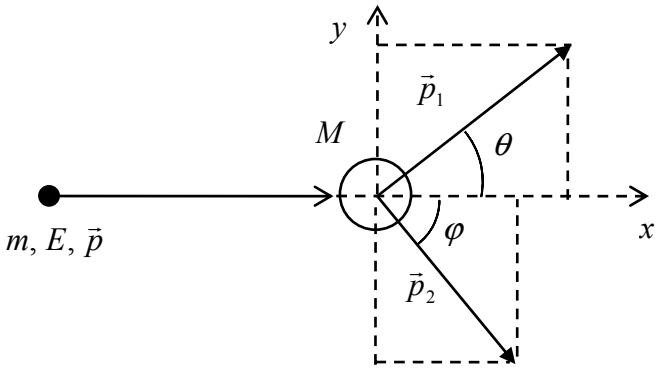

Thus, the energy and momentum conservation for the particle-target system yields:

$$\vec{p} = \vec{p}_1 + \vec{p}_2 \tag{1a}$$

$$E = E_1 + E_2 \tag{1b}$$

Using equation (1b) and projecting equation (1a) on $x-$ and $y-$axes, the following equations are obtained:

$$\frac{mv^2}{2} = \frac{mv_1^{\,2}}{2} + \frac{Mv_2^{\,2}}{2} \tag{2a}$$

$$mv = mv_1\cos\theta + Mv_2\cos\varphi \tag{2b}$$

$$m^2 v_1^{\,2}\sin^2\theta = Mv_2^{\,2}\sin^2\varphi \tag{2c}$$

Solving equations (2) for v_1:

$$v_1 = \frac{-v\left\{m\cos\theta \pm \left(M^2 - m\sin^2\theta\right)^{1/2}\right\}}{m+M} \tag{3}$$

Thus, the kinematics factor k is obtained as follows:

$$k = \frac{E_1}{E} = \frac{{v_1}^2}{v^2} = \frac{\left\{m\cos\theta \pm \left(M^2 - m\sin^2\theta\right)^{1/2}\right\}^2}{\left(m+M\right)^2} \tag{4}$$

(Q.E.D.)

VITA

Ramona Gaza

Candidate for the Degree of

Doctorate of Philosophy

Thesis: SPACE RADIATION DOSIMETRY: AN OPTICALLY STIMULATED LUMINESCENCE RADIATION DETECTOR FOR LOW-EARTH ORBIT

Major Field: Physics

Biographical:

Personal Data: Born in Lugoj, Romania, Europe, on October 29, 1972, the daughter of Mircea and Ioana Carabas.

Education: Graduated from the 'Coriolan Brediceanu' High School, Lugoj, Romania in 1991; received a Bachelor of Science degree in Physics from the Western University of Timisoara, Romania, in 1997. Completed the requirements for a Doctorate of Philosophy degree with a major in Physics at Oklahoma State University in December 2004.

Experience: Employed as an accountant consultant by Poliphem Smile, Ltd., between 1997 and 1999; employed by the Department of Physics at Oklahoma State University as a Research Assistant between 2000 and 2002 and 2003-2004, and as a Teaching Assistant, in 2002.

Professional Membership: American Physical Society (APS) since 2000; Arkansas-Oklahoma Center for Space and Planetary Sciences (CSAPS) since 2000; Member-elect of the National Honor Society of Phi Kappa Phi since 2002.

Name: Ramona Gaza Date of Degree: December, 2004

Institution: Oklahoma State University Location: Stillwater, Oklahoma

Title of study: SPACE RADIATION DOSIMETRY: AN OPTICALLY STIMULATED LUMINESCENCE RADIATION DETECTOR FOR LOW-EARTH ORBIT

Pages in Study: 160 Candidates for the Degree of Doctor of Philosophy

Major Field: Physics

Scope and Method of Study: The purpose of this study was to investigate Al_2O_3:C as a potential optically stimulated luminescence (OSL) radiation detector for Low-Earth Orbit. The OSL response of Al_2O_3:C was characterized in terms of its luminescence efficiency for a variety of heavy charged particles (HCPs) with features similar to those found in space. The HCP irradiations were performed using the HIMAC accelerator at Chiba (Japan), the proton facility at Loma Linda (CA) and the NSRL facility at Brookhaven (NY). The OSL curves were further investigated to obtain information about the 'mean efficiency' and 'mean LET', parameters that needed to assess the absorbed dose and the dose equivalent. This analysis was applied for simulated mixed radiation fields (ICCHIBAN) and actual space radiation exposures (i.e., STS-105, BRADOS, and TRACER). In parallel, the thermoluminescence response of dosimetry materials LiF:Mg,Ti and CaF_2:Tm was also studied.

Findings and Conclusions: The OSL efficiency of Al_2O_3:C exposed to HCPs was found to decrease with increasing linear energy transfer (LET) for the investigated LET range (i.e., from $0.4\,\text{keV}/\mu\text{m}$ to $459\,\text{keV}/\mu\text{m}$). For simulated mixed radiation fields with a strong low-LET component, the results indicated that the OSL calibration methods (i.e., $\tau-$ method and $R-$ method) can be used with good accuracy to obtain information about the absorbed dose and the dose equivalent. Nevertheless, for mixed fields with a strong high-LET component these methods will give larger errors when estimating the absorbed dose and the dose equivalent. For actual space radiation exposures, the results indicated that different materials/calibration methods (i.e., the LiF:Mg,Ti/HTR– method and the CaF_2:Tm/ $\text{peak}\,5+6/\text{peak}\,3-$ method) give different results in terms of 'mean efficiency' and 'mean LET'. This was explained by suggesting that none of the above calibration methods can give information about the true average LET of the incident radiation, but rather about the 'mean LET' weighted by the dosimeter efficiency.

Advisor's Approval: _____